4UU17 190

REPORT D‿CUMENTATION PAGE

AFOSR-TR-97

0569

1. AGENCY USE ONLY (Leave blank)

2. REPORT DATE 7/14/94

3. REPORT TYPE AND [illegible]
AFOSR Project Report - Dec. 1993

4. TITLE AND SUBTITLE
Site Specific Reactions of B and Si Based Compounds in Carbon

5. FUNDING NUMBERS
Contract Number
AFOSR-91-0103

AFOSR's Purchase Request
No.: FQ8671-9300189

6. AUTHOR(S)
Dawn A. Bonnell and John M. Vohs

7. PERFORMING ORGANIZATION NAME(S) AND ADDRESS(ES)
University of Pennsylvania
Dept. of Materials Science & Engineering
3231 Walnut Street
Philadelphia, PA 19104-6272

8. PERFORMING ORGANIZATION REPORT NUMBER
FINAL TECHNICAL REPORT

9. SPONSORING/MONITORING AGENCY NAME(S) AND ADDRESS(ES)
AFOSR / NC
Building 410
Bolling AFB
Washington DC 20332-6448

NA

10. SPONSORING/MONITORING AGENCY REPORT NUMBER

11. SUPPLEMENTARY NOTES

12a. DISTRIBUTION / AVAILABILITY STATEMENT
Unrestricted, no proprietary data

12b. DISTRIBUTION CODE

13. ABSTRACT *(Maximum 200 words)*

This report summarizes the progress made during three years of an AFOSR sponsored program directed towards understanding the atomic details of oxidation resistance in carbon based composites. The primary tools are scanning tunneling microscopy and spectroscopy, high resolution energy loss spectroscopy, and conventional surface analysis. The results of this program to date can be separated into three subfields; oxidative reactions on carbon: a model study; instrument design for in situ deposition studies; initial stages of SiOx deposition.

19971103 073

14. SUBJECT TERMS

15. NUMBER OF PAGES

16. PRICE CODE

17. SECURITY CLASSIFICATION OF REPORT

18. SECURITY CLASSIFICATION OF THIS PAGE

19. SECURITY CLASSIFICATION OF ABSTRACT

20. LIMITATION OF ABSTRACT

NSN 7540-01-280-5500

Standard Form 298 (Rev 2-89)
Prescribed by ANSI Std Z39-18
298-102

Final Report to the Air Force Office of Scientific Research on

THE RELATIONSHIP BETWEEN LOCAL DEFECT STRUCTURE AND REACTIVITY IN CARBON/CARBON AND BC_3

by

Dawn A. Bonnell* and John M. Vohs†

Department of Materials Science and
†Department of Chemical Engineering
The University of Pennsylvania
Philadelphia, PA 19104

TABLE OF CONTENTS

PREVIOUS WORK ON THIS PROJECT

SUMMARY OF PROPOSAL OBJECTIVES

During the three years of this project many objectives have been met. Specifically, the following has been accomplished:

> A portable CVD chamber that can be attached to several analysis systems, allowing *in situ* studies of the reactions of carbon with a number of compounds, has been designed and constructed .
>
> A new scanning tunneling microscope (STM) head designed for exceptional stability in order to perform site specific tunneling spectroscopy has been designed and built.
>
> A tip approach system based in part on the new STM design has been installed on an SEM-STM.
>
> Oxidative reactions on cleaved graphite, oxygen ion sputtered graphite, and oxygen plasma etched graphite, have been characterized by high resolution electron energy loss spectroscopy (HREELS) and STM.
>
> The morphological development of SiO_x films at the first stages of growth under various processing conditions has been characterized with HREELS, STM, and Rutherford Backscattering (RBS). Films from high pressure/high temperature and low pressure/low temperature deposition conditions have been compared. Determination of bond sequence at the carbon-SiO_x interface has been accomplished.

TECHNICAL REPORT

The results of this program to date can be separated into three subfields;

- oxidation reactions on carbon: a model study,
- instrument design for *in situ* deposition studies,
- initial stages of SiO_x deposition,

Selected results are described here in detail, after which the program productivity is summarized. More in depth descriptions and literature reviews can be found in the attached publications.

Oxidation Reactions on Graphite: a model study

Graphite was chosen as a model system for studies aimed at isolating the behavior of individual types of defects in carbon. This represents the first step in the study of defects. After individual defects are isolated and characterized, these studies will be extended to carbon fibers and eventually to carbon/carbon composites. HREELS has been used to identify surface functionalities that result after exposure to different oxidative atmospheres, including high energy oxygen ions and oxygen plasmas. Topographic STM imaging was used to characterize nominally and fully defected surfaces. The oxidative treatment conditions which have been studied to date are summarized in the Table below. Note that for treatment conditions employing molecular oxidants (i.e. O_2, CO, and H_2O) no reaction products could be identified with HREELS or Auger spectroscopy. Surface oxidation only occurred after exposure of the surface to high energy oxygen ions or radicals.

Table I. Reactivity of Graphite after Various Surface Treatments

Dose*	Temp (K)	Method	Reaction
	Cleaved graphite		
O_2, 35 L	At 1000	HREELS	None
O_2, 35 L	At 1050	HREELS	None
O_2, 35 L	At 1250	HREELS	None
O_2, 175 L	At 900	HREELS	None
O_2, 1260 L	At RT	TPD	None
O_2, 120000 L	At 1000	HREELS	None
H_2O, 56 L	At RT	HREELS	None
	Graphite sputtered with argon		
	At RT	HREELS	Roughened
O_2, 7 L	At RT	TPD	None
O_2, 35 L	At RT	TPD	None
O_2, 70 L	At RT	TPD	None
O_2, 140 L	At RT	HREELS, TPD	None, none
O_2, 600000 L	At RT	HREELS	None
CO, 5 L	At 100	TPD	None
CO, 17 L	At 650	TPD	None
CO, 9 L	At RT	TPD	None
CO, 70 L	At RT	TPD	None
CO, 140 L	At RT	TPD	None
CO, 210 L	At RT	HREELS	O-H
CO, 175000 L	At RT	HREELS	None
	Graphite sputtered with oxygen		
	At RT	HREELS	C=O, O-H, C-H
None	Heat to 1000	HREELS	C=O, O-H
None	Heat to 1250	HREELS	None
O_2, 350000 L	At RT	HREELS	O-H, C-H
	Graphite in oxygen plasma		
O_2, 175000 L	At RT	HREELS	C=O, O-H, C-H
None	Heat to 1140	HREELS	C=O

*L is langmuirs (1 L = 10^{-6} torr·s)

HREELS spectra of oxygen ion sputtered surfaces are shown Fig. 1. The spectrum of clean cleaved graphite is compared to those of the oxygen exposed surfaces. For the cleaved graphite surface the elastic peak intensity was found to be sharply peaked in the specular direction, indicating a relatively flat surface. Although no losses indicative of adsorbed species are present in the spectrum, the elastic peak does exhibit a broad tail that extends to high loss energies. This tail has been observed in a previous HREELS study of graphite surfaces and has been attributed to excitation of electron-hole pairs [1,2]. For a semimetal, such as graphite, the density of states at the Fermi energy (E_f) is zero, but rises both above and below E_f. Excitation of vertical transitions from the valence band to the conduction band can give rise to the energy loss continuum observed in the HREEL spectrum. This observation will be returned to in the discussion of BC_3.

As expected, the cleaved graphite surface was found to be relatively unreactive toward O_2. In contrast, the HREEL spectrum of the oxygen ion sputtered surface was found to be substantially different than that obtained from the cleaved surface. As shown in the figure, the most noticeable change which occurred upon sputtering was the appearance of several prominent losses centered at 460, 810, 1470, 2950, 3650 cm^{-1}. The two highest energy peaks can be assigned to the C-H stretching mode of surface hydrocarbon species (2950 cm^{-1}) and the O-H stretching mode of adsorbed hydroxyl groups (3650 cm^{-1}). Since significant amounts of H_2O are present in the chamber background gas during sputtering, it is likely that these surface CH_x and OH species were formed by dissociative adsorption of water at surface defect sites. It is somewhat more difficult to assign the peaks at lower loss energies. It is possible the peak centered at 1470 cm^{-1} is due to the C-H bending mode of the surface CH_x species. The origin of the large peak at 810 cm^{-1} will be discussed below. In addition to partially oxidizing the surface, the sputtering process also significantly increased the roughness of the surface. This was evident by a large decrease in the intensity of the elastic peak following sputtering and has been quantified by topographic analysis.

During heating to 1000 K, the primary desorption products were CO and CO_2. Carbon dioxide desorbed over a wide temperature range with a maximum occurring at 780 K. Carbon monoxide also desorbed over a wide temperature range with maxima occurring at 790 and 910 K. In addition, smaller amounts of H_2O and hydrocarbon species desorbed from the surface at temperatures between 300 and 500 K. The HREEL spectrum after heating was significantly different; the most noticeable changes being the almost complete disappearance of the C-H stretch at 3690 cm^{-1}, indicating the desorption of nearly all the CH_x species from the surface. Other changes include the appearance of small peaks centered at 1200, 1390, and 1600 cm^{-1} and a shift in the position of the large peak previously at 810 cm^{-1} to 530 cm^{-1}. The O-H stretching mode near 3600 cm^{-1} was relatively unchanged upon heating, indicating the continued presence of OH groups on the surface. The peak at 1200 cm^{-1} is also likely due to surface OH groups and can be attributed to the C-OH stretching mode of these species. The peak at 1600 cm^{-1} is in a position characteristic of a C=O stretching mode. It is somewhat more difficult to unambiguously assign the peak at 1390 cm^{-1}, however, the most reasonable assignment seems to be the O-H bending mode of the surface hydroxyl groups. These HREELS results indicate that the primary oxygen containing functional groups on the surface after heating to 1000 K are hydroxyls and carbonyls. The presence of carbonyl functionalities is consistent with the formation of surface semi-quinine species as has been previously proposed by Marchon et al. for graphitic particles[4,5]. Surface lactone species have also been proposed to exist on oxidized graphite and would give rise to a C=O stretching mode in the HREEL spectrum. The C=O stretching mode in lactones generally occurs, however, between 1700 and 1800 cm^{-1}. The lack of a peak in this region of the spectrum indicates that surface lactones were not formed by the oxidation procedure used in this study. After heating to approximately 1250 K none of the previous peaks related to oxygen containing species are observed, indicating the decomposition of the surface semi-quinone and C-OH species. These and the previous HREELS results provide direct spectroscopic evidence in support of the surface functional groups proposed by Marchon et al.[3,4]

The only feature in the HREEL spectra that has yet to be explained is the rather large peak that appeared at low energy in the spectra of the sputtered surface. After sputtering, this peak appeared at 810 cm^{-1} and shifted to 530 cm^{-1} upon heating the sample to 1000 K. This peak was found to persist even after extended annealing at 1250 K, suggesting that it is not due to an oxygen containing species on the surface. One possibility is that peak is due to a skeletal vibration of a surface polyaromatic species. Such species could easily be formed during the sputtering process. This result will later be compared to that obtained from BC_3.

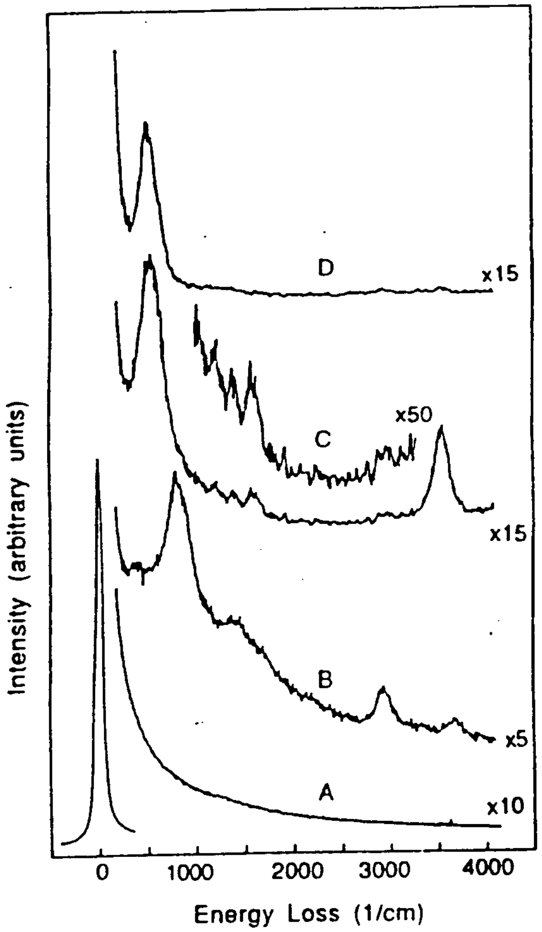

Fig. 1. (A) HREELS spectra of cleaved graphite after heating to 1000 K. (B) after sputtering with oxygen. (C) after heating sputtered sample to 1000 K. (D) after heating sputtered sample to 1250 K

The impact of sputtering on the surface morphology is indicated by the increased breadth and decreased intensity of the elastic HREELS peak. This increase can be associated with increased surface roughness, and has been quantified using both high resolution and large scan STM imaging. The topographic structures of cleaved and sputtered HOPG graphite are compared in the Fig. 2. Cleaved graphite typically contains surface steps with heights of integer multiples of the distance between basal planes (6.708 Å). In contrast, the features on the sputtered surface range in size from

100 Å to 1000 Å and appear 'hill' and 'pit' like. Close examination of these features indicates that many of the edges of the structures appear to be aligned crystallographically, consistent with the supposition that the anisotropy of the graphite structure will affect the mechanism of damage. The edge site density estimated from the sputtered surface is two orders of magnitude larger than that of the cleaved surface. The differences in structure between the cleaved and sputtered surfaces may be quantitatively compared in the profiles of the figure. Note that over similar lateral scales the cleaved graphite varies 700 Å in height, while the sputtered surface varies 8000 Å.

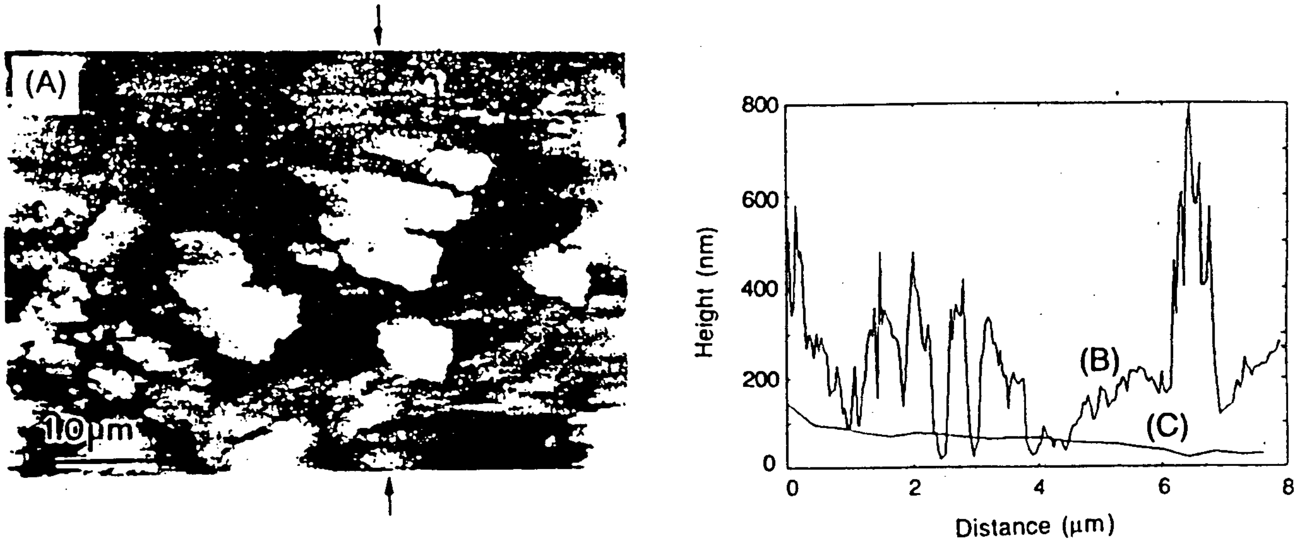

Fig. 2 (A) STM 6 mm × 8 mm constant-current topographical image of graphite after sputtering and heating to 1250 K, with full range of gray scale on the order of hundreds of nanometers. (B) Line profile extracted from (A) at the position indicated by the arrow. (C) Line profile extracted from a topographic image of cleaved graphite.

In summary, these results have provided direct spectroscopic evidence of the presence of semi-quinone functionalities on oxidized HOPG. The similarity of these observations with those of obtained from higher oxygen doses on cleaved graphite[4,5] implies that the bonding configurations of a sputtered surface are similar to the defect sites on the freshly cleaved graphite. The irreversibility of oxygen treatments suggests that some of the reactive sites due to sputtering are eliminated upon heating, or are terminated by adsorbed oxygen or hydrogen which are stable to temperatures in excess of 1200 K. Similar experiments have been carried out for plasma etched surfaces and can be found in the publications attached to this proposal[5,6].

Instrument Design for *in situ* Analysis of Film Growth

In order to unambiguously characterize local structure at different stages of reaction, a reaction chamber is needed on all analytical instruments; i.e. STM, HREELS, XPS-UPS, (all systems have LEED and Auger spectroscopy). We designed and built a portable chamber which can attach to all three systems, in which CVD reactions can be carried out. The chamber operates with a base pressure of 10^{-9} torr, allows variable reaction temperatures up to 1200°C, and contains a quadrupole mass spectrometer for gas analysis and temperature programmed desorption. The chamber is shown schematically in Fig. 3.

Deposition occurs in the top portion of the chamber where the sample transfer manipulator brings the substrate to the center of the six-way cross. Here, the substrate is heated and exposed to reactant gases. Temperature is monitored from above via a pyrometer. After deposition, the sample travels forward through the opposite port and into one of the characterization chambers. Chamber vacuum (10^{-8} Torr) is maintained with an ion pump at the bottom of the chamber. A turbo pump is attached to aid in initial evacuation. The second cross, below the point of deposition allows an ion gauge and a residual gas analyzer to be attached. The gases are prepared in a manifold where the pressure is monitored by a thermocouple gauge. Gases are injected into the chamber through a leak valve equipped with a stainless steel tube which allows gasses to be admitted one inch above the substrate. The sample is contained in a Ta 'boat' which can be resistively heated. The 'boat' is part of a specimen holder which is maneuvered by a magnetically coupled linear transfer manipulator capable of 360° rotation and extension of twelve inches.

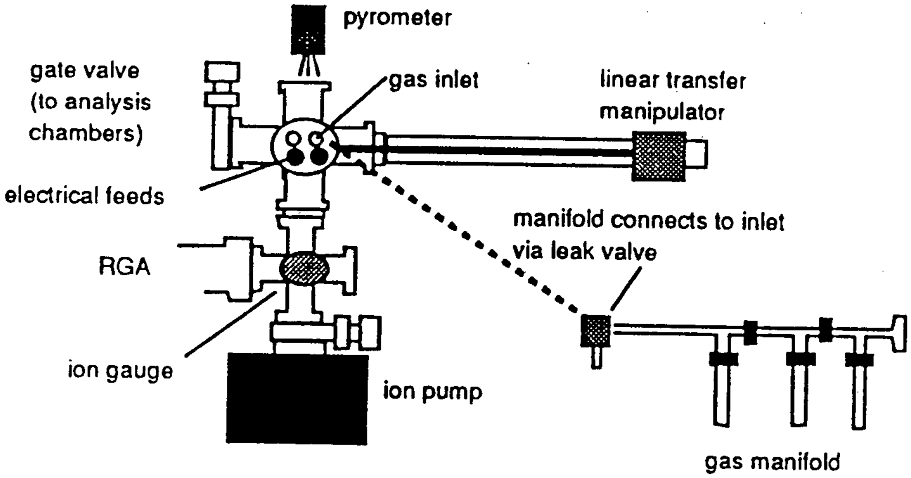

Fig. 3 Schematic of Reaction Chamber

Although not directly supported by this project, expanding STM scan range is critical to its success. Two approaches have been taken to expand the scan range and positioning capability of one of our STMs. The first involves a design which utilizes piezo block translators with a maximum travel of 50 μm for lateral movement of the tip, and of 15 μm for the vertical motion. The resolution of the long range STM is 25 Å laterally, and 7.5 Å vertically. Different areas of large samples can be imaged by positioning the tip which is magnetically coupled to the stage. Sample areas as large as 6.5 cm^2 can be accommodated in this manner. Tip-sample approach is accomplished via an electrostrictive device. This microscope operates in air or moderate vacuum.

Our second approach to improving the limited range of STM is through the design and construction of a SEM/STM which operates in UHV and has large scale positioning capability (> 1 cm). This configuration allows visual observation of sample-tip approach and tip positioning. The system allows imaging with secondary electrons, STM imaging and spectroscopy, Auger and LEED capabilities, along with *in situ* sample and tip exchange and sputtering and gas dosing. Although a few groups and companies have developed combination STM/SEM, they are either in a relatively low vacuum or do not allow large scale positioning.

Initial Stages of SiOx Deposition

In order to examine the initial stages of deposition of potential protective coatings on carbon, we attempted to deposit small amounts of SiO_x and BO_x on graphite. Fuller descriptions and a more comprehensive literature review can be found in the attached publications. It was only possible to deposit a boron oxide film in a small window of temperature/pressure phase space, consistent with the thermodynamic properties of boron oxide. CVD of Silica was achieved via thermal decomposition of tetraethoxysilane (TEOS). The results of various reaction conditions for silica deposition via decomposition of TEOS are summarized in the Fig. 4.

The results of TEOS temperature programmed desorption experiments can be summarized as follows. Molecular TEOS desorbs from the surface in a peak centered at -80 °C, while chemisorbed species remain intact to 225 °C where they react to produce ethanol and ethylene. AES analysis indicates that only a small amount of SiO_x is deposited during the first TEOS TPD experiment on a freshly cleaved surface. Following subsequent TPD experiments only the low-temperature molecular TEOS desorption peak was observed and no significant increase in the amount of SiO_x on the surface was detected. These results suggest that the sites which are most active for TEOS reaction were passivated during the first TPD cycle, consistent with expectations[7].

HREEL spectra were collected following exposure of the substrate to 6 L of TEOS at -180°C are displayed in Fig. 5. Peaks are evident in the spectrum obtained following TEOS exposure at 487, 809, 975, 1108, 1435, 2230 and 2970 cm^{-1}. By comparison to previously reported HREEL spectra of TEOS-dosed surfaces[8], these peaks can be assigned to the d(Si-O), n(Si-O), n(C-C), n(C-O), d(CH3), n(C-O) first overtone, and n(C-

H), respectively. The positions and relative intensities of the peaks are consistent with the presence of multilayers of molecular TEOS on the surface. Heating the TEOS-dosed surface to 25°C to ensure that only chemisorbed species remained, produced several changes in the HREEL spectrum. These include shifts in the positions of the d(Si-O) and n(Si-O) modes to 421 and 800 cm^{-1}, respectively, an increase in the intensity of the n(C-H) mode and a shift in its position to 2930 cm^{-1}. The v(C-C) mode was no longer resolvable after heating to 25°C. The exact structures of the adsorbed species at this temperature cannot be determined; however, the changes in peak positions and relative intensities indicate that either the configuration of the adsorbed TEOS is distorted from that of the free molecule or it has dissociated. Dissociation would most likely result in the formation of adsorbed ethoxy [CH_3CH_20-] and ethoxysilane species [Si-$(OCH_2CH_3)_n$, n = 1..3].

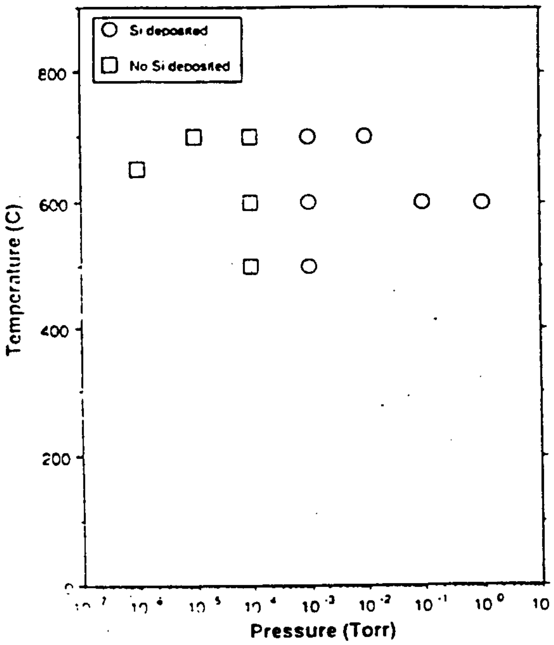

Fig. 4 Summary of TEOS reaction conditions

Heating the TEOS-dosed sample to 225°C resulted in a marked decrease in the intensities of all of the peaks, consistent with the TPD results which showed that adsorbed TEOS decomposes near 225°C to produce gaseous ethylene and ethanol. The presence of a small d(CH_3) peak in the spectrum centered at 1430 cm^{-1} demonstrates that decomposition of the adsorbed species is not complete and that some ethoxy groups remain on the surface. In addition to the decrease in peak intensities, several other changes occurred upon heating to 225°C. These include the disappearance of the d(Si-O) mode at 421cm^{-1} and the appearance of a new peak at 400 cm^{-1}, and a shift in the position of the n(C-O) mode from 1108 to 1120 cm^{-1}. These changes can be attributed to decomposition of a portion of the ethoxy ligands and the formation of Si-

O-Si linkages. The HREEL spectrum of molecules containing siloxane bridges generally contain three normal modes centered at approximately 400, 800, and 1120 cm^{-1}. Thus, the peak at 400 cm^{-1} may result from excitation of one of these siloxane normal modes. The large peak at 1120 cm^{-1} most likely contains contributions from both a Si-O-Si mode expected at this frequency and the n(C-O) mode of the remaining ethoxy ligands. The spectrum obtained after heating to 625°C contains three peaks centered 424, 820 and 1120 cm^{-1} which can be assigned to the normal modes of SiO_x.

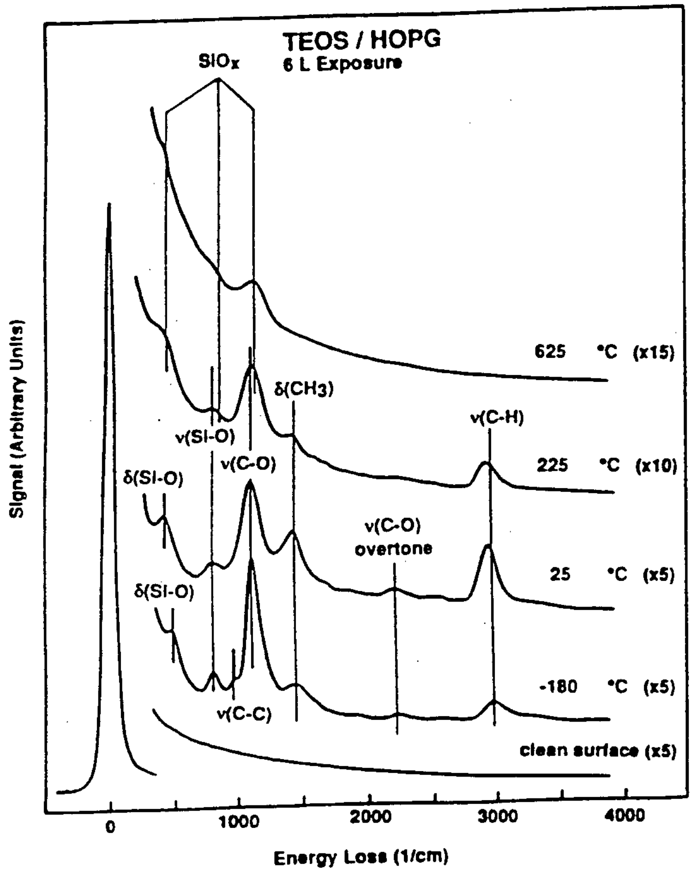

Fig. 5 HREEL spectra of clean HOPG basal surface, the basal surface following a 6 L exposure of TEOS at -180°C, and following subsequent heating to 25, 225, and 625°C

One of the factors crucial to the efficacy of the deposited film is the atomic bonding at the SiO_x-carbon interface. In order to characterize the compositional variations at the interface and in the films, AES depth profile analyses are presented. Relative concentrations of elemental silicon (92 eV), oxidized silicon (76 eV), oxygen (510 eV), and carbon (272 eV) are shown in Fig. 5 as a function of position. At the surface, the relative concentration of oxidized silicon is a factor of three higher than that of elemental silicon. The amount of oxidized silicon decreases and the amount of elemental silicon increases with distance into the film until the relationship is reversed. Consistent variations in oxygen concentration occur. This suggests that the reaction layer consists of SiO_x in the film and Si-C bonds at the film-substrate interface. The significant carbon signal at the surface and the presence of Si after long sputtering times indicate that some of the surface remains unreacted and that the thickness of the reactant layer varies.

Rutherford backscattering spectra (RBS) provide further evidence that the SiO_x film does not cover the entire surface. The RBS spectrum from a basal plane exposed to TEOS at low pressure is shown in Fig. 6. Silicon is detected at 1.2 MeV, oxygen at 0.85 MeV, and carbon at 0.62 MeV. Note that peaks detected at the silicon and oxygen energies are narrow, in contrast to the edge exhibited by carbon. The shape of these peaks indicates that silicon and oxygen are surface species, i.e. they are not detected in the bulk. The fact that the carbon edge is at 0.62 MeV, i.e. does not exhibit an energy loss, indicates that silicon does not completely cover the surface. Furthermore, the ratio of silicon to oxygen is estimated from this data to be 1:3.5. Since the highest ratio that can be accommodated by silica is 1:2, the excess oxygen must arise from oxygen termination of some of the exposed carbon, further evidence of incomplete silica coverage.

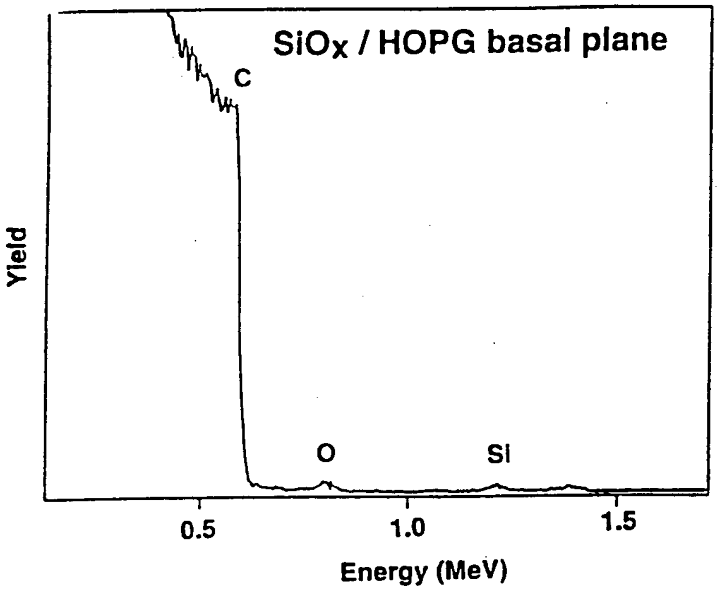

Fig. 6 RBS spectrum of SiO_x deposited on the basal plane of HOPG

STM was used to characterize the topographies of SiO_x films deposited on the basal plane. Figures 7 and 8 display both large and small scale constant current images of the various surface features observed after SiO_x deposition. The surface morphology after a long exposure to TEOS at high pressure consists of island-like features which vary in diameter from 1 to 8 mm and have heights on the order of 0.2-0.4 mm. The islands are separated by 1-5 mm, giving the appearance of coverage on the order of 40%; however, smaller, scale inhomogeneously distributed features are observed between these islands. The morphology after low pressure exposure consists of island-like features that are 0.1 - 0.8 mm in diameter, and are separated by 0.2-2.0 mm, giving the appearance of a much lower coverage than that observed in the high pressure sample. Higher resolution imaging of these surfaces, reveals homogeneously distributed features on the order of several nms in lateral and vertical dimension. On both samples the tunneling current was less stable over regions with high densities of large islands than over those appearing flatter. This behavior indicates that deposits are not very conductive.

In summary, the initial stages of the deposition of a silicon film via thermal decomposition of TEOS onto graphite basal planes were examined The compositional variation with reactant thickness indicates that carbon is bonded to silicon rather than oxygen and that SiO_x develops beyond the Si-C bond. All processing conditions resulted in inhomogeneous reaction, consistent with the theory that the initial reactions occur at unsaturated carbon bonds (i.e. defect sites). Once the TEOS reacts at surface defect sites and nucleates a SiO_x deposit, the SiO_x film grows upon itself, developing into islands as illustrated by the STM images. The nm scale features of the surface morphology depend upon the processing conditions.

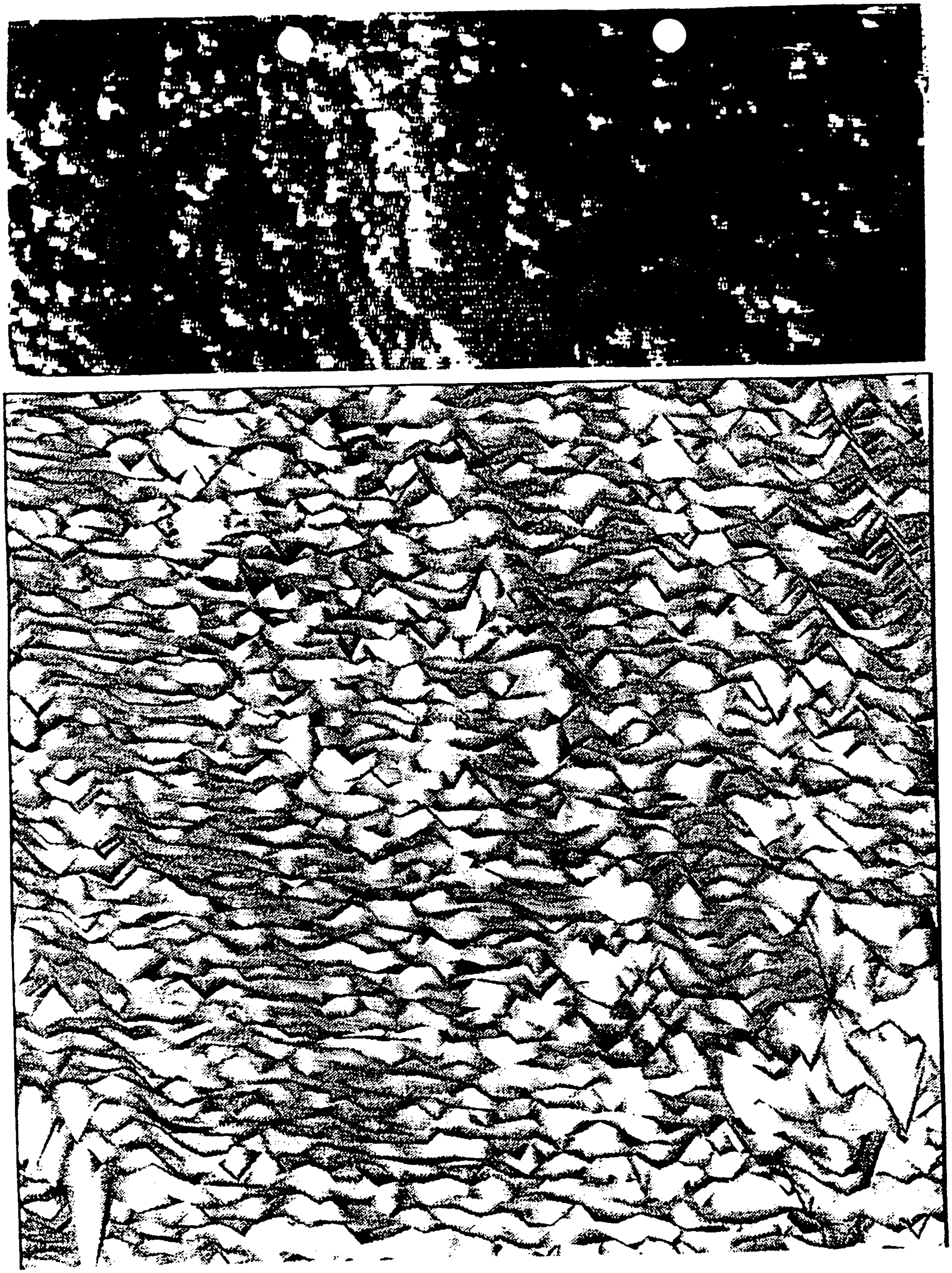

Fig. 7 Constant current STM image of SiO_x deposited on basal plane graphite under low pressure short exposure, top: 7.2 µm x 20 µm, vertical scale 1 µm, bottom: 150 nm x 150 nm area, vertical scale 10 nm, current 1 nA, bias 10 mV.

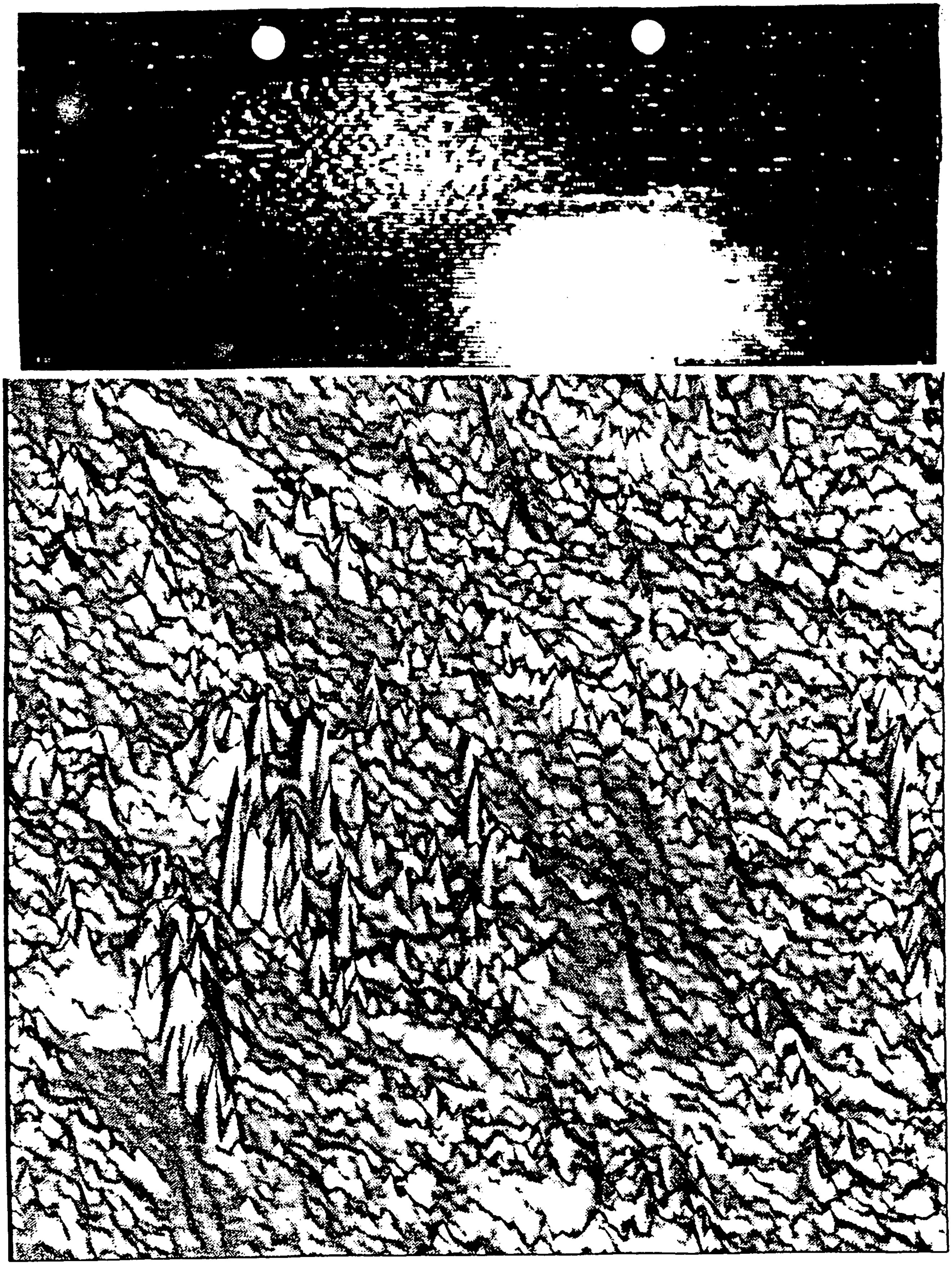

Fig. 8 Constant current STM image of SiO_x deposited on basal plane graphite under high pressure long exposure conditions, top: 7.2 μm x 20 μm area with 5 μm vertical scale, bottom: 150 nm x 150 nm area, 19 nm vertical scale, current 1 nA, bias 50 mV.

Program Productivity Summary

Status of Students supported by this program

Michelle Hoveland	MS Dec. 1992	"Initial Stages of Deposition of SiOx on Graphite"
Marilyn Nowakowski	PhD expected 12/94	"Site Specific Structure and Reactivity of Defects in Carbon"
Darren Jiron	MS May 1994	"Local Chemistry at Interfaces of Carbon and Coatings"

Instrumentation Development within this program

Rigid STM Head, tube scanner with inertial approach system
Portable High Vacuum CVD Chamber, described earlier
Approach System for the SEM/STM

(All three have been designed, constructed, and calibrated and are now fully operational and in use.)

Dissemination of Results through Presentations at Meetings

American Ceramic Society, (April 1991)
Materials Research Society, Boston, MA (November 1991)
American Ceramic Society, (April 1992)
Gordon Conference on Science of Ceramics New Hampshire (August 1992)
Materials Research Society, Boston, MA (November 1992)
American Ceramic Society (April 1993)
MRS Meeting (April 1993)

Dissemination of Results through Publications

Effect of Sputtering and Plasma Etching on the Reactivity of Carbon
M. Nowakowski, D. A. Bonnell *J. Am. Ceram. Soc.* 76 (1993) 279.

Initial Stages of SiO_x Deposition on Graphite
M. Hoveland, J. Vohs, D. Bonnell *J. Mat. Res.*, 9, No. 4 (1994) 933-939.

Surface Reactivity of Oxygen on Cleaved and Sputtered Graphite
M. Nowakowski, J. Vohs, D. Bonnell *Surface Science* 271 (1992) L351-356.

Phase Evolution and Structure of TiN/TiB_2 Nanocomposites from Polymeric Precursors
M. Nowakowski, V. Szabo, K. Su, M. Ruhle, L. Sneddon, D. Bonnell Proceedings of the Materials Research Society Meeting (1993).

Morphological Development in TiN/TiB2 using Energy Filtered TEM
V. Szabo, M. Nowakowski, K. Su, M. Ruhle, L. Sneddon, D. Bonnell Proceedings of the Materials Research Society Meeting (1993).

Synthesis, Microstructural Evolution, and Properties of TiN/TiB2 Nanocomposites
M. Nowakowski, V. Szabo, K. Su, M. Ruhle, L. Sneddon, D. Bonnell, submitted to
J. Am Cer. Soc.

Polymer Precursor Routes to TiB_2/TiN Nanocomposites
K. Su, M. Nowakowski, D. A. Bonnell, L. Sneddon *Chemistry of Materials* 4 (1992) 1179.

At least two more papers are in preparation.

---

[1] R. J. Purtell, M. Pomerantz, "Electron Energy Loss Spectroscopy of Real Surfaces", Langmuir 7 (1991) 2443.

[2] R. E. Palmer, J. F. Annett, R. F. Willis, "Loss Structure in the Electron Energy Loss Exicitations Continuum of a Semimetal" Phys. Rev. Lett. **58** (1987) 2490. .

[3] B. Marchon, J. Carrazza, H. Heinemann, G. Somorjai, "TPD and XPS Studies of O2, CO2, and H2O in Clean Polycrystalline Graphite" *Carbon* **26** (1988) 507.

[4] B. Marchon, W. Tysoe, J. Carrazza, H. Heinemann, G. Somorjai, "Reactive and Kinetic Properties of CO and CO2 on a Graphite Curface" *J. Phys. Chem.* **92** (1988) 5744.

[5] M. Nowakowski, J. Vohs, D. Bonnell, "Effects of Sputtering and Plasma Etching on the Surface Reactivity of Graphite" *J. Am. Ceram. Soc.* **76** (1993) 279.

[6] M. Nowakowski, J. Vohs, D. Bonnell, "Surface Reactivity of Oxygen on leaved and Sputtered Graphite" *Surf. Sci. Lett.* **271** L351 (1992).

[7] W. Hoffmann, private communication.

[8] J. Danner, M. Rueter, J. Vohs, "Pathways and Intermediates in the Reaction of TEOS on Si(100) 2x1" *Langmuir* 9 455 (1993).

APPENDIX 1

Reprints

SYNTHESIS, PROCESSING AND PHASE EVOLUTION OF TiN/TiB_2 COMPOSITES FROM POLYMERIC PRECURSORS

M. NOWAKOWSKI, K. SU*, L. SNEDDON*, D. BONNELL
Department of Materials Science and Engineering
*Department of Chemistry
The University of Pennsylvania, 3231 Walnut St., Philadelphia, PA 19104

ABSTRACT

High yield synthetic route to TiN/TiB_2 nanocomposites based upon polymeric precursors has been developed. The phase evolution and microstructural development have been characterized and related to preliminary measurements of properties, i.e. hardness. The observations indicate the existence of TiN-TiB_2, TiN-BN, and TiB_2-BN subsolidus compatibilities.

INTRODUCTION

Recent developments of polymeric precursors to ceramics have been motivated by the potential for strict control of stoichiometry, for complex shape forming, and for low temperature processing. These advantages have spurred the development of a number of polymeric synthetic routes to ceramics, one of the most visible being the commercialization of the polycarbosilane-to-SiC reaction to form fibers. The molecular level control of chemistry inherent in this approach could be exploited to produce ceramic composites with fine morphological structure, perhaps on nanometer scales.

Although most studies of preceramic polymers have been centered on silicon-based polymers, a number of boron-based polymer systems have also been shown to produce ceramics, including BN and B_4C, upon pyrolysis.[1] These polymers have exhibited properties important to potential applications such as coatings in structural ceramic composites, wear resistant films, oxidation-resistant fibers and high temperature electronics. The use of preceramic polymers as reactants to esize other ceramics, such as metal boride, nitride and silicide has also been reported.[2-3] by taking advantage of the formability of the polymer, a near net shape ceramic might be obtained. Among boron-based ceramics, metal boride and nitride are of special interest because of their high melting points, hardness and chemical inertness at high temperatures. We recently demonstrated that the synthesis of monolithic TiB_2/TiN composites can be achieved by a process based on the reaction of polyborazylene with titanium metal powder.[4]

In order to control the properties of the composites, an understanding of the morphological development and the relationship between microstructure and properties, as well as the synthesis of the polymeric precursor is required This paper presents synthesis, processing and phase evolution of TiN/TiB_2 from polyborazylene and Ti. Morphological characterization presents challenges associated with the small grain size and light element variations that are met with an energy loss imaging technique. Both the technique and the microstructural development are discussed in a separate paper in this issue.[5] Experimental details related to processing and characterization are first summarized, then synthesis strategies and results are presented. Phase evolution is documented and implications to subsolidus phase compatibilities are discussed. Finally the results are summarized with respect to implications to thermodynamics and processing parameters.

Mat. Res. Soc. Symp. Proc. Vol. 286. ©1993 Materials Research Society

EXPERIMENTAL PROCEDURES

Polyborazylene was prepared according to the usual method.[6] All manipulations of the preceramic materials were carried out with standard high vacuum or inert-atmosphere techniques. Pyrolysis under 2000°C was performed in a Linberg Tube Furnace under argon atmosphere, while pyrolysis at 2000°C was achieved in a graphite resistance furnace (Astro Industry Hot Press Model 1000-3070 HP) under vacuum. In a typical process, 34.32 g of titanium metal (325 mesh, Strem Chemicals) was added to a dry tetrahydrofuran solution containing 14.2 g polyborazylene. The solvent was then vacuum evaporated while maintaining ultrasonic agitation. The resulting black solid dispersion was ground to a fine powder under a nitrogen atmosphere. Two to four grams of precursor powder were isostatically pressed at 75,000 psi. The resulting green bodies were divided into two groups. Group 1 samples were heated (2°C/min) to 800°C and held for 9.5 h under an argon atmosphere. After being cooled to room temperature, the ceramic bars were annealed at higher temperatures as summarized in Table 1. Group two samples were not cooled between the reaction and annealing steps.

Two powder samples were also reacted. A 0.74 g sample of powdered solid dispersion was heated (2°/min.) to 800°C and held for 9.5 h under Ar. Yield: 0.69 g; Ceramic yield: 88.5%. Elemental analysis: Ti: 65.8%; B: 9.80%; N:.12.3%; O: 8.58%; C: 0.66%; H: 0.70%. In another experiment, a 0.78 g same preceramic sample was heated (10°C/min.) to 1450°C and held for 10 h under Ar. Yield: 0.69 g; Chemical yield corresponding to metal: 91.8%; Ceramic yield: 88.5%. Elemental Analysis: Ti: 73.4%; B: 8.31%; N: 12.2%; O: 2.91%; C: 2.66%; H: < 0.1%.

Table 1 Summary of Reaction Conditions:

Sample	T (°C)	Time (h)	Cer. yield (%)	d (g/cm^3)
No. 1	800	9.5 (only)	99.1	2.98
No. 2	1000	2	96.0	3.47
No. 3	1200	2	95.5	3.81
No. 4	1450	2	91.9	3.90
No. 5*	2000	2	88.6	3.63
* 5 was annealed in vacuo, while 2–4 were under Ar.				
No. 2-1	870	1.0	98.0	2.59
No. 2-2	1000	1.0	98.2	2.82
No. 2-3	1000	3.8	98.8	3.16
No. 2-4	1000	49.0	99.5	3.29
No. 2- 5	1200	1.0	97.5	3.49
No. 2-7	1200	3.0	98.4	3.73
No. 2-6	1200	67.5	98.6	3.70
No. 2-7*	1200	126.0	96.1	4.18
No. 2-8	1450	1.0	94.9	4.13
No. 2-9	1450	17	91.6	3.49

X-ray powder diffraction spectra were recorded on a Rigaku Geigerflex X-ray diffractometer using Cu Kα radiation. Quantification of the relative phase amounts was accomplished using silicon powder as a standard. The uncertainty due to measurement error is less than 2%. Scanning electron microscopy (SEM) micrographs were obtained on a Phillips 500X scanning electron microscope. Densities were measured by water displacement method. Elemental analyses were performed by Pascher, (Postfach 2129, 5480 Remagen 2, Germany). Hardness was measured by microindentation with a diamond shaped indentor and was calculated according to the usual relation:

$H = P/2a^2$, where P is the load, a is the half diagonal of the indentation.

RESULTS AND DISCUSSION

We have previously reported the preparation of the new boron-nitrogen polymer, polyborazylene, $(B_3N_3H_4)_x$, and shown that this polymer can be converted to boron nitride in high ceramic and chemical yields (90-94%).[2] We have also demonstrated a new, potentially general route to metal borides, such as TiB_2 and ZrB_2, involving the reduction of the corresponding metal oxide with a boron-carbon based polymer (decaborane-dinitrile). Taken together these results suggested that the reactions of a metal with polyborazylene might lead to incorporation of both polymer boron and nitrogen atoms to produce new composite metal-nitride/metal-boride materials which might have improved properties over an individual metal boride or nitride. The final product could be either in powder or monolithic form depending on the processing conditions. Since polyborazylene functions as both a reactant and a binder in this system, a green body can be readily made by isostatic pressing at room temperature. The yrolysis of the green body yielded a composite that exhibited excellent shape retention with final nsity dependent upon the annealing temperature and time. An increase in density from 2.98 to 3.90 observed in group 1 samples is associated with increases in annealing temperatures (for constant times) from 800° to 1450°C. In contrast, a decrease in density from 4.13 to 3.94 for samples treated at 1450°C for 1 h and 17 h was found. It is believed that the decrease in density results from the evaporation of B_2O_3 and NO at temperature above 1200°C. The ceramic

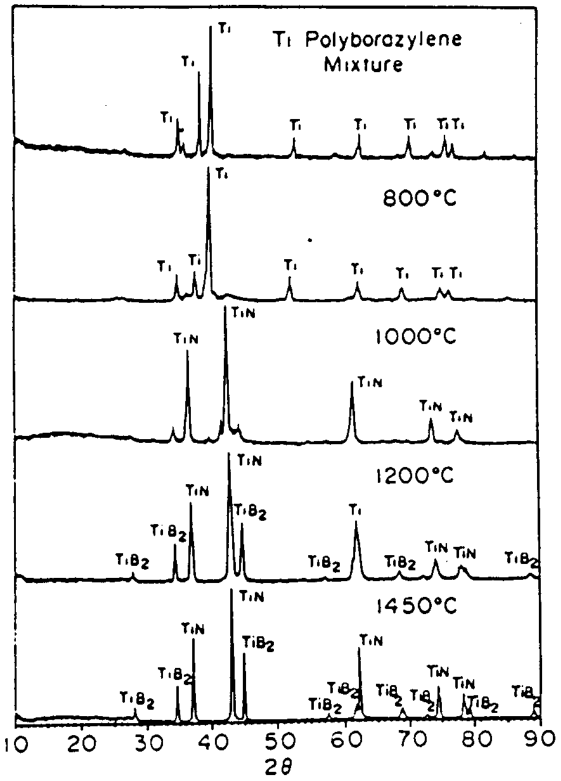

Figure 1. X-ray diffraction patterns of samples heated for 16 hrs at the temperatures shown. At 800 C, only Ti metal and amorphous phase are present. At higher temperatures both TiN and TiB_2 are present.

powders prepared at 800°C and 1450°C have compositions of $Ti_{1.0}B_{0.66}N_{0.64}H_{0.51}O_{0.39}C_{0.04}$ and $Ti_{1.0}B_{0.50}N_{0.57}H_{0.06}O_{0.1}C_{0.14}$, respectively. The 1450°C material is consistent with a $(TiN)_{0.57}(TiB_2)_{0.25}Ti_{0.18}O_{0.1}C_{0.14}$ mixture. Both nitrogen and boron contents have decreased for 1450°C materials compared to those of the 800°C materials suggesting that the reduction of TiO_2 involves both nitrogen and boron.

X-ray diffraction documented the variations in phase content with processing temperature and/or time. Thus, as can be seen in Figure 1, there appears to be little reaction between the polymer and the titanium metal when the sample was heated at 800°C for 9.5 h. Consistent with this conclusion, elemental analyses of a sample at this point showed that the material still had a significant hydrogen content with the observed $B_{1.03}:N_{1.0}:H_{0.79}$ ratio suggesting that polymer crosslinking was still occurring. When the sample was heated at 1000°C for 2 h, the titanium metal is consumed by reaction with the polymer and crystalline titanium nitride is initially observed to form. The pattern shown in the figure obtained from the the sample annealed at 1200°C for 2 h clearly indicates the presence of both crystalline TiB_2 and TiN. The decrease in line widths in the pattern from the 1450°C sample is consistent with an increase in the average grain size. Although not detected in the X-ray diffraction pattern, TEM imaging provides evidence that some BN crystallizes during the reaction.

The phase assemblages from different processing conditions are shown in Figure 2 which compares intensities of the primary peaks of each phase at the times and temperatures listed in Table I. Note that for all temperatures investigated TiN and TiB_2 appear to crystallize simultaneously in a 2:1 ratio. Some deviation occurs on very long anneals (50 hrs or 120 hrs for 1000 °C and 1200 °C, respectively), after which the TiN content is somewhat increased as the system equilibrates with a ratio of 2.27:1.

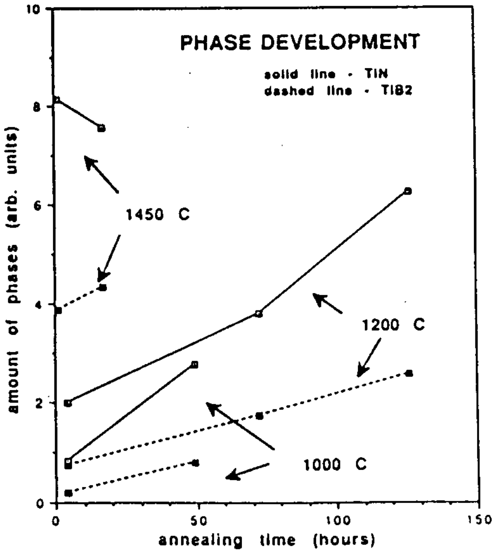

Figure 2. Crystallization of TiN and TiB_2 at various temperatures.

If one assumes that H volatilizes immediately, then the fact that all processing conditions result in two crystalline phases, TiN and TiB_2, suggests that a TiN-TiB_2 tie line exists in the Ti-B-N equilibrium phase diagram. Further evidence for the existence of this tie line is that small deviations in composition around the proposed tie line result in BN, which further implies the TiB_2-BN and TiN-BN compatibilities. The proposed relationships are shown schematically in Figure 3. This is in apparent contradiction to the work of Matsudaira et al who find that the solid state reaction of amorphous B and TiN does not proceed in a N overpressure but yields TiB_2 in an Ar overpressure. Their result implies the existence of a tie line between TiN and B. The contradiction would be resolved if one, or both experiments access metastable compatibilities. It is also possible that Matsudaira et al [7] were not able to detect BN in xray patterns since the highest intensity peak would be hidden by the amorphous B diffraction. (We also did not detect BN in the x-ray analysis but did observe it with energy filtered TEM, as discussed in ref. 5.) A more fundamental difference between the two results lies in the nitrogen activity. The phase equilibria will obviously be dependent on nitrogen activity, as emphasized by this earlier work, and diagrams such as figure 3 represents sections of constant N activity. However, regardless of the consequent uncertainty to the BN-TiN-N section of the diagram, the TiN-BN-B-Ti sections should not be affected unless mass is lost to the system as a result of changing N atmosphere.

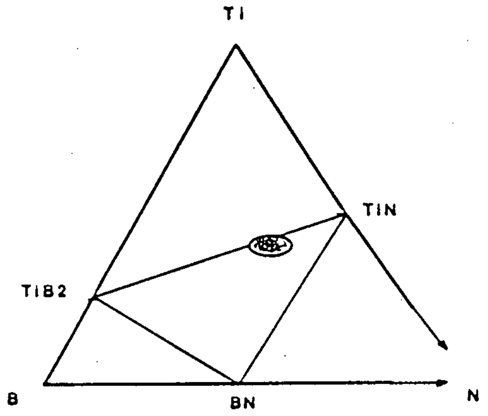

Figure 3. Schematic diagram of the subsolidus phase compatibilities indicated by the phase analyses. Shaded region represents the composition range of the samples.

In all samples a microstructure developed that appears to be characteristic of this system. The TiB_2 grains are on the nm scale, while the TiN grains are angular and on the order of 1 μm in diameter. Since all of the grains are relatively small, the phases could not be distinguished by conventional dark field imaging. Since the chemical difference resides in the light element content, EDAX could not be used to distinguish the phases. However, ESI allowed identification of the morphology of the various phases.

Preliminary measurements of hardness, listed in Table II, indicate that the TiN-TiB_2 composites made from the polymer precursor described here exhibit hardnesses much lower than that previously reported for TiB_2. Porosity in the samples resulted in a large scatter in the measurements; therefore, possible trends with phase content could not be confirmed. However, within sets of samples processed at a single temperature the hardness did increase with density. Thus, further work on this system is indicated.

SUMMARY

In summary, a high yield synthetic route to TiN/TiB_2 composites based upon polymeric precursors has been developed. The process does not involve ammonia. Phase evolution and microstructural analysis have shown that the nitride and boride phases have very different morphologies and, provide evidence for the existence of a TiN-TiB_2 compatibility in the TiN-TiB_2-BN system. Preliminary hardness measurements suggest that fully dense composites will exhibit good wear resistance.

Table II. Properties of TiN/TiB_2 Composites

Sample	Rel. Density	Hardness
2-2	56%	0.7 GPa
2-3	63%	2.3 GPa
2-4	66%	1.3 GPa
2-5	70%	1.6 GPa
2-6	75%	1.6 GPa
2-7*	84%	1.9 GPa
2-8	83%	1.0 GPa
2-9	70%ø	0.5 GPa

Acknowledgements
This work was supported by Air Force Office of Scientific Research (DB and MN), the Department of Energy, Division of Chemical Sciences, Office of Basic Energy Sciences and the National Science Foundation Materials Research Laboratory at the University of Pennsylvania (LS and KS).

REFERENCES

1 K. Wynne, R. Rice *Annual Rev. Mat. Sci.* **14** (1984) 297-334.
2 S. Yajima, *Am. Ceram. Soc. Bull.* **62** (1983) 893.
3 (a) Paine, R. T.; Narula, C. K. *Chem. Rev.* **90** (1990) 73-91.
(b) L. G. Sneddon, M. G. L. Mirabelli, A. T. Lynch, P. J. Fazen, K. Su, J. S. Beck. *Pure and Applied Chemistry* **63**, (1991) 407-410.
4 D. Seyferth, N. Bryson, D. P. Workman, C. A. Sobon. *J. Am. Ceram. Soc.* **74** (1991) 2687-2689.
5 (a) Greil, P.; Seibold, M. *Ceram. Trans.* **1991**, *19*, 43-49.
(b) Greil, P.; Seibold, M. *Adv. Mater. Processes, Proc. Eur. Conf.* Exner, H. E.; Schumacher, V. Eds., DGM Informationsges: Oberursel, 1990; vol. 1, p 641-646.
(c) Greil, P.; Seibold, M. *J. Mater. Sci.* **1992**, 27, 1053-1060.
6 K. Su, M. Nowakowski, D. Bonnell, L. Sneddon *Chem. Mater.* 4 (1992) 1139-1141
7 V. Szabo, M. Nowakowski, K. Su, L. Sneddon, M. Ruhle, D. Bonnell, this volume.
8 Shriver, D.F.; Drezdzon, M. A. *Manipulation of Air Sensitive Compounds*; 2nd Ed., Wiley: New York, **1986**.
9 P. J. Fazen, J. S. Beck, A. T. Lynch, E. E. Remsen and L. G. Sneddon. *Chem. of Mater.* 2 (1990) 96-97.
10 T. Matsudaira, H. Itoh, S. Naka, H. Hamamoto, M. Obayashi, J. Mat. Sci. **23** (1988) 288-292.

Reprinted from the Journal of the American Ceramic Society, Vol 76, No. 2, February 1993

journal

Surface Eng ering of Structural Ceramics

J. Am. Ceram. Soc., 76[2] 279–83 (1993)

Effects of Sputtering and Plasma Etching on the Surface Reactivity of Graphite

Marilyn J. Nowakowski,*,• John M. Vohs,† and Dawn A. Bonnell*,•

Department of Materials Science and Engineering and Department of Chemical Engineering,
University of Pennsylvania, Philadelphia, Pennsylvania 19104

The surfaces of highly oriented pyrolytic graphite (HOPG) samples were treated using two different methods, exposure to an energetic oxygen ion beam and immersion in an oxygen ion plasma, and the reactions which occur during treatment were characterized using high-resolution electron energy loss spectroscopy (HREELS), temperature programmed desorption (TPD), and scanning tunneling microscopy (STM). Both surface treatments result in similar oxidation species. The results of this investigation provide spectroscopic evidence for the presence of semi-quinone functionalities on sputtered and oxidized HOPG. STM images are presented to quantify the increase in defect sites after oxygen ion sputtering and to correlate defect site density with reactivity.

I. Introduction

GRAPHITE fibers and carbon–carbon composites have a wide variety of high-temperature applications; however, application of these materials is limited by their chemical instability in oxidizing environments. Successful application invariably involves surface modification. While deposition of protective coatings is the most prevalent surface treatment, chemical, electrochemical, and plasma etching are used in some applications.[1-6] To fully exploit the potential of carbon-based materials a detailed understanding of atomic interactions involved in these processes is necessary.

To this end, a variety of techniques have been used to characterize these oxidative processes including temperature programmed desorption (TPD), photoelectron spectroscopy (XPS and UPS), Auger electron spectroscopy (AES), X-ray diffraction (XRD), scanning electron microscopy (SEM), and, more recently, scanning tunneling microscopy (STM).[5-10] This work has established that the basal plane of graphite is relatively unreactive toward molecular oxygen, while step edges and defects in these planes may oxidize more readily.[11] Furthermore, the rate of oxidation at the edges of the basal planes is sensitive to the local structure of the edge site. Recent TPD observations suggest that both semi-quinone and lactone species terminate defect sites on oxidized surfaces of graphitic particles.[8] Similar assignments have been based on Fourier transform infrared spectroscopy (FTIR) and XPS of graphitic fibers.[2-15] The work, to date, has focused primarily on reaction kinetics, rather than on specific reaction mechanisms of carbon oxidation.

The objective of the present study is to provide direct observations of the interaction occurring during surface treatment of carbon. Specifically, the effects of oxygen ion sputtering and oxygen plasma etching of graphite are probed using high-resolution electron energy loss spectroscopy (HREELS) and STM. Highly oriented pyrolytic graphite (HOPG) was chosen as the model system so that correlations with atomic geometries of defects can be made in the future. Few studies exist in which carbon has been characterized by HREELS,[16,17] and these are primarily concerned with mechanisms of electron scattering from graphite surfaces. In contrast, a large literature has accumulated on imaging graphite with STM,[18,19] much of it involving direct observations of the topography of graphite on an atomic scale. Formation of monolayer pits upon oxidation of the basal plane of HOPG has been observed with STM, as has the anisotropy of oxidation rates of the pit edges.[20] Together these studies demonstrate the potential of a systematic study of carbon surface interactions using HREELS and STM, in conjunction with conventional surface analytical methods.

HREELS and TPD spectra of sputtered and plasma-etched graphite are described. The surface functionalities resulting from these processes are compared to those proposed as products of oxidation of graphitic particles.[8] The effect of sputtering and plasma etching on the topographic structure of graphite is quantified by STM. Implications to oxidation mechanisms are discussed.

II. Experimental Procedure

TPD and HREELS were performed in an ultrahigh-vacuum (UHV) chamber with a base pressure of 1×10^{-10} torr (1 torr ~ 1.33×10^2 Pa) which included a quadrupole mass spectrometer (UTI 100C, Milpitas, CA), a high-resolution electron energy loss spectrometer (McAllister Technical Services, Coeur d'Alene, ID), and a cold-cathode ion gun (VG Instruments, Inc., Danvers, MA). A tantalum foil sample holder, in which the HOPG samples were mounted, was spot-welded to the sample manipulator. A chromel–alumel thermocouple attached to the back face of the sample was used to monitor the temperature. During TPD, the sample was heated at a rate of 8 K/s by conduction from the resistively heated sample holder. The HREEL spectra were obtained using a 3-eV electron beam incident at 60° from the sample normal, with the scattered electrons collected in the specular direction.

HOPG was cleaved in air and immediately inserted into the vacuum chamber. Each sample was then heated to 1000 K to desorb any atmospheric contaminants. Both HREELS and AES indicated that the surfaces were clean after this initial heating. Two separate oxidation treatments were studied. In the first treatment, the graphite sample was exposed to an energetic beam of oxygen ions. In order to create surface defects that could react, the sample was sputtered with an oxygen ion beam for 10 min (4 kV, 1 mA). The exposure time of 10 min was chosen after evaluating the surface after various sputtering times. For example, exposure of the graphite to a 1-μA, 4-keV oxygen ion beam for a considerably longer time caused sufficient

---

R. R. Reeber—contributing editor

Manuscript No. 195698. Received May 13, 1992; approved October 19, 1992.
Supported by the Air Force Office of Scientific Research, Division of Chemistry and Materials, under Grant No. AFOSR-91-0103.
Presented at the 94th Annual Meeting of the American Ceramic Society, Minneapolis, MN, April 12–16, 1992 (Basic Science Division, Paper No. 20-B-92).

*Member, American Ceramic Society.

•Department of Materials Science and Engineering.

†Department of Chemical Engineering.

damage to the surface that the resolution of the HREELS spectra was decreased to an unacceptable level. Exposure of the sample to the ion beam for much less time resulted in insufficient change. The composition of the oxygen ion beam was not determined; however, it was most likely composed of both doubly ionized O_2 molecules and singly ionized oxygen atoms.

In the second treatment, a similarly cleaved graphite sample was immersed in an oxygen ion plasma. The chamber was filled to 10^{-1} torr with O_2, and an oxygen plasma was created by applying a voltage from a Tesla coil at an unconnected feedthrough in order to produce a voltage drop to the chamber (which was at ground). The sample was exposed to this plasma for 30 s. The oxygen plasma was assumed to have a composition similar to that of the ion beam. The difference between these two oxidation procedures is that the first employs energetic ions which have been accelerated through a voltage gradient, whereas the second involves ions which possess only thermal energy. As a comparison to the oxidized samples, the O_2 and CO reactivities of cleaved graphite were characterized.

Following HREELS and TPD, the samples were characterized by STM in air. Constant-current images (1 nA) were obtained using a W tip with a 60-mV sample bias voltage. Two STMs were used to characterize the topographic structure of the cleaved and oxidized graphite. High-resolution imaging was accomplished on a standard instrument (WA Technology, Cambridge, England) with mechanical tip approach and tube scanner. Large-area analysis was accomplished on a long-range STM with a lateral range of 80 mm, a vertical range of 10 mm, and spatial resolution of 1 nm.[22] Images were acquired at several locations in order to characterize the general morphologies of the surfaces. The topographic structures of the oxidized surfaces were compared to the structure of cleaved graphite.

III. Results and Discussion

The HREELS spectrum of the cleaved graphite surface following annealing at 1000 K is displayed in Fig. 1(A). The elastic peak intensity was found to be sharply peaked in the specular direction, indicative of a relatively flat surface. Although no losses associated with adsorbed species are present in the spectrum, the elastic peak does exhibit a broad tail that extends to high loss energies. This tail on the elastic peak has been observed in a previous HREELS study of graphite surfaces and has been attributed to excitation of electron–hole pairs.[17] For a semimetal, such as graphite, the density of states at the Fermi energy (E_f) is zero but rises both above and below E_f. Excitation of vertical transitions from the valence band to the conduction band can give rise to the energy loss continuum observed in the HREELS spectrum.

As expected, the cleaved graphite surface was found to be relatively unreactive toward O_2. An untreated sample was exposed to various doses of O_2 at various temperatures, as outlined in Table I. Included in this table are the methods used to characterize the surface reactivities. Dosing with molecular oxygen results in insignificant reaction with the cleaved graphite surface. One explanation for the lack of reactivity is the fact that the cleaved surface is very smooth on an atomic scale, with very few steps and defects. These defects are presumably necessary for oxidation. Sputtering the graphite surface with argon ions followed by dosing with O_2 at ambient temperature and with CO at various temperatures also resulted in negligible surface reaction. A widening of the HREELS elastic peak indicated that the sputtering process roughened the surface. In this case, the lack of reactivity suggests that either sputtering with argon did not result in an increased number of defects, or that molecular oxygen and carbon monoxide do not react easily with graphite even in the presence of defects. Reaction products such as CO and CO_2 were not observed in the TPD spectra following these treatments. It is interesting to compare these TPD results with those obtained previously by Marchon *et al.*[18] for oxidized graphitic particles. These authors observed CO and CO_2 as desorption products following the exposure of the particles to various doses of O_2. Similar dosing of O_2 on cleaved or argon-sputtered HOPG in the present study resulted in little interaction, suggesting that graphitic particles have an atomic configuration different from that in HOPG.

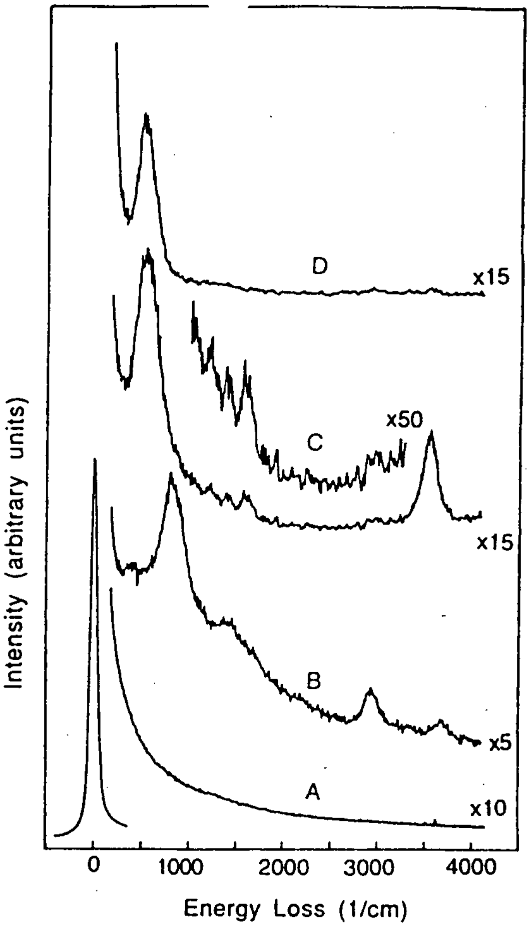

Fig. 1. (A) HREELS spectra of cleaved graphite after heating to 1000 K, (B) after sputtering with oxygen, (C) after heating sputtered sample to 1000 K, (D) after heating sputtered sample to 1250 K.

Graphite surfaces were exposed to oxygen ions created by two different methods. The first surface treatment involved sputtering with an oxygen ion beam which, in addition to providing a source of energetic atomic oxygen, also served to increase the number of surface defects and steps. HREELS spectra of the surface were collected before and after sputtering and found to be substantially different, as seen in Figs. 1(A) and (B). Several loss peaks, centered at 810, 1470, 2950, and 3650 cm^{-1}, are observed after sputtering, as is a decrease in the intensity of the elastic peak. This decrease is caused by an increase in the roughness of the surface due to the sputtering process. The loss peaks are assigned in a recent paper.[23] In general, a C–H stretching mode (2950 cm^{-1}) and O–H stretching mode (3650 cm^{-1}) are relevant to the reaction. The O–H and C–H species were most likely produced by reaction with water that was present in the background gas of the chamber while sputtering with O_2. The peaks centered at 810 and 1420 cm^{-1} result from modes other than those of carbon–oxygen bonds. The 810-cm^{-1} peak, which shifts to 530 cm^{-1} upon heating to 1000 K, most likely results from low-energy electronic transitions in the graphite surface; its existence even after extended annealing to 1250 K suggests that it is not due to an oxygen-containing species on the surface. The 1420-cm^{-1} peak corresponds to a C–H bending mode of surface hydrocarbon groups.

The desorption products from this surface were monitored up to 1000 K. The primary desorption products were CO and CO_2. The TPD spectra for these molecules are presented in Fig. 2.

Table I. Reactivity of Graphite after Various Surface Treatments

Dose*	Temp (K)	Method	Reaction
		Cleaved graphite	
O_2, 35 L	At 1000	HREELS	None
O_2, 35 L	At 1050	HREELS	None
O_2, 35 L	At 1250	HREELS	None
O_2, 175 L	At 900	HREELS	None
O_2, 1260 L	At RT	TPD	None
O_2, 120 000 L	At 1000	HREELS	None
H_2O, 56 L	At RT	HREELS	None
		Graphite sputtered with argon	
	At RT	HREELS	Roughened
O_2, 7 L	At RT	TPD	None
O_2, 35 L	At RT	TPD	None
O_2, 70 L	At RT	TPD	None
O_2, 140 L	At RT	HREELS, TPD	None, none
O_2, 600 000 L	At RT	HREELS	None
CO, 5 L	At 100	TPD	None
CO, 17 L	At 650	TPD	None
CO, 9 L	At RT	TPD	None
CO, 70 L	At RT	TPD	None
CO, 140 L	At RT	TPD	None
CO, 210 L	At RT	HREELS	O–H
CO, 175 000 L	At RT	HREELS	None
		Graphite sputtered with oxygen	
	At RT	HREELS	C═O, O–H, C–H
None	Heat to 1000	HREELS	C═O, O–H
None	Heat to 1250	HREELS	None
O_2, 350 000 L	At RT	HREELS	O–H, C–H
		Graphite in oxygen plasma	
O_2, 175 000 L	At RT	HREELS	C═O, O–H, C–H
None	Heat to 1140	HREELS	C═O

*L is langmuirs (1 L = 10^{-6} torr·s).

Carbon dioxide desorbed over a wide temperature range, with a maximum occurring at 740 K. Carbon monoxide also desorbed over a wide temperature range, with maxima occurring at 780 and 910 K. In addition to CO and CO_2, smaller amounts of H_2O and hydrocarbon species desorbed from the surface at temperatures between 300 and 500 K. Previous authors[7,8] observed CO_2 desorption peaks in the range from 433 to 900 K and CO desorption peaks at 1093 and 1253 K, with a shoulder at 973 K for graphitic particles. Based primarily on desorption activation energies calculated from TPD results, it was proposed that the CO peaks resulted from decomposition of surface semi-quinone species, while the CO_2 resulted from decomposition of surface lactones. Since our TPD peaks for CO_2 and CO fall in similar temperature ranges, it is possible that lactone and semi-quinone species account for the desorption of CO_2 and CO after sputtering with oxygen.

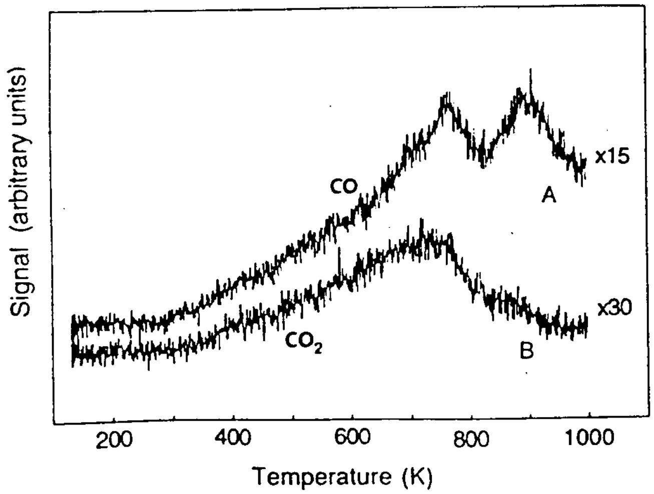

Fig. 2. (A) TPD spectra of mass 28 (CO) and (B) mass 44 (CO_2) after sputtering sample with oxygen.

Changes in the surface vibrational spectrum upon heating to 1000 K are illustrated in Fig. 1(C). One of the most noticeable changes is the almost complete disappearance of the C–H stretch at 2950 cm^{-1}, indicating the desorption of nearly all CH_x species from the surface. Other changes include the appearance of small peaks centered at 1200, 1390, and 1620 cm^{-1} and a shift in the position of the large peak previously at 810 to 530 cm^{-1}. The O–H stretching mode near 3600 cm^{-1} was relatively unchanged upon heating, indicating the continued presence of OH groups on the surface. The peak at 1200 cm^{-1} can be attributed to a C–OH stretching mode, while that at 1620 cm^{-1} is characteristic of a C═O stretching mode. It is somewhat more difficult to assign the peak at 1390 cm^{-1}; however, the most reasonable assignment seems to be the O–H bending mode of surface hydroxyl groups. These HREELS results indicate that the primary oxygen-containing functional groups on the surface after heating to 1000 K are hydroxyls and carbonyls. The presence of carbonyl functionalities is consistent with the formation of surface semi-quinone species as previously proposed. Surface functionalities assumed to be semi-quinones are stable to temperatures as high as 1273 K, much higher than the 1000 K temperature excursion of the present experiment. Surface lactone species have also been proposed to exist on oxidized graphite and would be expected to give rise to a C═O stretching mode in the HREELS spectrum. The C═O stretching mode in lactones generally occurs between 1700 and 1800 cm^{-1}.[21] The absence of this peak indicates either that surface lactones were not formed by this oxidation reaction or that they decompose at temperatures less than 1000 K. In the latter case, the CO and CO_2 peaks observed in the TPD spectra result from lactone decomposition. Final heating to approximately 1250 K results in desorption of all oxygen-containing species, as shown in (D) of Fig. 1.

Figure 3 displays the HREEL spectra of the surface before and after exposure to the plasma. Fig. 3(A), acquired after the sample was initially inserted into the chamber and heated, exhibits no peaks. As Fig. 3(B) shows, exposure to the ion plasma results in the appearance of several loss peaks. Again, the O–H peak is seen at 3650 cm^{-1}, which indicates adsorbed hydroxyl groups. Also, a peak due to the C–H stretching mode

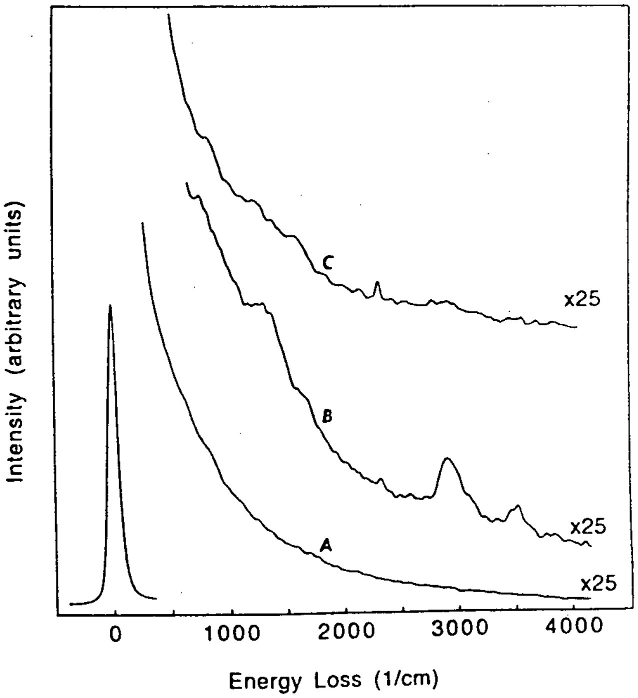

Fig. 3. (A) HREELS spectra of cleaved graphite sample after heating to 1000 K, (B) after exposing to oxygen ion plasma, (C) after heating to 1140 K.

of surface hydrocarbon species is observed at 2950 cm^{-1}. The wide peak centered around 1300 cm^{-1} probably incorporates stretching and bending modes of surface hydrocarbons and hydroxyl groups. There exists a wide shoulder in the spectrum in the 1600–1700-cm^{-1} range; energy losses in this area can possibly be due to lactones or semi-quinones, as peaks in this range are consistent with C=O bond energies in either of these species. Heating to 1140 K, as shown in Fig. 3(C), results in desorption of hydrocarbon and hydroxyl groups, yet the shoulder in the C=O range still remains, implying that stable oxidation species exist on the graphite surface above 1140 K after exposure to an oxygen ion plasma.

Spectra in Fig. 1 exhibit energy loss features in the range of 1620 cm^{-1}. Since this is consistent with the presence of C=O modes of carbonyls, these HREELS results provide direct spectroscopic evidence in support of the surface functionals described by Marchon *et al.*[8] Although these results are from the sample which was bombarded by accelerated oxygen ions, the shoulder in the HREELS spectrum at 1600–1700 cm^{-1} for the ion-plasma-treated sample suggests that both accelerated oxygen ions (from sputtering) and thermally active oxygen ions (from the plasma) result in similar oxidation species on the surface. Oxidation species appear to exist above 1140 K, as seen from the ion-plasma-treated sample, yet desorb when the sample is heated above 1250 K, as seen from the oxygen-bombarded sample. In contrast to previous work, these functionalities could not be produced by reactions with molecular oxygen. This seeming contradiction may rest on the differences in atomic configurations between "graphitic" particles and HOPG.

The impact of sputtering on the surface morphology is indicated by the increased breadth and decreased intensity of the HREELS elastic peak, which is associated with increased surface roughness. This change in roughness has been quantified using both high-resolution and large-scan STM imaging. The topographic structure of the sputtered HOPG is shown in Fig. 4. The gray scale representation is normalized to the largest feature in the image. Cleaved graphite typically contains surface steps with heights of integer multiples of the distance between basal planes (3.35 Å). In contrast, the features on the sputtered surface range in size from 10 to 100 nm. Figure 4(A) illustrates the topographic structure of sputtered HOPG which contains "hill-" and "pit-" like features. Close examination of these features indicates that many of the edges of the structures appear to be aligned crystallographically, consistent with the supposition that the anisotropy of the graphite structure will affect the mechanism of damage. The approximated edge site density estimated from the sputtered surface is two orders of magnitude larger than that of the cleaved surface. The differences in structure between the cleaved and sputtered surfaces may be quantitatively compared in the profiles of Figs. 4(B) and (C). Figure 4(B) was extracted from Fig. 4(A) at the position indicated by the arrows, and Fig. 4(C) was taken from a topographic image of cleaved graphite. Note that over similar lateral scales the cleaved graphite varies 70 nm in height, while the sputtered surface varies 800 nm.

The observed increase in the number of edge sites is consistent with the increase in surface reactivity, in that intensities in the spectra from the plasma-etched surface were lower than those of the sputtered surface. Furthermore, it seems that the mere presence of defects is not sufficient to cause reactions under the conditions examined here. Specifically, in the case of sputtering with argon, followed by dosing with molecular oxygen, the reactivity of the graphite was not increased. The suggestion that sputtering may have changed the carbon bonding to the extent than an amorphous structure results is not viable for two reasons. The TPD spectra for CO exhibit two distinct peaks, which implies that distinct sites were created rather than a continuum of defects characteristic of amorphous structure. Furthermore, the sharp nature of the features evident in the STM line profiles suggests that the defects consist of edges and steps. Further studies must be done to determine the exact nature of the defect bond configurations.

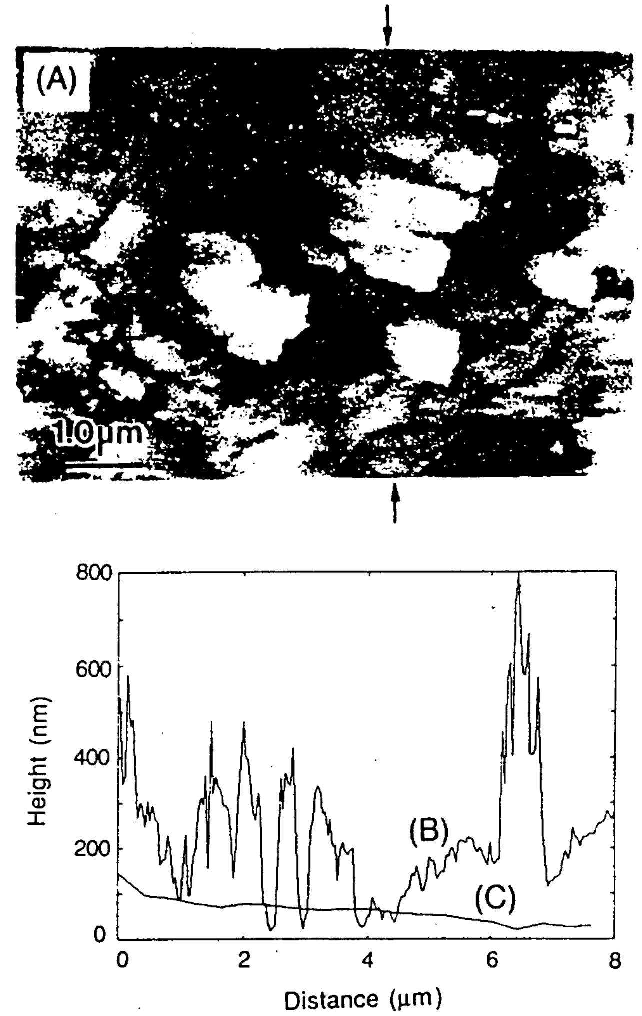

Fig. 4. (A) STM 6 mm × 8 mm constant-current topographical image of graphite after sputtering and heating to 1250 K, with full range of gray scale on the order of hundreds of nanometers. (B) Line profile extracted from (A) at the position indicated by the arrow. (C) Line profile extracted from a topographic image of cleaved graphite.

IV. Conclusions

In the summary, this study has found that surface treatment of HOPG by either an energetic oxygen ion beam or an oxygen ion plasma results in similar surface oxidation products. These data provide direct spectroscopic evidence for the presence of semi-quinone functionalities on oxidized HOPG. Unsurprisingly, the effect of sputtering on surface topography was much larger than that of plasma etching, as determined by HREELS. The effect of sputtering with oxygen ions on relative defect density was quantified by STM. The STM results imply that sputtering with oxygen ions causes the formation of steps and edges on cleaved graphite as opposed to amorphization of the surface. Finally, the physical disruption of the surface by sputtering does not lead to oxidation (under the thermochemical conditions examined here) in the absence of oxygen ions.

Acknowledgment: The authors are grateful to C. Warner for assistance with the large-scan STM analyses.

References

[1] J. R. Strife and J. E. Sheehan, "Ceramic Coatings for Carbon–Carbon Composites," *Am. Ceram. Soc. Bull.*, **67** [2] 369–74 (1988).

[2] D. P. Stinton, T. M. Besmann, and R. A. Lowden, "Advanced Ceramics by Chemical Vapor Deposition Techniques," *Am. Ceram. Soc. Bull.*, **67** [2] 350–55 (1988).

[3] D. W. McKee, "Oxidation Behavior and Protection of Carbon/Carbon Composites," *Carbon*, **25** [4] 551–57 (1987).

[4] P. Ehrburger, P. Baranne, and J. Lahaye, "Inhibition of the Oxidation of Carbon–Carbon Composite by Boron Oxide," *Carbon*, **24** [4] 495–99 (1986).

[5] D. W. McKee, "Borate Treatment of Carbon Fibers and Carbon/Carbon Composites for Improved Oxidation Resistance," *Carbon*, **24** [6] 737–41 (1986).

[6] E. J. Hippo, N. Murdie, and A. Hyjazie, "The Role of Active Sites in the Inhibition of Gas–Carbon Reactions," *Carbon*, **27** [5] 689–95 (1989).

[7] B. Marchon, J. Carrazza, H. Heinemann, and G. A. Somorjai, "TPD and XPS Studies of O_2, CO_2, and H_2O Adsorption on Clean Polycrystalline Graphite," *Carbon*, **26** [4] 507–14 (1988).

[8] B. Marchon, W. T. Tysoe, J. Carrazza, H. Heinemann, and G. A. Somorjai, "Reactive and Kinetic Properties of Carbon Monoxide and Carbon Dioxide on a Graphite Surface," *J. Phys. Chem.*, **92** [20] 5744–49 (1988).

[9] S. R. Kelemen and H. Freund, "O_2 Oxidation Studies of the Edge Surface of Graphite," *Carbon*, **23** [6] 619–25 (1985).

[10] F. Atamny, R. Schlögl, W. J. Wirth, and J. Stephan, "Topochemistry of Graphite Oxidation," *Ultramicroscopy*, **42–44**, 660–67 (1992).

[11] G. R. Hennig; pp. 32–33 in *Chemistry and Physics of Carbon*, Vol. 2. Edited by P. L. Walker, Jr. Marcel Dekker, New York, 1970.

[12] C. Sellitti, J. L. Koenig, and H. Ishida, "Surface Characterization of Graphitized Carbon Fibers by Attenuated Total Reflection Fourier Transform Infrared Spectroscopy," *Carbon*, **28** [1] 221–28 (1990).

[13] T. Takahagi and A. Ishitani, "XPS Studies by Use of the Digital Difference Spectrum Technique of Functional Groups on the Surface of Carbon Fiber," *Carbon*, **22** [1] 43–46 (1984).

[14] Y. Nakayama, F. Soeda, and A. Ishitani, "XPS Study of the Carbon Fiber Matrix Interface," *Carbon*, **28** [1] 21–26 (1990).

[15] A. Ishitani, "Application of X-ray Photoelectron Spectroscopy to Surface Analysis of Carbon Fiber," *Carbon*, **19** [4] 269–75 (1981).

[16] R. J. Purtell and M. Pomerantz, "Electron Energy Loss Spectroscopy of Real Surfaces," *Langmuir*, **7** [11] 2443–449 (1991).

[17] R. E. Palmer, J. F. Annett, and R. F. Willis, "Loss Structure in the Electron-Energy-Loss Excitation Continuum of a Semimetal," *Phys. Rev. Lett.*, **58** [23] 2490–93 (1987).

[18] "Layered Compounds"; pp. 1052–92 in *Microelectronics and Nanometer Structures*, Proceedings of the Fifth International Conference on Scanning Tunneling Microscopy/Spectroscopy and the First International Conference on Nanometer Scale Science and Technology, *J. Vac. Sci. Technol.*, **B9** [2] (1991) Part II.

[19] S. Park and C. F. Quate, "Tunneling Microscopy of Graphite in Air," *Appl. Phys. Lett.*, **48** [2] 112–14 (1986).

[20] H. Chang and A. J. Bard, "Formation of Monolayer Pits of Controlled Nanometer Size on Highly Oriented Pyrolytic Graphite by Gasification Reactions as Studied by Scanning Tunneling Microscopy," *J. Am. Chem. Soc.*, **112** [11] 4598–99 (1990).

[21] C. N. R. Rao, "Oxygenated Compounds: Carbonyl Compounds"; pp. 192–236 in *Chemical Applications of Infrared Spectroscopy*. Academic Press, New York, 1963.

[22] C. P. Warner and D. A. Bonnell, "Characterization of Plasticity on Bimaterial Interface Fracture by STM"; pp. 393–98 in *Structure and Properties of Interfaces in Materials*, Materials Research Society Symposium Proceedings, Boston, MA, December 2–5, 1991. Edited by W. A. T. Clark, U. Dahmen, and C. L. Briant. Materials Research Society, Pittsburgh, PA, 1992.

[23] M. J. Nowakowski, J. M. Vohs, and D. A. Bonnell, "Surface Reactivity of Oxygen on Cleaved and Sputtered Graphite," *Surf. Sci.*, **271** [3] L351–L356 (1992). □

Initial stages of SiO_x deposition on graphite

M. M. Hoveland
Department of Materials Science, University of Pennsylvania, Philadelphia, Pennsylvania 19104-6272

J. B. Danner and J. M. Vohs
Department of Chemical Engineering, University of Pennsylvania, Philadelphia, Pennsylvania 19104-6272

D. A. Bonnell
Department of Materials Science, University of Pennsylvania, Philadelphia, Pennsylvania 19104-6272

(Received 2 July 1993; accepted 16 December 1993)

The reaction of tetraethoxysilane (TEOS) and the subsequent deposition of SiO_x on the basal plane and edges of highly oriented pyrolytic graphite (HOPG) were studied. Interfacial bonding and surface morphologies resulting from different reaction conditions were probed using scanning tunneling microscopy (STM), Auger electron spectroscopy (AES), Rutherford backscattering spectroscopy (RBS), temperature programmed desorption (TPD), and high resolution electron energy loss spectroscopy (HREELS). The initial reaction of TEOS was found to occur at surface defects. STM images indicated that SiO_x films do not grow layer-by-layer, confirming earlier indirect observations to that effect.

I. INTRODUCTION

Although carbon has been successfully used in a number of structural applications, its potential as a structural material has not yet been fully realized. This is particularly true in high temperature applications where oxidation is often the limiting factor, in spite of the use of rather sophisticated protection strategies. The fundamental issues involved with oxidation protection of carbon have been reviewed by Buckley,[1] and Strife and Sheehan.[2,3] Regardless of whether oxidation protection involves diffusion barriers, chemical inhibition, or a combination of the two, atomic bonding in the coating and at the carbon interface dictates its efficacy.

There are numerous reports in the literature on various aspects of the use of coatings to inhibit the oxidation of carbon and its composites. The effectiveness of carbides, nitrides, silicides, and noble metals as oxygen diffusion barriers has been well documented.[2–6] The optimum choice of a coating material for a particular application depends on its vapor pressure, melting point, oxygen permeability, and coefficient of thermal expansion. Borate-based glass formers are used at temperatures below 1500 °C, while silicon-based systems (Si_3N_4 and SiC) are limited to 1800 °C. For applications above 1800 °C refractory oxides and titanates have been investigated and found to be appropriate for short time, single-cycle applications. Phosphates, borates, and chlorides are thought to be chemical inhibitors which poison reactive sites by bonding to undercoordinated carbon atoms.[2,5,7,8] In order to accommodate thermal expansion mismatch, strategies for oxidation protection above 1800 °C usually include layers of several compounds, for example, refractory oxide/silicate glass/refractory oxide/carbide.

Optimization of current methods and development of new approaches of oxidation inhibition require a systematic understanding of reactions of carbon with potential coating materials. The reactions of oxides, nitrides, and carbides with carbon, which dictate both film growth characteristics and the potential for chemical inhibition, are not understood at an atomic level. Previous work using photoelectron spectroscopy gives an indication of the variability of carbon bonding configurations and associated reactant functionalities.[9–11] Unfortunately, fibers and particles contain a high density of various defect types and most analytical techniques average over large areas, thus rendering atomic level interpretations somewhat difficult. In order to contribute to the fundamental understanding of these reactions, this study focuses on atomic interactions between graphite surfaces and a deposited silica film with the goal of elucidating how SiO_x interacts with the graphitic basal plane, planar edges, dislocations, vacancies, and steps. The model system consists of highly ordered pyrolytic graphite (HOPG) on which an SiO_x layer was grown via chemical vapor deposition using tetraethoxysilane (TEOS) as the reactant. The pyrolysis of TEOS on carbon, silica, and silicon has been studied previously, providing the basis for these high resolution studies.[12,13] The morphology and bonding during the initial stages of film deposition were characterized using STM, Auger electron spectroscopy (AES), Rutherford backscattering spectroscopy (RBS), temperature programmed desorption (TPD), and high resolution electron energy loss spectroscopy (HREELS).

II. EXPERIMENTAL PROCEDURES

Two vacuum analysis systems were used during deposition and characterization of silica on the HOPG substrates. Low pressure experiments were performed in an ultrahigh vacuum chamber with a base pressure of 2×10^{-10} Torr. The chamber was equipped with a quadrupole mass spectrometer (UTI 100C), optics for AES (Omicron), a high resolution electron energy loss spectrometer (McAllister), and an ion gun (Physical Electronics). The HOPG samples could be heated to temperatures in excess of 1000 °C and cooled to −180 °C via conduction from a resistively heated sample holder. Temperatures were monitored using a chromel/alumel thermocouple attached to the back face of the sample with a high temperature ceramic adhesive (Aremco 516). Higher pressure deposition experiments were performed in a second vacuum system which had a base pressure of 10^{-8} Torr. This chamber was equipped with a quadrupole mass spectrometer (Amtek) and heating capabilities similar to those described above.

Temperature programmed desorption (TPD) experiments were performed using a heating rate of 5 °C/s. HREELS spectra were collected using a 3.5 eV electron beam directed 60° from the surface normal with detection in the specular direction. The sample temperature was held at −180 °C during HREELS analysis. To characterize surface intermediates formed at higher temperatures, the sample was heated to the temperature of interest and then rapidly quenched to −180 °C, at which point the HREEL spectrum was collected. Sputter depth profile analysis was carried out *ex situ* using a Physical Electronics 600 AES. This instrument has a spatial resolution of approximately 2000 Å and is more sensitive in the region of the LMM silicon transition (at 92 eV) than is the *in situ* system. Rutherford backscattering was also used to characterize surface composition. The RBS system used a 3.15 MeV He^{+2} beam generated by a 5SDH-1 NEC Tandem Accelerator. The background pressure in the RBS scattering chamber was 4×10^{-7} Torr.

Two STM's were used for topographic analysis. One microscope contained a lever sample-tip approach system with a tube scanner. This system was capable of atomic resolution and was used for high resolution scans. The second system had an orthogonal stack piezo scanner with an inchworm type sample-tip approach. Large areas were imaged using this instrument which had a 50 μm lateral range and a 15 μm vertical range, with respective resolutions of 100 Å and 10 Å. All images were acquired in air at a constant current of 3 nA and a sample bias of 0.3 V.

HOPG substrates were cleaved in air to expose the basal plane. Edge planes were obtained by polishing a piece of HOPG perpendicular to the basal plane. Once in the vacuum chamber, the HOPG samples were annealed at 1000 °C. This produced a clean surface as determined by AES. Electronic grade TEOS (Aldrich) was contained in a glass sample vial and purified by freeze-pump-thaw cycles and vacuum distillation prior to use. TEOS was admitted into each vacuum chamber via a variable leak valve.

Two processes were used to deposit silica. The first, carried out in the high vacuum system, involved heating the HOPG substrate to reaction temperature and then exposing it to a constant pressure of TEOS. Subsequent to silica deposition, *ex situ* analyses were performed. In the UHV system silica was deposited during the course of TPD and HREELS experiments.

III. RESULTS AND DISCUSSION

A. Interfacial bonding

TPD was initially used to investigate the reaction of TEOS on the HOPG basal plane. The clean HOPG substrate was dosed with 6 L of TEOS at −180 °C and the sample was then heated at 5 °C/s while monitoring desorbing species with a mass spectrometer. The TPD spectra showed that molecular TEOS desorbed from the surface in a peak centered at −80 °C, while chemisorbed species remained intact to 225 °C where they reacted to produce gaseous ethanol and ethylene. Following the initial TPD experiment, AES analysis indicated the presence of a small amount of SiO$_x$ on the surface. In subsequent TPD experiments only the low-temperature molecular TEOS desorption state was observed and no significant increase in the amount of SiO$_x$ on the surface was detected. These results demonstrate that the sites that are most active for TEOS reaction were passivated during the first TPD cycle.

HREEL spectroscopy was used to examine the nucleation of the SiO$_x$ layer on the HOPG basal plane. HREEL spectra were collected as a function of sample temperature following exposure of the substrate to 6 L of TEOS at −180 °C. These spectra are displayed in Fig. 1 along with the spectrum of clean HOPG. The sloping baseline in the spectrum of clean surface has been reported previously and attributed to the excitation of electron-hole pairs in the substrate.[14] Peaks are evident in the spectrum of the TEOS-dosed surface at 487, 809, 975, 1108, 1435, 2230, and 2970 cm^{-1}. By comparison to previously reported HREEL spectra of TEOS-dosed surfaces, these peaks can be assigned to the δ(Si–O), ν(Si–O), ν(C–C), ν(C–O), $\delta(CH_3)$, ν(C–O) first overtone, and ν(C–H) modes, respectively.[13] The positions

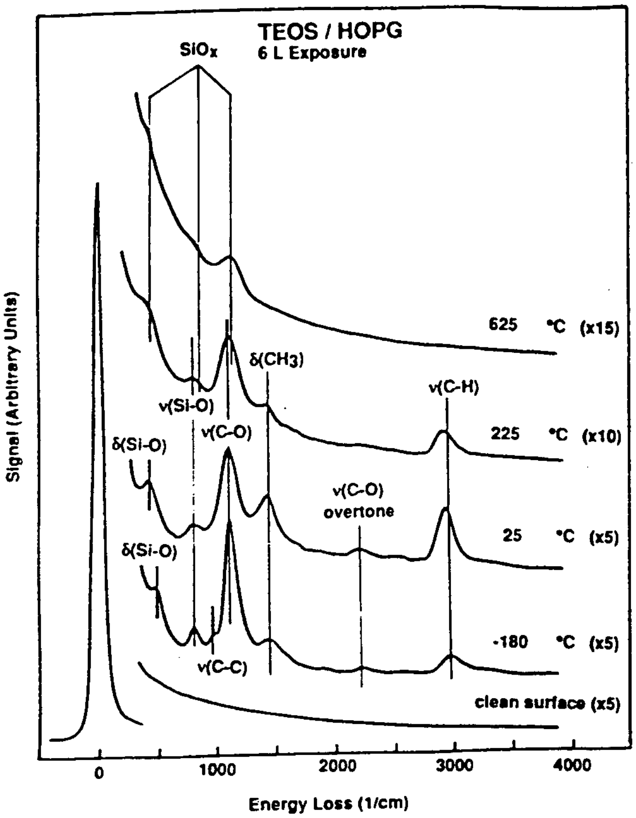

FIG. 1. HREELS spectra of the clean HOPG basal surface, the basal surface following a 6 L exposure of TEOS at −180 °C, and following subsequent heating to 25 °C, 225 °C, and 625 °C.

and relative intensities of the peaks are consistent with the presence of multilayers of molecular TEOS on the surface. Heating the TEOS-dosed surface to 25 °C to ensure that only chemisorbed species remained produced several changes in the HREEL spectrum. These include shifts in the positions of the δ(Si–O) and ν(Si–O) modes to 421 and 800 cm^{-1}, respectively, an increase in the intensity of the ν(C–H) mode, and a shift in its position to 2930 cm^{-1}. The ν(C–C) mode was no longer resolvable after heating to 25 °C. Due to the limited resolution of the spectrum, the exact structure of the adsorbed species at this temperature cannot be determined; however, the changes in peak positions and relative intensities indicate that either the configuration of the adsorbed TEOS is distorted from that of the free molecule or it has dissociated. Dissociation would most likely result in the formation of adsorbed ethoxy [$CH_3CH_2O^-$] and ethoxysilane species [$Si\text{-}(OCH_2CH_3)_n$, $n = 1..3$].

Heating the TEOS-dosed sample to 225 °C resulted in a marked decrease in the intensities of all of the peaks in the HREEL spectrum. This is consistent with the TPD results which showed that adsorbed TEOS decomposes near this temperature to produce gaseous ethylene and ethanol. The presence of a small δ(CH_3) peak in the spectrum centered at 1430 cm^{-1} demonstrates that decomposition of the adsorbed species is not complete and that some ethoxy groups remain on the surface. In addition to the decrease in peak intensities, several other changes occurred upon heating to 225 °C. These include the disappearance of the δ(Si–O) mode at 421 cm^{-1} and the appearance of a new peak at 400 cm^{-1}, and a shift in the position of the ν(C–O) mode from 1108 to 1120 cm^{-1}. These changes can be attributed to decomposition of a portion of the ethoxy ligands and the formation of Si–O–Si siloxane linkages. The HREEL spectrum of molecules containing siloxane bridges generally contain three normal modes centered at approximately 400, 800, and 1120 cm^{-1}.[15] Thus, the peak at 400 cm^{-1} may result from excitation of one of these siloxane normal modes. The large peak at 1120 cm^{-1} most likely contains contributions from both the Si–O–Si mode and the ν(C–O) mode of the remaining ethoxy ligands. The spectrum obtained after heating to 625 °C contains three peaks centered 424, 820, and 1120 cm^{-1}, which can be assigned to the normal modes of SiO_x.

Following the HREELS experiments an attempt was made to grow a thick SiO_x film. In this experiment the same HOPG sample used in the HREELS study was heated to 425 °C and then exposed to 1×10^{-6} Torr of TEOS. *In situ* AES indicated that a TEOS exposure time of 45 min produced only a marginal increase in the amount of deposited SiO_x. In order to characterize compositional variations at the interface, RBS and AES sputter depth profile analyses of this sample were performed. The RBS spectrum is displayed in Fig. 2. The small peaks centered at 1.20 and 0.85 MeV correspond to scattering from silicon and oxygen atoms in the deposited silica layer, while the edge at 0.62 MeV corresponds to scattering from the graphite substrate. The fact that silicon and oxygen exhibit distinct peaks indicates that they are surface species and that the silica layer is less than 300 Å in thickness. The position of the carbon edge, 0.62 MeV, is that expected for a clean carbon surface and therefore demonstrates that the silica layer does not completely cover the surface. The ratio of silicon to oxygen is estimated from these data to be 1 : 3.5, somewhat higher than that expected for SiO_2. This result suggests that portions of exposed carbon must be partially oxidized. This could have occurred when the sample was exposed to air during transfer from the HREELS chamber to the RBS analysis system.

An AES sputter depth profile of this sample was also collected. The Auger spectra contained peaks centered at 76, 92, 272, and 510 eV. These peaks can be assigned to silicon bonded to oxygen (Si_O), silicon bonded to carbon (Si_C), carbon, and oxygen, respectively. Figure 3 displays the relative concentrations Si_O, Si_C, O, and C as a function of sputter time. The relative concentrations

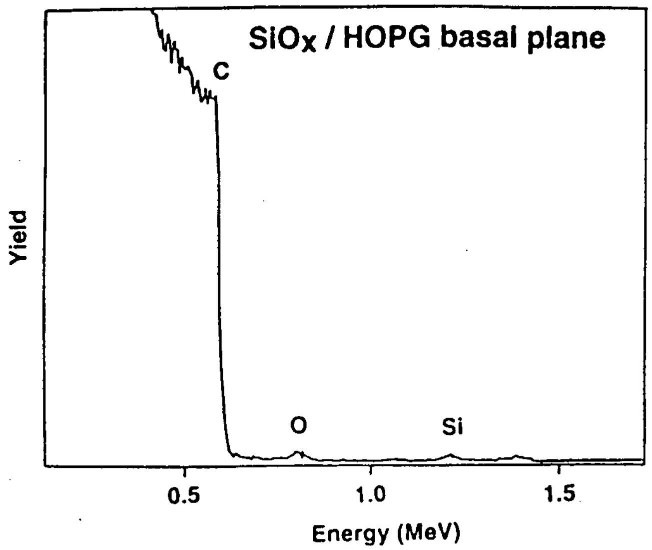

FIG. 2. RBS spectrum of SiO$_x$ deposited on the basal plane of HOPG.

of Si$_O$ and oxygen decrease with sputter time (i.e., depth). That of Si$_C$ initially increases with depth, then goes through a maximum, and then decreases. The AES results suggest that the surface of the deposited layer consists of SiO$_2$, while the interfacial region consists of silicon carbide. Thus, bonding at the interface occurs primarily through Si–C bonds. It should be noted that since a significant C signal was detected prior to sputtering, it is likely that a portion of the surface was not covered by the SiO$_x$ layer. This conclusion is consistent with the RBS results.

It is useful to compare the sputter depth profile results obtained from SiO$_x$ layers on the basal plane with those obtained for SiO$_x$ layers on planar edges. Figure 4 displays a depth profile obtained from a sample that was exposed to 10^{-3} Torr of TEOS at 600 °C for 75 min (the reaction was carried out in the high vacuum chamber). The trends in the relative concentration of Si$_O$, Si$_C$, O, and C are qualitatively similar to those for deposition on the basal plane; however, the fact that the surface carbon concentration is significantly higher than that on the basal plane suggests that deposition occurs more inhomogeneously on the edge surface than on the basal surface.

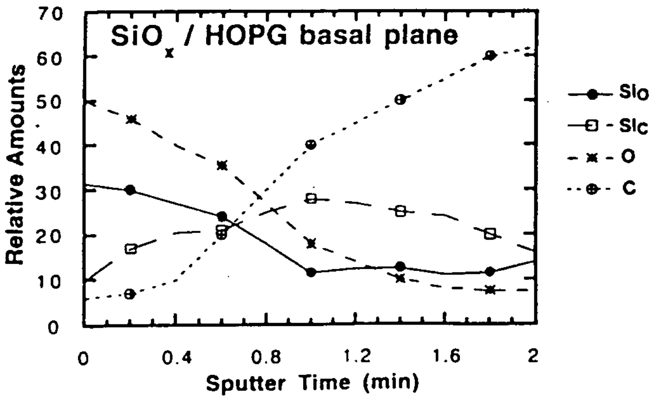

FIG. 3. AES depth profile analysis of SiO$_x$ deposited on the basal plane of HOPG.

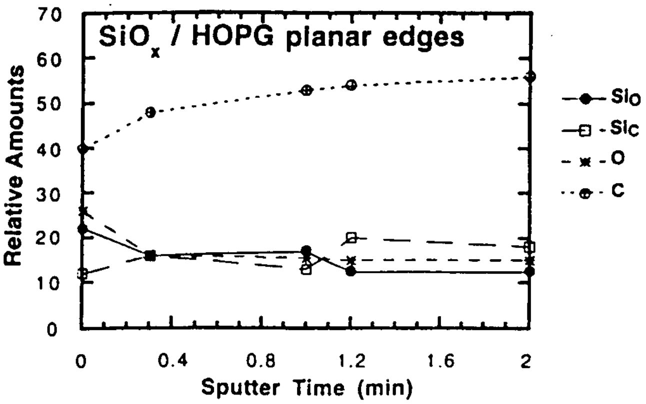

FIG. 4. AES depth profile analysis of SiO$_x$ deposited on the planar edges of HOPG.

B. Film topography

STM was used to characterize the topographies of films deposited on the basal plane. Figures 5 and 6 display both large and small scale constant current images of samples on which silica has been deposited. The sample in Fig. 5 is the same as that used in the TPD and HREELS experiments and was exposed to 10^{-6} Torr of TEOS at 425 °C for 45 min. Figure 5(a) shows that the morphology of the sample exposed to TEOS at 10^{-6} Torr contains inhomogeneously distributed island-like features which are 0.1–0.8 μm in diameter. The separation between these features ranges from 0.2 to 2 μm. A higher resolution image of a flat region of this surface is shown in Fig. 5(b) and reveals homogeneously distributed features on the order of several nms in lateral and vertical dimension. The sample whose STM image is displayed in Fig. 6 was prepared by exposing a basal plane to 10^{-3} Torr of TEOS at 600 °C for 120 min. The image in Fig. 6(a) shows island-like features which vary in diameter from 1 to 8 μm and have heights in the range 0.2–0.4 μm. On average, the islands are separated by approximately 3 μm. A higher resolution image of a region between the large islands [Fig. 6(b)] reveals the presence of smaller island-like features that are inhomogeneously distributed. Figure 7 displays a low resolution image of the same sample. In this image the islands appear to be aligned with crystallographic precision, and changes in the character of the topography occur abruptly, suggesting that the islands are aligned along step edges.

On both samples which were studied using STM, the tunneling current was less stable over regions with high densities of large islands than over those appearing

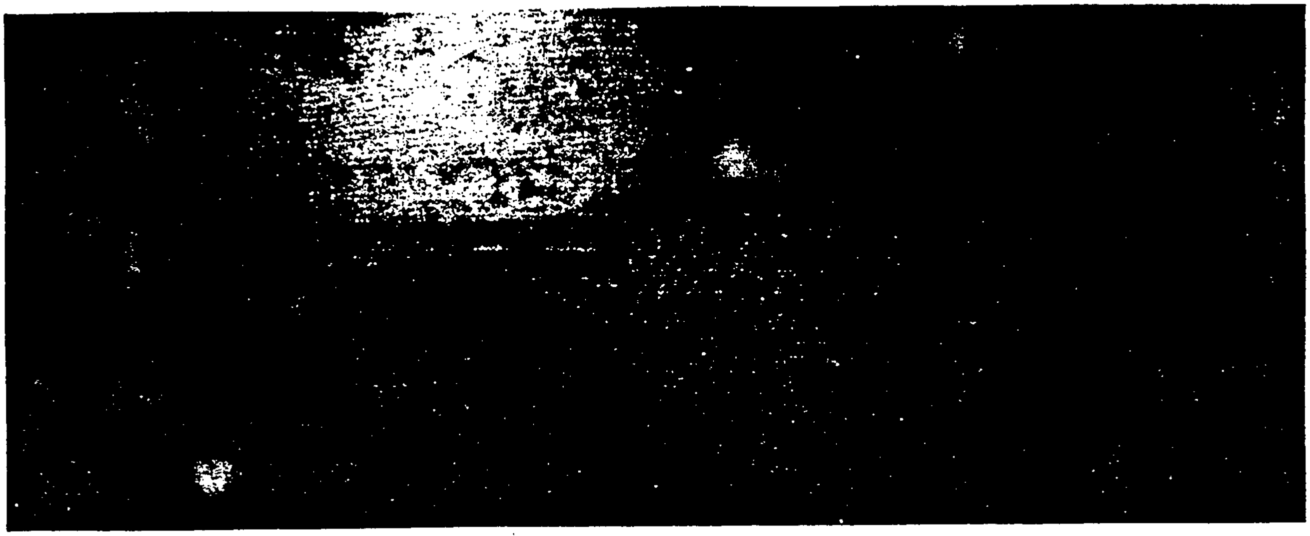

(a)

(b)

FIG. 5. Constant current STM image of SiO_x deposited on basal plane graphite under low pressure short exposure: (a) 7.2 μm × 20 μm, vertical scale 1 μm; (b) 150 nm × 150 nm area, vertical scale 10 nm, current 1 nA, and bias 10 mV.

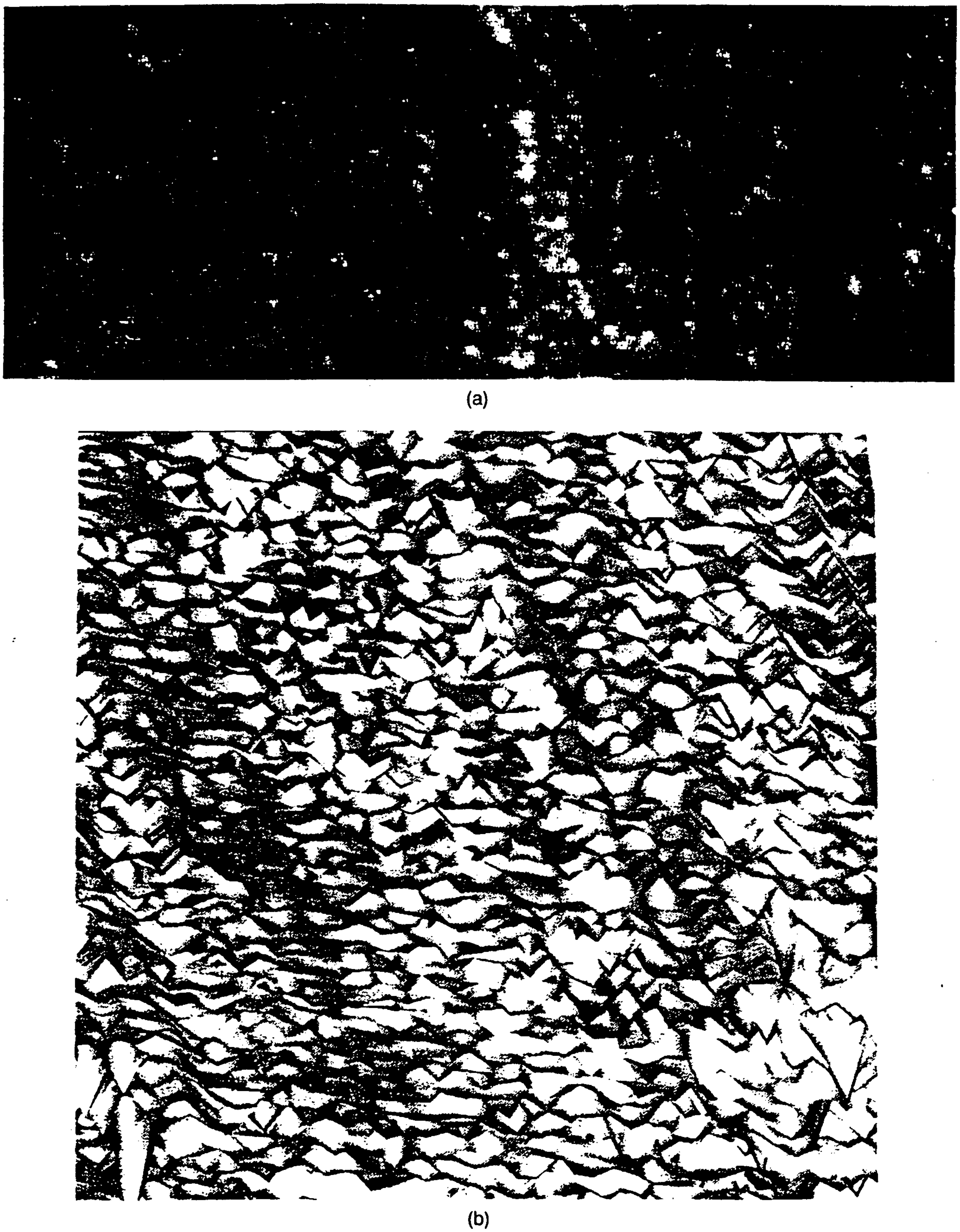

FIG. 6. Constant current STM image of SiO$_x$ deposited on basal plane graphite under high pressure long exposure conditions: (a) 7.2 μm × 20 μm area with 5 μm vertical scale; (b) 150 nm × 150 nm area, 19 nm vertical scale, current 1 nA, and bias 50 mV.

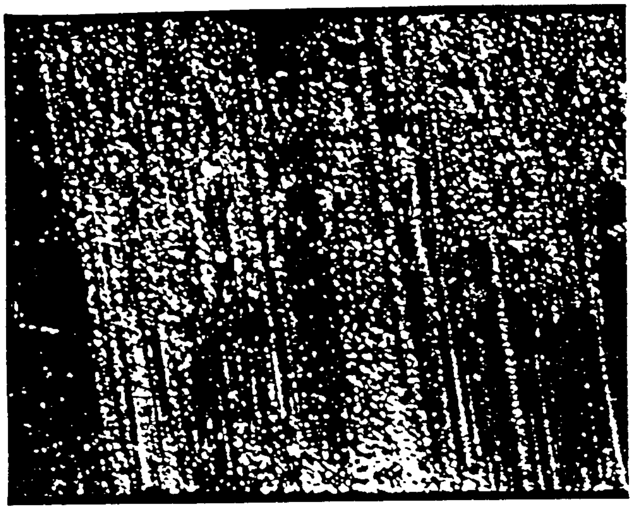

FIG. 7. Constant current STM image of 20 μm × 20 μm area, vertical scale 3 μm, current 1 nA, and bias 50 mV.

flatter, i.e., regions such as those shown in Figs. 5(b) and 6(b). This result indicates that the large islands exhibit low conductivity.

IV. SUMMARY

The TPD and HREELS results clearly demonstrate that TEOS adsorbs dissociatively on the basal plane of HOPG to form stable ethoxysilane species. These species decompose at 225 °C to produce gaseous ethylene and ethanol and deposit SiO$_x$ on the surface. AES depth profiles show that the deposited SiO$_x$ layer is bonded to the surface through Si–C linkages. Both RBS and STM results demonstrate that the growth of the silica layer does not occur by a layer-by-layer process. Rather, the silica nucleates and forms islands. This conclusion is also consistent with the TPD results. Reaction of TEOS and deposition of silica were found to occur readily during the first TPD experiment on a freshly cleaved basal plane, while the extent of silica deposition remained largely unchanged following subsequent TPD experiments. Indeed, attempts to grow thick SiO$_x$ layers in the UHV analysis system were unsuccessful. Taken together, the TPD and STM data indicate that the active sites for TEOS decomposition are surface defects which are located at step edges. The initial reaction at these defects is facile; however, once the active sites have been passivated, growth of the SiO$_2$ overlayer occurs much more slowly.

It has been previously reported that the active sites for TEOS decomposition on graphite are the same as those for oxidation of graphite with molecular oxygen.[12] Since the results of this study demonstrate that a small amount of TEOS-deposited SiO$_2$ passivates these active sites, this treatment may provide some degree of oxidation inhibition even though the entire graphite surface is not encapsulated in SiO$_2$.

ACKNOWLEDGMENTS

This work was supported by the Air Force Office of Scientific Research under Grant No. AFOSR-91-0103. Additionally, facilities used in this work were supported by the National Science Foundation, Materials Research Laboratory Program, under Grant No. DMR91-20668 (the Ion Scattering Facility and Materials Processing Facility). We are grateful to M. Nowakowski, D. Carroll, and D. Jiron for helpful discussions regarding carbon oxidation and for assistance in preparing the manuscript.

REFERENCES

1. J. D. Buckley, Ceram. Bull. **67**, 364 (1988).
2. J. R. Strife and J. E. Sheehan, Ceram. Bull. **67**, 369 (1988).
3. D. W. McKee, Carbon **25**, 551 (1987).
4. J. E. Sheehan, Carbon **27**, 709 (1989).
5. K. L. Luthra, Carbon **26**, 217 (1988).
6. A. A. Cochran, J. B. Stephenson, and J. G. Donaldson, J. Metals **37**, August, 37 (1970).
7. D. W. McKee, C. L. Spiro, and E. J. Lamby, Carbon **22**, 507 (1984).
8. E. J. Hippo, N. Murdie, and A. Hyjazie, Carbon **27**, 689 (1989).
9. C. Kozlowski and P. Sherwood, Carbon **25**, 751 (1987).
10. C. Kozlowski and P. Sherwood, J. Chem. Soc., Faraday Trans. 1 **81**, 2745 (1985).
11. C. Kozlowski, and P. Sherwood, Carbon **24**, 357 (1986).
12. W. P. Hoffman and P. Ehrburger, J. Anal. Appl. Pyrolysis **15**, 275 (1989).
13. J. B. Danner, M. A. Rueter, and J. M. Vohs, Langmuir **9**, 455 (1993).
14. R. E. Palmer, J. F. Annett, and R. F. Willis, Phys. Rev. Lett. **58**, 2490 (1987).
15. P. A. Thiry, M. Liehr, J. J. Pireaux, P. Sporken, R. Caudano, J. Pl. Vigeron, and A. A. Lucas, J. Vac. Sci. Technol. B **3**, 1118 (1985).

Surface Science Letters 271 (1992) L351-L356
North-Holland

surface science
letters

Surface Science Letters

Surface reactivity of oxygen on cleaved and sputtered graphite

M.J. Nowakowski [a], J.M. Vohs [b] and D.A. Bonnell [a]

[a] *Department of Materials Science and Engineering, University of Pennsylvania, Philadelphia, PA 19104, USA*
[b] *Department of Chemical Engineering, University of Pennsylvania, Philadelphia, PA 19104, USA*

Received 4 February 1992; accepted for publication 24 February 1992

The characterization of reactions which occur during the oxidation of highly oriented pyrolytic graphite (HOPG) was performed using high-resolution electron energy loss spectroscopy (HREELS), temperature programmed desorption (TPD), and scanning tunneling microscopy (STM). The results of this investigation provide spectroscopic evidence for the presence of semi-quinone functionalities on sputtered and oxidized HOPG. STM images are presented to quantify the increase in defect sites after oxygen ion sputtering, and to correlate defect site density with reactivity.

1. Introduction

Recently developed carbon-containing materials, such as carbon–carbon composites, have proven very useful for high temperature structural applications in the aerospace industry. Although they exhibit excellent high temperature mechanical properties, these materials have intrinsic limitations due to their chemical instability in oxidizing environments. Coating with ceramics to produce a diffusion barrier is one approach to oxidation protection that has been exploited with some success. In contrast to this physical mechanism of protection, it may also be possible to use chemical inhibition to control surface oxidation. In order to achieve this goal a detailed understanding of the mechanisms of carbon oxidation reactions will be required. In recent years there has been much effort directed towards investigating oxidation of different forms of carbon, including graphite, fibers, and composites. A variety of techniques have been used to characterize these oxidation processes including temperature programmed desorption (TPD), photoelectron spectroscopy (XPS and UPS), Auger electron spectroscopy (AES), X-ray diffraction (XRD), scanning electron microscopy (SEM), and more recently scanning tunneling microscopy (STM) [1–6]. Most of this work has focused on measuring the reaction kinetics of carbon oxidation, as opposed to the specific reaction mechanisms.

It is well established that the basal plane of graphite is relatively unreactive toward molecular oxygen, while step edges and defects in these planes may oxidize more readily [7]. It has been shown that the rate of oxidation at the edges of the basal planes is sensitive to the local structure of the edge site. It has also been suggested based on TPD results that both semi-quinone and lactone species exist on oxidized surfaces of graphitic particles [2]. Other authors have made similar assignments using Fourier transform infrared spectroscopy (FTIR) and XPS of graphite fibers [8–11].

In the present study we make use of high-resolution electron energy loss spectroscopy (HREELS) and STM to characterize the structure and composition of oxidized surfaces of highly oriented pyrolytic graphite (HOPG). In the case of HREELS, there have been relatively few studies in which this technique has been applied to carbon surfaces. One recent HREELS study compared the vibrational spectra of cleaved graphite with those of a sputtered surface [12]. Palmer et al. have also used HREELS in a study of the mechanisms of the electron scattering from graphite surfaces [13]. In the case of STM, the technique has proven important for direct observation of the topography of graphite. A large literature has accumulated on imaging graphite with STM [14,15], and atomic resolution imaging of graphite, albeit amidst controversy over interpretation, is now routine. Formation of monolayer pits upon oxidation of the basal plane of HOPG has been observed with STM, as has the anisotropy of oxidation rates of the pit edges [16]. Neither HREELS nor STM have been fully exploited in investigations of carbon oxidation reactions, nor has their combined use, in conjunction with conventional surface analytical methods, been directed to a systematic study of oxidation mechanisms.

The objective of the present study is to examine reactions of oxygen on cleaved and sputtered HOPG, and use direct spectroscopic evidence to identify oxygen surface species on the graphite samples. These measurements are compared to the species proposed as products of oxidation of graphitic particles. HREELS and TPD are used to determine surface functionalities and STM is used to characterize the topographic structure of the surfaces. Other conventional surface analytical tools, (TPD, AES, etc.) are also used. After a discussion of the experimental procedures, the HREELS results are compared to previous work on related surfaces and are discussed in terms of defect densities estimated by STM analysis.

2. Experimental procedure

Temperature programmed desorption and HREELS experiments were performed in a stainless steel ultrahigh vacuum chamber with a base pressure of 1×10^{-10} Torr. The system included a quadrupole mass spectrometer (UTI 100C), a high resolution electron energy loss spectrometer (McAllister) and a cold-cathode ion gun (VG Scientific). The HOPG sample was mounted in a tantalum foil sample holder which was spotwelded to the sample manipulator. The sample temperature was monitored using a chromel–alumel thermocouple which was attached to the back face of the sample using a ceramic adhesive. During TPD experiments the sample was heated at a rate of 8 K/s by conduction from the resistively heated sample holder. The HREEL spectra were obtained using a 3 meV electron beam incident at 60° from the sample normal with the scattered electrons collected in the specular direction.

The HOPG sample (1 cm^2) was initially cleaved in air and immediately inserted into the vacuum chamber. The sample was then heated to 1000 K to desorb any adsorbed species. Both HREELS and AES indicated that after heating the surface was clean. In order to oxidize the surface and create surface defects the sample was sputtered with an oxygen ion beam for 10 min (4 kV, 1 μA).

Following the HREELS and TPD studies, the sample was removed from the vacuum system and characterized in air using STM. Constant current images (1 nA) were obtained using a W tip with a −60 mV bias voltage. Two STMs were used to characterize the topographic structure of the cleaved and sputtered graphite. High resolution imaging was accomplished on a standard instrument (WA Technology) with mechanical tip approach and tube scanner. Large area analysis was accomplished on a long range STM with a lateral range of 80 μm, a vertical range of 10 μm, and spatial resolution of 1 nm. images were acquired at several locations in order to characterize the general morphology of the surface. The topographic structure of the sputtered surface was compared to the structure of a freshly cleaved graphite sample under the same conditions.

3. Results and discussion

The HREELS spectrum of the cleaved graphite surface following annealing at 1000 K is displayed in fig. 1A. The elastic peak intensity was found to be sharply peaked in the specular direction, indicating a relatively flat surface. Although no losses indicative of adsorbed species are present in the spectrum, the elastic peak does exhibit a broad tail that extends to high loss energies. This tail on the elastic peak has been observed in a previous HREELS study of graphite surfaces and has been attributed to excitation of electron–hole pairs

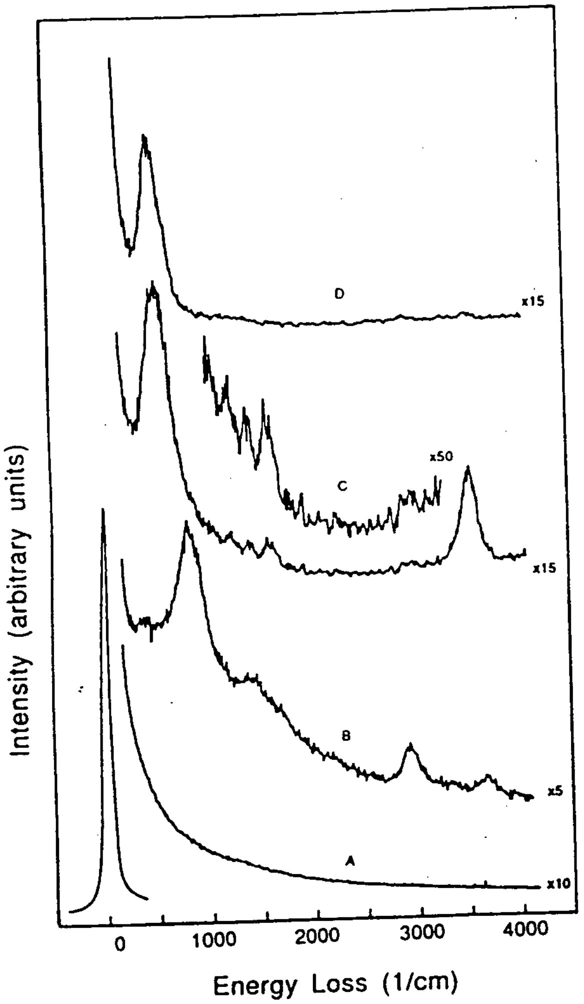

Fig. 1. (A) HREEL spectra of a cleaved graphite sample after heating to 1000 K, (B) after sputtering with oxygen, (C) after heating the sputtered sample to 1000 K, (D) after heating the sputtered sample to 1250 K.

[13]. For a semimetal, such as graphite, the density of states at the Fermi energy (E_F) is zero, but rises both above and below E_F. Excitation of vertical transitions from the valence band to the conduction band give rise to the energy loss continuum observed in the HREEL spectrum.

As expected, the cleaved graphite surface was found to be relatively unreactive toward O_2. Exposure of this surface to up to 6×10^5 L of O_2 at ambient temperature did not result in the formation of any oxygen containing surface complexes, as evidenced by the absence of any new features in the HREEL spectrum. In order to partially oxidize the surface the sample was sputtered with an oxygen ion beam. This sputtering process also served to increase the number of surface defects and steps. The composition of the oxygen ion beam was not determined; however, it was most likely composed of both doubly ionized O_2 molecules and singly ionized oxygen atoms. Following sputtering, the HREEL spectrum of the surface was again collected and found to be substantially different than that obtained from the cleaved surface. As shown in fig. 1B, the most noticeable change in the spectrum was the appearance of several prominent losses centered at 810, 1470, 2950, and 3650 cm^{-1}. The two highest energy peaks can be assigned to the C–H stretching mode of surface hydrocarbon species (2950 cm^{-1}) and the O–H stretching mode of adsorbed hydroxyl groups (3650 cm^{-1}) [17]. Since significant amounts of H_2O are present in the chamber background gas during sputtering, it is likely that these surface CH_x and OH species were formed by dissociative adsorption of water at surface defect sites. it is somewhat more difficult to assign the peaks at lower loss energies. It is possible that the peak centered at 1470 cm^{-1} is due to the C–H bending mode of the surface CH_x species. The origin of the large peak at 810 cm^{-1} will be discussed below. In addition to partially oxidizing the surface, the sputtering process also significantly increased the roughness of the surface. This was evident by a large decrease in the intensity of the elastic peak following sputtering.

After collection of the HREELS spectrum from the sputtered surface, the sample was heated to 1000 K while monitoring for desorbing species with the mass spectrometer. The primary desorption products detected were CO and CO_2; the TPD spectra for these molecules are displayed in figs. 2A and 2B. Carbon dioxide desorbed over a wide temperature range with a maximum occurring at 740 K. Carbon monoxide also desorbed over a wide temperature range with maxima occurring at 780 and 910 K. In addition to CO and CO_2, smaller amounts of H_2O and hydrocarbon species desorbed from the surface at temperatures between 300 and 500 K. It is interesting to

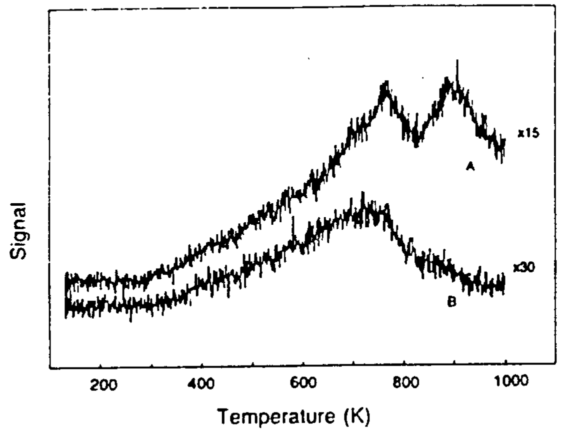

Fig. 2. (A) TPD spectra of mass 28 (CO) and (B) mass 44 (CO_2) after sputtering the sample with oxygen.

compare these TPD results with those obtained previously by Marchon and coworkers [1,2] for oxidized graphitic particles. These authors also observed CO and CO_2 as desorption products following the exposure of the particles to O_2. They found that the CO_2 desorption spectra were dependent on the O_2 dosing temperature. For room temperature exposure, CO_2 desorbed in two peaks centered at 433 and 693 K. increasing the O_2 dosing temperature generally resulted in an increase in the CO_2 desorption temperature; following O_2 exposure at 773 K, CO_2 desorbed in a single peak centered at 900 K. The CO desorption spectra were less dependent on the O_2 dosing temperature with CO desorbing in two peaks centered at 1093 and 1253 K with a shoulder at 973 K. Based primarily on desorption activation energies calculated from the TPD results, these authors proposed that the CO peaks resulted from decomposition of surface semi-quinone species and the CO_2 from decomposition of surface lactones.

Following the TPD experiment in which the sample was heated to 1000 K, the surface was again characterized using HREELS. As shown in fig. 1C, the resulting HREEL spectrum was significantly different from that obtained before heating. One of the most noticeable changes is the almost complete disappearance of the C–H stretch at 2950 cm^{-1}, indicating the desorption of nearly all the CH_x species from the surface. Other changes include the appearance of small peaks centered at 1200, 1390, and 1620 cm^{-1} and a shift in the position of the large peak previously at 810 cm^{-1} to 530 cm^{-1}. The O–H stretching mode near 3600 cm^{-1} was relatively unchanged upon heating, indicating the continued presence of OH groups on the surface. The peak at 1200 cm^{-1} is also most likely due to surface OH groups and and can be attributed to the C–OH stretching mode of these species. The peak at 1620 cm^{-1} is in a position characteristic of a C=O stretching mode. It is somewhat more difficult to assign the peak at 1390 cm^{-1}; however, the most reasonable assignment seems to be the O–H bending mode of the surface hydroxyl groups. These HREELS results indicate that the primary oxygen containing functional groups on the surface after heating to 1000 K are hydroxyls and carbonyls. The presence of carbonyl functionalities is consistent with the formation of surface semi-quinine species as has been previously proposed by Marchon et al. [2] for graphitic particles. Surface lactone species have also been proposed to exist on oxidized graphite and would be expected to give rise to a C=O stretching mode in the HREEL spectrum. The C=O stretching mode in lactones generally occurs between 1700 and 1800 cm^{-1} [17]. The lack of a peak in this region of the spectrum indicates that either surface lactones were not formed by the oxidation procedure used in this study or that they decompose at temperatures less than 1000 K. It is possible that the CO and CO_2 peaks observed in the TPD spectra result from lactone decomposition.

The sample was then heated to approximately 1250 K, and the resulting HREELS spectrum is shown in fig. 1D. As shown in the spectrum, none of the previous peaks related to oxygen containing species are observed, indicating the decomposition of the surface semi-quinone and C–OH species. These and the previous HREELS results provide direct spectroscopic evidence in support of the surface functionals described by Marchon et al. [1].

The only features in the HREEL spectra that have yet to be explained are the rather large peaks that appeared at low energy in the spectra of the sputtered surface. After sputtering, a peak appeared at 810 cm^{-1} and shifted to 530 cm^{-1} upon heating the sample to 1000 K. This peak was found to persist even after extended annealing at 1250 K, suggesting that it is not due to an oxygen containing species on the surface. One possibility is that these peaks are due to a skeletal vibration of a polyaromatic species on the surface. Such species could easily be formed during the sputtering process. If this were the case, however, one would expect to observe additional modes in the spectrum. Indeed, the appearance of only a single mode in the spectrum of the sputtered and annealed surface suggests that these peaks are not associated with a vibrational mode of a surface species. A more likely possibility is that the peaks resulted from excitation of low energy electronic transitions. The creation of defects and steps during sputtering undoubtedly alters the surface density of states near the Fermi level. It is therefore possible that the low energy peaks resulted from excitation of electron–hole pairs from low lying defect electronic states. A detailed analysis of the surface electronic properties will therefore be required before this peak can be definitively assigned.

The impact of sputtering on the surface morphology is indicated by the increased breadth and decreased intensity of the elastic HREELS peak which can be attributed to increased surface roughness. This change in roughness has been quantified using both high resolution and large scan STM imaging. The topographic structures of cleaved and sputtered HOPG graphite are compared in fig. 3. The grey scale representations are normalized to the largest feature in the image. Cleaved graphite typically contains surface steps with heights of integer multiples of the distance between basal planes (6.708 Å). In contrast, the features on the sputtered surface range in size from 10 to 100 nm. Fig. 3B illustrates the topographic structure of sputtered HOPG which contains "hill" and "pit" like features. Close examination of these features indicates that many of the edges of the structures appear to be aligned crystallographically, consistent with the supposition that the anisotropy of the graphite structure will affect the mechanism of damage. The approximated edge site density estimated from the sputtered surface is two orders of magnitude larger than that of the cleaved surface. The differences in structure between the cleaved and sputtered surfaces may be quantitatively compared in the profiles of fig. 4, which were extracted from the images at the positions indicated by the arrows. Note that over similar lateral scales

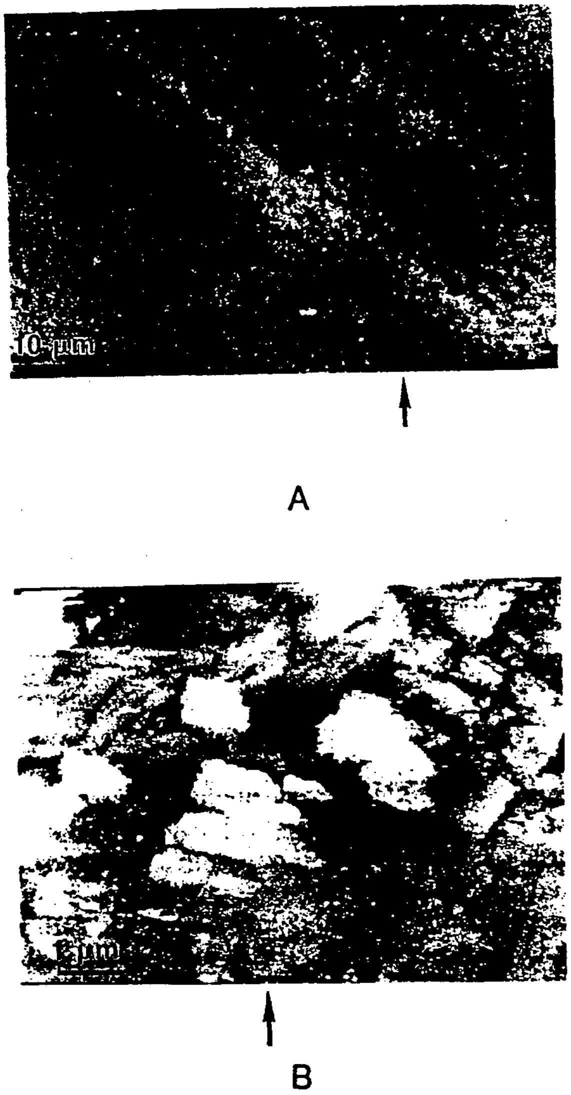

Fig. 3. (A) STM 50×70 μm constant current topographical image of freshly cleaved graphite, with full range of grey scale equivalent to 100 nm. (B) STM 6×8 μm constant current topographical image of graphite after sputtering and heating to 1250 K, with full range of grey scale equivalent to 800 nm.

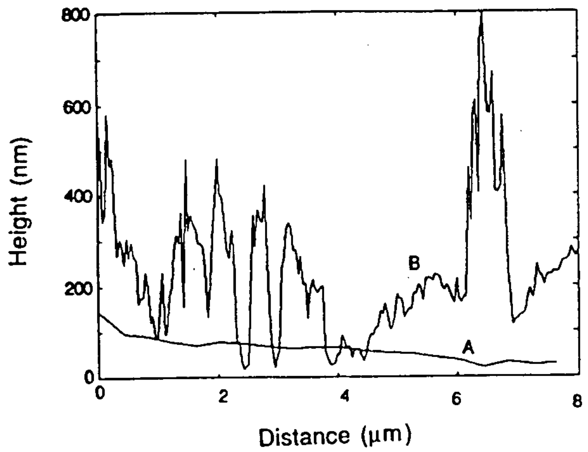

Fig. 4. (A) and (B) line profiles extracted from figs. 3A and 3B at positions indicated by arrows.

the cleaved graphite varies 70 nm in height, while the sputtered surface varies 800 nm.

The foregoing estimate of defect site density has implicitly assumed that the primary effect of sputtering is to increase the number of edge sites; not an entirely naive assumption given the extreme anisotropy in bond strengths of graphite. This rather crude approximation goes a long way in explaining the increased reactivity of the sputtered surface documented in this, and other, studies. Not included in this assumption is the possibility that sputtering may change the carbon bond configuration, i.e., the resulting surface disorder may be so extensive as to resemble amorphous carbon. If, however, the two peaks in the TPD spectrum are associated with in general two different defect site configurations, then sputtering did not totally disorder the surface. Furthermore, the sharp features on the sputtered graphite as seen in the line profile of fig. 4B indicate that the surface was not amorphized, but that the defects consist of edges and steps. The exact nature of defect bond configuration is left to further study.

5. Conclusions

In summary, this study has provided direct spectroscopic evidence for the presence of semiquinone functionalities on oxidized HOPG. The stability of the surface species was measured with TPD and HREELS. The effect of sputtering with low energy oxygen ions on surface topography and defect density was examined by HREELS and quantified by STM. The similarity of the TPD results obtained here with those obtained for oxidized graphitic particles implies that the bonding configurations of a sputtered surface are similar to the defect sites of the graphitic particles. The STM results suggest that sputtering of the cleaved graphite surface resulted in an increase in the density of steps and edges but did not cause total amorphisation of the surface.

Acknowledgements

The authors are grateful to C. Warner for assistance with the large scan STM analyses. This work was supported by the Air Force Office of Scientific Research, Division of Chemistry and Materials under grant #AFOSR-91-0103.

References

[1] B. Marchon, J. Carrazza, H. Heinemann and G.A. Somorjai, Carbon 26 (1988) 507.
[2] B. Marchon, W.T. Tysoe, J. Carrazza, H. Heinemann and G.A. Somorjai, J. Phys. Chem. 92 (1988) 5744.
[3] S.R. Kelemen and H. Freund, Carbon 23 (1985) 619.
[4] R. Schlogl, F. Atamny, W.J. Wirth and J. Stephan, to be published.
[5] D.W. McKee, Carbon 24 (1986) 737.
[6] E.J. Hippo, N. Murdie and A. Hyjazie, Carbon 27 (1989) 689.
[7] G.R. Hennig, in: Chemistry and Physics of Carbon, Vol. 2, Ed. P.L. Walker, Jr. (Dekker, New York, 1970).
[8] C. Sellitti, J.L. Koenig and H. Ishida, Carbon 28 (1990) 221.
[9] T. Takahagi and A. Ishitani, Carbon 22 (1984) 43.
[10] Y. Nakayama, F. Soeda and A. Ishitani, Carbon 28 (1990) 21.
[11] A. Ishitani, Carbon 19 (1981) 269.
[12] R.J. Purtell and M. Pomerantz, Langmuir 7 (1991) 2443.
[13] R.E. Palmer, J.F. Annett and R.F. Willis, Phys. Rev. Lett. 58 (1987) 2490.
[14] J. Vac. Sci. Technol. B 9 (1991) 1052.
[15] S. Park and C.F. Quate, Appl. Phys. Lett. 48 (1986) 112.
[16] H. Chang and A.J. Bard, J. Am. Chem. Soc. 112 (1990) 4598.
[17] C.N.R. Rao, Chemical Applications of Infrared Spectroscopy (Academic Press, New York, 1963).

CHARACTERIZ' G THE MICROSTRUCTURES OF Ti iB$_2$ NANOCOMPOSITES WITH ENERGY FILTERED TEM

V. SZABO[*], M. RÜHLE[*], M. NOWAKOWSKI[**], K. SU[†], L. SNEDDON[†] and D. BONNELL[**]
[*]Max-Planck-Institut für Metallforschung, Stuttgart, Germany
[**]Dept. of Materials Science, The University of Pennsylvania, Philadelphia, PA
[†]Dept. of Chemistry, The University of Pennsylvania, Philadelphia, PA

ABSTRACT

Recent developments in boron chemistry have allowed the synthesis of TiN/TiB$_2$ composites from polymeric precursors with grain sizes of the order of 10-500 nm. In order to optimize the properties through controlled processing, nucleation of the crystalline phases and subsequent microstructural evolution must be understood. However, the nitride and boride phases are difficult to distinguish in conventional TEM since the grains are too small for diffraction analysis and light elements are not detectable by energy dispersive X-ray spectroscopy.

For the characterization a prototype of an energy filtering TEM (EFTEM) which utilizes an imaging electron energy loss spectrometer incorporated into the column of a normal TEM has been used for elastic filtering and electon spectroscopic imaging (ESI). The ESI-technique allows us to obtain two-dimensional maps of the elemental distribution. These techniques are applied to advantage in the microstructural anaysis of the TiN/TiB$_2$ nanocomposites.

INTRODUCTION

A central objective in materials research is on the one hand the developement of new materials, and on the other hand the microstructural and microanalytical characterization of these materials. Advances in the synthesis of B and N-containing polymeric precursors into ceramics have been made [1, 2, 3]. It is now possible to obtain TiN/TiB$_2$ nanocomposites with high ceramic yield. One important tool for characterizing these newly developed materials therefore is transmission electron microscopy (TEM).

In conventional transmission electron microscopy (CTEM) only the transmitted and elastically scattered electrons can be used for imaging whereas the contribution of inelastically scattered electrons to an image is useless in most cases. In analytical microscopy (AEM) inelastic scattering processes due to the interaction of the incident electron beam with the specimen are used for local chemical analysis: emitted X-rays and electrons with characteristic energy losses can be analyzed with appropriate detectors. The development of a new imaging energy loss spectrometer which is integrated into a column of a normal TEM [4] allows energy filtered images or diffraction patterns to be recorded. Inelastically scattered electrons can be utilized for imaging.

ENERGY FILTERED TRANSMISSION ELECTRON MICROSCOPY

The electron spectroscopic imaging (ESI) method [5] is based on the inelastic scattering processes between the fast incident electrons and atomic electrons of the sample. These inelastic scattering processes lead to energy losses which can be seen in an electron energy loss spectrum (Fig. 1) as a plasmon peak and as characteristic edges with an onset energy ΔE (the characteristic edges for each element correspond to the ionization energies of the atom). Unscattered and elastically scattered electrons (no energy loss) are visible in the zero loss peak of the spectrum.

The most important applications of an imaging spectrometer are the elastic (or zero-loss) filtering, elemental mapping and parallel EELS detection [6, 7]. In the first case inelastically scattered electrons are removed so that the images (microstructures, diffraction patterns) become

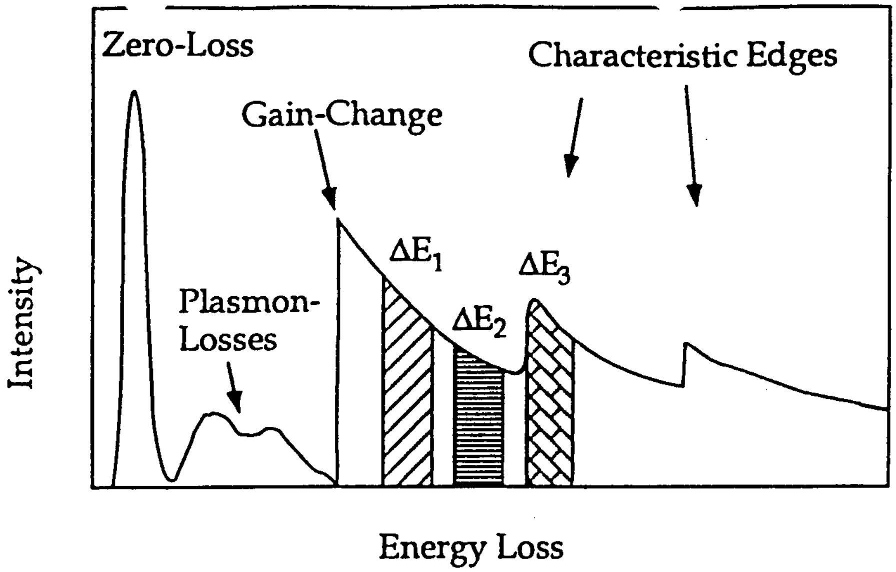

Figure 1: Schematic EELS spectrum, showing the three window technique used for elemental mapping.

sharper. In the second case electrons within a certain range of energy loss are selected with a slit and contribute to an electron spectroscopic image. The ESI technique allows us to obtain two-dimensional maps of the elemental distribution in the irradiated sample area. The combination of different elemental maps also enables conclusions to be drawn about the phase composition. A spacial resolution of 1 - 2 nm can be reached in ESI images. This method is suitable for imaging the distribution of light elements (e.g. B, C, N, O) in a sample, but elements of higher atomic numbers (e.g. Al, Si, Ti, Fe, Ni) can also be sucessfully imaged.

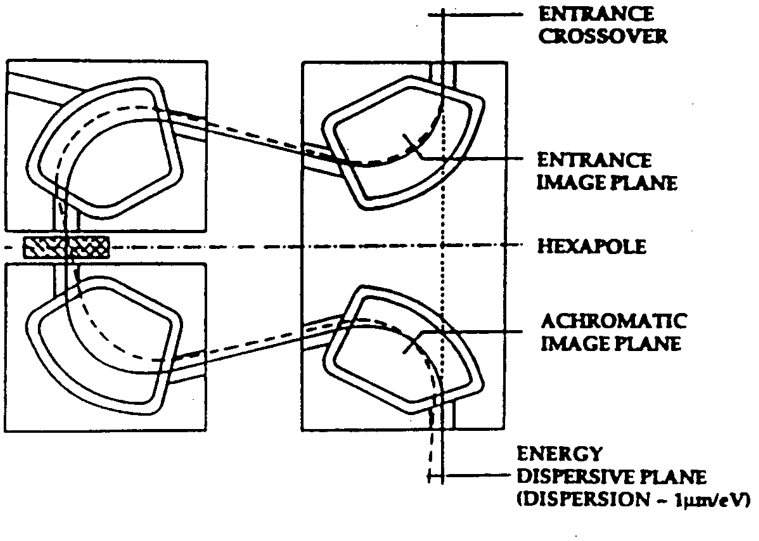

Figure 2: Schematic ray path in the Omega imaging filter.

We have utilized a prototype of the first commercially available TEM/STEM featuring an integrated imaging Omega type energy filter, the Zeiss EM 912 Omega. The energy filter is placed between the third and fourth projector lens, a fifth lens has been added to the projector system. The energy filter comprises four sector magnets in a symmetric arrangement (Fig. 2). The filter entrance plane contains either an image or a diffraction pattern. The entrance image plane and the crossover are transferred on an Ω- shaped path to the achromatic image plane and the energy disper e plane, respectively. Both planes can maged on the viewing screen. Additionally the microscope is equipped with a SIT 66 TV rate camera, 512 x 512 pixel, connected to an image processing system and a 1024 x 1024 slow scan CCD camera, connected to an Apple Macintosh II FX.

Energy filtered images are obtained by selecting particular energy losses with an energy selecting slit in the energy dispersive plane of the imaging filter: the energy loss spectrum is shifted along the slit by increasing the accelerating voltage at the cathode to $U = U_0 + \Delta E$ so that inelastically scattered electrons with the energy loss ΔE are in focus. The energy filtered images are recorded with a camera; they are digitized and the intensities are stored for each pixel. The calculated difference image is finally enhanced by image processing to reduce the noise and sharpen the contours.

For an elemental distribution image three energy filtered images at different energy losses have to be acquired (see Fig. 1): two images at two different energy losses below the characteristic edge (ΔE_1 and ΔE_2) and one image above the energy loss edge (ΔE_3). The images taken at the energy losses ΔE_1 andΔE_2 are used for a background extrapolation. The signal of the element of interest is the total signal intensity at the energy loss ΔE_3 minus the intensity of the extrapolated background. A cautionary note is that the same thickness sensitivity that plagues other electron energy loss measurements in a TEM is also inherent in ESI.

EXPERIMENTAL

Composite samples were prepared by adding 34.32 g titanium metal (325 mesh size) to dry tetrahydrofuran solution containing 14.2 g polyborazylene. The solvent was vacuum evaporated while maintaining ultrasonic agitation to achieve a homogeneous dispersion. The resulting dispersion was ground into a fine powder under a nitrogen atmosphere. Two to four grams of the precursor powder were isostatically pressed at 75000 psi into bars. The green bodies were then heated in a tube furnace under an Ar atmosphere to 650°C, held for 10 min and annealed for the times and temperatures as follows: 1000°C/49 hrs, 1200°C/1 hr, 1200°C/3 hrs 1450°C/1 hr and 1450°C/1 day, respectively.

From the bulk material TEM samples were prepared using a cross section preparation technique [8]. This technique allows the preparation of stable, self supporting TEM samples even from brittle and porous materials. The samples were mechanically ground, dimpled and ion beam milled. Finally they were coated with a thin carbon layer.

Boron, N, O and Ti elemental distribution images have been acquired at an incident energy of 120 kV. The K-edges have been used for the elements B, N and O, the $L_{2,3}$ edge has been used for Ti with the energy losses 188 eV, 401 eV, 532 eV and 455 eV, respectively. The selected slit widths were 10 - 15 eV for B and 15 - 20 eV for N, O and Ti. The total acquisition time for an elemental map was about 20 - 30 s. Titanium, N, and B elemental distribution maps are superimposed by representing the different elements in color to distinguish between the TiN, TiB_2 and BN phases.

RESULTS AND DISCUSSION

The heating of the green body at 1000°C/49 hrs leads to a crystallization of TiB_2 with grain sizes between 100 and 200 nm. The crystal size of TiN grains lies between 0.5 and 1.0 μm. Furthermore large amounts of amorphous BN can be found. Cracks between TiB_2 crystals and amorphous BN are quite frequent due to the different thermal expansions of both phases. Oxygen (in the form of TiO_2 or B_2O_3) could not be found.

Figures 3 and 4 show elemental maps of B, N and Ti with the corresponding TEM micrographs from a 1200°C/1 h sample. It can be seen that the TiB_2 grains are more elongated whereas the TiN grains seem to be more equiaxed. In the TEM micrograph (Fig. 3) the phases TiN and TiB_2 cannot be distinguished. Only in the elemental maps both phases can be identified. Amorphous BN (Fig. 4) can be found. The grain size of TiB_2 varies between 100 and 200 nm, the TiN grains have crystal sizes between [illegible] and 1.0 μm. After 3 hrs a slight grain growth of TiN can be observed: grains of 1.5 μm can be found. Amorphous BN is still present, the grain size of TiB_2 seems to be constant.

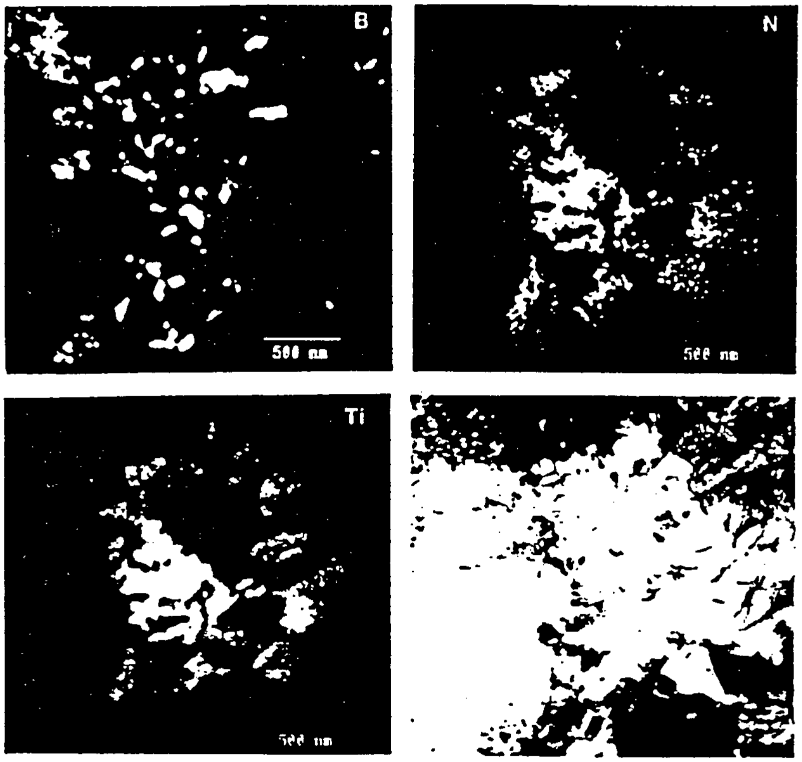

Figure 3: Elemental maps of B, N and Ti with the corresponding TEM micrograph. The phases can be deduced from the elemental maps. T=1200°C.

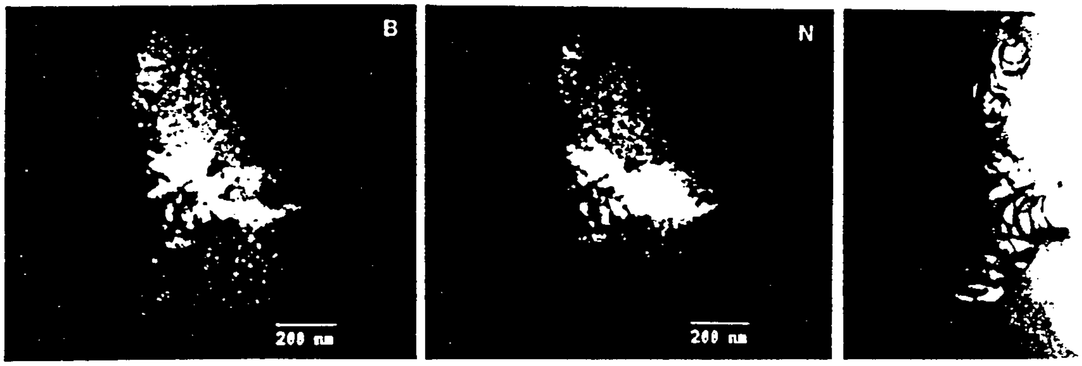

Figure 4: Elemental maps of B and N, indicating the presence of BN. A solution of Ti in the amorphous BN can not be detected. At the right side the corresponding TEM micrograph. T=1200°C.

Heating the green body at 1450°C leads to significant changes in the microstructure: the TiB_2 grain size increased, after 1 h grain sizes of 0.2 to 0.5 μm can be measured. The grain size of TiN is between 0.5 to 1.5 μm. The most significant change is the crystallization of the amorphous BN into a turbostratic like BN. Figures 5 and 6 show the distributions of B, N and Ti and the corresponding TEM micrographs. The EELS spectra of TiN and BN (Fig. 6) show why the N-signal is rather weak in the N-image of TiN whereas it can easily be detected in the N-image of BN.

The micrographs show that TiB_2 grains are an order of magnitude to a factor of 3 smaller than

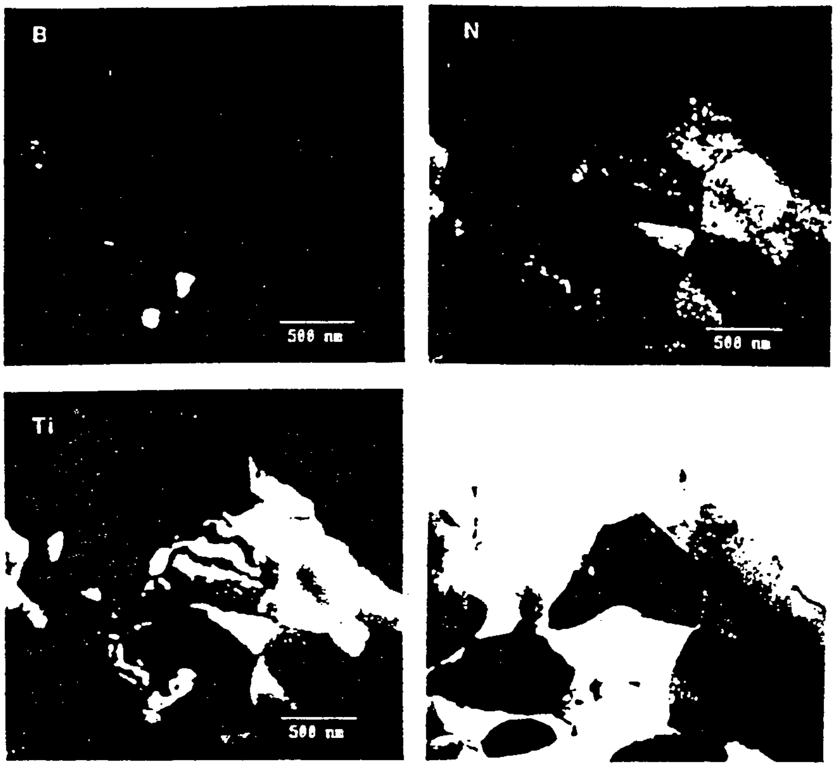

Figure 5: Phase distribution of TiN/TiB$_2$ at 1450°C after 1 h. The arrows indicate TiB$_2$.

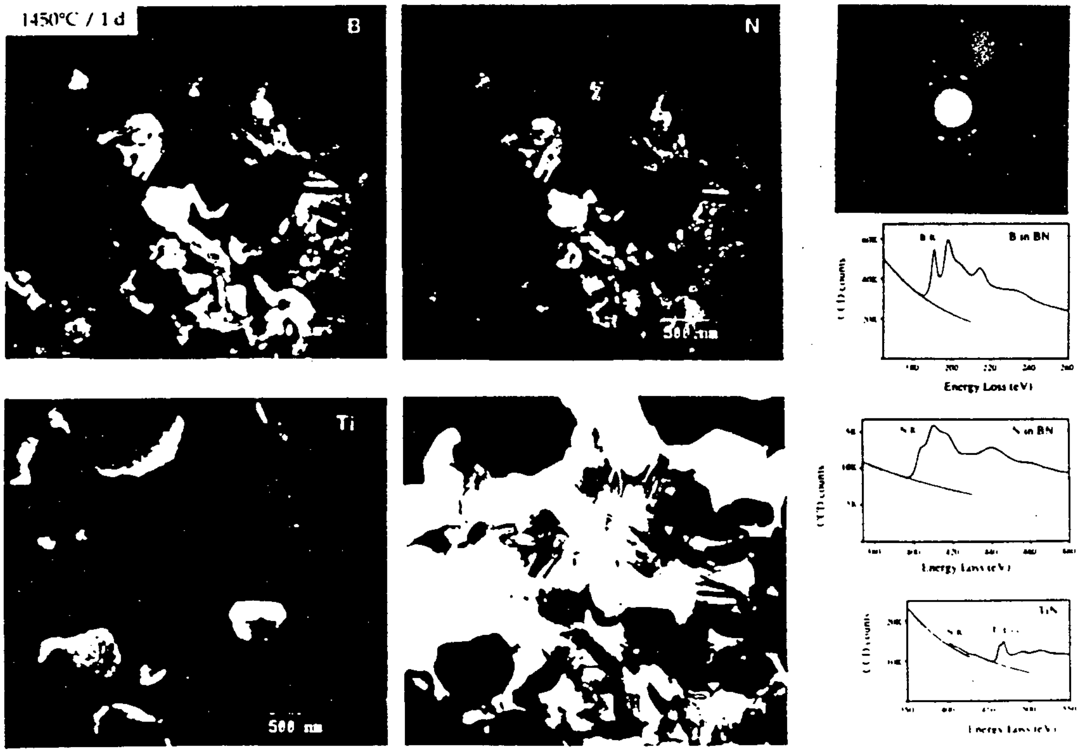

Figure 6: TEM micrograph and elemental maps of BN/TiN. The diffraction pattern of BN and the parallel EELS spectra of both phases, recorded with the CCD camera, are shown at the right.

the TiN grains. This suggests TiB_2 has a higher nucleation frequency and/or a lower growth rate than TiN under the processing conditions studied here. The observed grain coarsening of TiN and TiB_2 can also be observed by X-ray measurement [9]. The presence of BN (amorphous and crystalline) is an indication that small local changes in composition lead to changes in the morphology of the material.

SUMMARY AND CONCLUSIONS

A high yield synthetic route to TiN/TiB_2 composites based upon polymer precursors has been developed. Different TiN/TiB_2 composites have been produced under different conditions to study the microstructural development of the phases. Electron spectroscopic imaging was successfully utilized to characterize the microstructures. At temperatures below 1450°C TiN/TiB_2 and amorphous BN were found, at 1450°C the BN is crystallized. A slight grain growth of TiN/TiB_2 could be observed. The most significant difference between the TiN and TiB_2 phases is the difference in size and shape of the grains. Electron spectroscopic imaging has enabled us to distinguish in short times those two phases which otherwise could not have been separated by conventional analytical TEM methods.

ACKNOWLEDGEMENTS

This work was supported by the Bundesministerium für Forschung und Technologie (BMFT) under contract No. NTS 0215/8 (VS and MR), the Air Force Office of Scientific Research (MN and DB) and the National Science Foundation (KS and LS). The authors gratefully acknowledge helpful discussions with J. Mayer.

REFERENCES

1. M. G. Mirabelli and L. G. Sneddon, Inorganic Chem. 27, 3271 (1988).
2. P. J. Fatzen, J. S. Beck, A. T. Lynch, E. E. Remsen, and L. G. Sneddon, Chem. Mater 2, 96 (1990).
3. K. Su, M. Nowakowski, D. Bonnell, and L. Sneddon, Chem. Mater. , in press (1992).
4. S. Lanio, Optik 73, 99 (1986).
5. L. Reimer, Advances in Electronics and Electron Physics 81, 43 (1991).
6. M. Rühle et al., Electron spectroscopic imaging and diffraction, in *Proceedings of the 49th Annual Meeting of the EMSA*, edited by G. W. Bailey, pages 706–707, San Francisco Press, Inc., 1991.
7. J. Mayer, Electron spectroscopic imaging and diffraction: Applications in materials science, in *Proceedings of the 50th Annual Meeting of the EMSA*, edited by G. W. Bailey, J. Bentley, and J. A. Small, pages 1198–1199, San Francisco Press, Inc., 1992.
8. U. Salzberger, A. Strecker, and J. Mayer, Tem specimen preparation: a universal method for cross sections and brittle materials, in *Proceedings of the 10th European Congress on Electron Microscopy*, edited by A. López-Galindo and M. I. Rodríguez-García, volume 2, pages 743–744, Secretariado de Publicaciones de la Universidad de Granada, 1992.
9. M. Nowakowski et al., to be published .

Submitted to the Journal of Materials Research

SYNTHESIS, PROCESSING, AND MICROSTRUCTURAL EVOLUTION OF TiN/TiB_2 COMPOSITES FROM A POLYMERIC PRECURSOR

M. Nowakowski, #K. Su, *V. Szabo, #L. G. Sneddon, *M. Ruhle, D. Bonnell

Department of Materials Science and Engineering
The University of Pennsylvania, Philadelphia, PA

#Department of Chemistry
The University of Pennsylvania, Philadelphia, PA

*The Max-Planck-Institut fur Metallforschung
Stuttgart, Germany

ABSTRACT

A high yield synthetic route to TiN/TiB_2 composites based upon a polymeric precursor approach has been developed. The phase evolution and microstructural development have been characterized and related to preliminary measurements of properties, i.e. hardness. The small size of the grains and the fact that the phases differ chemically in light element content necessitated the used of a new TEM imaging technique for microstructural characterization. The technique, utilizing an energy filter and referred to as electron spectroscopic imaging (ESI), is described in detail.

[Key words: nanocomposite, TiN, TiB_2, processing, synthesis, electron spectroscopic imaging, TEM]

4/3/93

INTRODUCTION

Recent developments in the use of polymeric precursors to ceramics have been motivated by the potential for strict control of stoichiometry, complex shape forming, and low temperature processing.[1] By taking advantage of the formability of the starting material, coatings, films and near net shape for complex geometries might be obtained. Furthermore, molecular level control of chemistry inherent in this approach could be exploited to produce ceramic composites with fine morphological structure, perhaps on nanometer scales. These advantages have spurred the development of a number of polymeric synthetic routes to ceramics, one of the most visible being the commercialization of the polycarbosilane-to-SiC reaction to form fibers.[2] A number of boron-based polymer systems[3], have also been shown to produce ceramics including BN and B_4C in a controllable fashion upon pyrolysis. These polymers have exhibited properties important to potential applications such as coatings in structural ceramic composites, wear resistant films, oxidation-resistent fibers and high temperature electronics. The use of preceramic polymers as reactants to synthesize other boron based ceramics has also been reported.[4,5,6]

Among structural ceramics, metal borides and nitrides are of special interest because of their high melting points, hardness and chemical resistance at high temperatures.[7,8] We recently demonstrated that the synthesis of monolithic TiB_2/TiN composites can be achieved by a process based on the reaction of the boron-nitrogen polymer, polyborazylene, with titanium metal powder.[9] In order to control the properties of these composites, we must understand the morphological development and the relationship between microstructure and properties, as well as the chemical processes involved in the polymer to ceramic conversion reaction. Since light elements (N, C, O, etc.) are an intrinsic part of these systems, a new technique is necessary to characterize the materials. Experimental details are first summarized, including an in-depth description of the imaging technique in the transmission electron microscope (TEM) referred to as electron spectroscopic imaging (ESI). Synthesis methods and results are presented after which phase evolution is documented. Morphologies are characterized and correlated with preliminary measurements of properties, i.e. hardness. Finally the results are summarized with respect to implications to thermodynamics and processing parameters.

EXPERIMENTAL PROCEDURES

Materials Processing

All manipulations of the preceramic materials were carried out using standard high vacuum or inert-atmosphere techniques as described by Shriver.[10] Polyborazylene was prepared according to the published method.[11] Pyrolysis under 2000°C was performed in a Linberg Tube Furnace under argon atmosphere, while pyrolysis at 2000°C was achieved in a graphite resistance furnace (Astro Industry Hot Press Model 1000-3070 HP) under vacuum.

In a typical process, 34.32 g of titanium metal (325 mesh, Strem Chemicals) was added to a sodium-dry tetrahydrofuran solution containing 14.2 g polyborazylene. The solvent was then vacuum evaporated while maintaining ultrasonic agitation. The resulting black solid dispersion was ground to a fine powder under a nitrogen atmosphere. Two to four grams of precursor powder was isostatically pressed at 75,000 psi. The resulting green bodies were divided into two groups. Group 1 samples were heated (2°C/min) to 800°C and held for 9.5 h under an argon atmosphere. After being cooled to room temperature, the ceramic bars were annealed at higher temperatures as summarized in Table 1. The pyrolysis of group 2 samples was carried out in two continuing ramps: the green bodies were first heated to 650°C (5°C/min) under Ar and held for ~10 min, then they were annealed at higher temperatures. The reaction conditions and results are summarized in Table 2.

Two powder samples were processed under different conditions. A 0.74 g sample of powdered solid dispersion was heated (2°/min) to 800°C and held for 9.5 h under Ar. Yield: 0.69 g; Ceramic yield: 93.2%. Elemental analysis: Ti: 65.8%; B: 9.80%; N: 12.3%; O: 8.58%; C: 0.66%; H: 0.70%. In another experiment, a 0.78 g sample was heated (10°C/min) to 1450°C and held for 10 h under Ar. Yield: 0.69 g; Chemical yield corresponding to metal: 91.8%; Ceramic yield: 88.5%. Elemental Analysis: Ti: 73.4%; B: 8.31%; N: 12.2%; O: 2.91%; C: 2.66%; H: < 0.1%.

Materials Characterization and Properties

X-ray powder diffraction (XRD) spectra were recorded on a Rigaku Geigerflex X-ray diffractometer using Cu Kα radiation. Quantification of the relative phase amounts was accomplished using silicon powder as a standard. The uncertainty due to measurement error is less than 2%. Thermogravimetric analyses (TGA) were performed on Seiko

TG/DTA 320. Densities were measured by water displacement method. Elemental analyses were performed by Pascher, (Postfach 2129, 5480 Remagen 2, Germany).

TEM foils were prepared with standard methods; sectioning into 3 mm discs, polishing to 200 mm., dimpling to 50 mm, and ion milling at 9° for 1-5 hours. General microstructural characterization (i.e. grain size determination) was performed in a Philips 400 with point-to-point resolution of 3 Å. However, the small grain size and chemical differences in light element content conspire to make phase distinction difficult with conventional TEM and typical selected area aperture sizes. Therefore, microstructural evolution relied primarily on electron spectroscopic imaging (ESI)[12] The electron spectroscopic imaging (ESI) method is based on the inelastic scattering processes between the fast incident electrons and atomic electrons of the sample. These inelastic scattering processes lead to energy losses which result in an electron energy loss spectrum (Fig. 1) with a plasmon peak and several characteristic edges, each edge with an onset energy, ΔE. The edges correspond to ionization energies of the atom. Unscattered and elastically scattered electrons (no energy loss) result in the zero loss peak of the spectrum.

The most important applications of an imaging spectrometer are the elastic (or zero-loss) filtering, elemental mapping and parallel EELS detection[13] [14] [15]. In the first case, inelastically scattered electrons are removed so that the images (microstructures, diffraction patterns) become sharper. In the second case, electrons within a certain range of energy loss are selected with a slit and allowed to contribute to an electron spectroscopic image. The ESI technique allows two-dimensional maps of the elemental distribution to be obtained. The combination of different elemental maps also enables conclusions to be drawn about the phase distribution and composition. A spatial resolution of 1-2 nm can be achieved in ESI images. While this method is unique in its ability to image the distribution of light elements (e.g., B, C, N, O), elements of higher atomic numbers (e.g., Al, Si, Ti, Fe, Ni) can also be successfully imaged.

We have utilized a prototype of the first commercially available TEM/STEM featuring an integrated imaging Omega type energy filter, the Zeiss EM 912 Omega. The energy filter is placed between the third and fourth projector lens, a fifth lens has been added to the projector system. The energy filter comprises four sector magnets in a symmetric arrangement (fig. 2). The filter entrance plane contains either an image or a diffraction pattern. The entrance image plane and the crossover are transferred on an Ω-shaped path to the achromatic image plane and the energy dispersive plane, respectively. Both planes can be imaged on the viewing screen. Additionally, the microscope is equipped with a SIT 66 TV rate camera, 512x512 pixel, connected to an image processing system and a 1024x1024 slow scan CCD camera, connected to an Apple Macintosh II FX.

Energy filtered images are obtained by selecting particular energy losses with an energy selecting slit in the energy dispersive plane of the imaging filter: the energy loss spectrum is shifted along the slit by increasing the accelerating voltage at the cathode to $U = U_0 + \Delta E$ so that inelastically scattered electrons with the energy loss ΔE are in focus. An energy filtered image is recorded with a camera and digitized, i.e. the intensity of each pixel is stored. For an elemental distribution image three energy filtered images at different energy losses must be acquired (see Fig. 1): two images at energy losses below the characteristic edge (ΔE_1 and ΔE_2) and one image above the energy loss edge (ΔE_3). The images acquired at the energy losses ΔE_1 and ΔE_2 are used for a background extrapolation. The signal of the element of interest is the total signal intensity at the energy loss ΔE_3 minus the intensity of the extrapolated background. Finally, the calculated difference image is enhanced by image processing to reduce the noise and sharpen the contours. (A cautionary note is that the same thickness sensitivity that plagues other electron energy loss measurements in a TEM is also inherent in ESI.)

Elemental distribution images have been acquired at an incident energy of 120 kV using the K-edges for B, N, and O, the $L_{2,3}$ edge for Ti with the energy losses 188 eV, 401 eV, 532 eV and 455 eV, respectively. The selected slit widths were 10-15 eV for B and 15–20 eV for N, O and Ti. The total acquisition time for an elemental map was about 20 – 30s. Titanium, N, and B elemental distribution maps can be superimposed by representing the different elements in color to distinguish between the TiN, TiB_2 and BN phases.

Hardness was measured by microindentation with a diamond shaped indentor using the usual relation: $H=P/2a^2$; where P is the load and a is the half-diagonal length.

RESULTS AND DISCUSSION

Synthesis and Phase Evolution

We have previously reported the preparation of the new boron-nitrogen polymer, polyborazylene, $(B_3N_3H_4)_x$, and shown that this polymer can be converted to boron nitride in high ceramic and chemical yields (90-94%).[8] We have now found that the reactions of polyborazylene/titanium metal dispersions leads to the formation of TiB2/TiN composites in both high chemical and ceramic yields. The final product can be produced in either in powder or monolithic form depending on the processing conditions.

$$(B_3N_3H_4)_x + Ti \rightarrow TiN/TiB_2 + H_2$$

Since polyborazylene functions as both a reactant and a binder in this system, a monolithic green body was readily made by isostatic pressing at room temperature. The pyrolysis of the green body yielded a composite that exhibited excellent shape retention with final density dependent upon the annealing temperature and time. For example, an increase in density from 2.98 to 3.90 observed in group 1 samples is associated with increases in annealing temperatures (for constant times) from 800° to 1450°C. Significant densification was observed at both 1000°C and 1200°C (group 2) as a function of annealing time. In contrast, samples treated at 1450°C for 1 h and 17 h decreased in density from 4.13 to 3.94 which may result from the evaporation of B_2O_3 and NO at temperatures above 1200°C formed by reaction with TiO_2 impurity. Based on these results, the use of titanium metal with less oxide impurities should then enable an increase the bulk density of the final composite. The ceramic powders prepared at 800°C and 1450°C have compositions of $Ti_{1.0}B_{0.66}N_{0.64}H_{0.51}O_{0.39}C_{0.04}$ and $Ti_{1.0}B_{0.50}N_{0.57}H_{0.06}O_{0.1}C_{0.14}$, respectively. The 1450°C material is consistent with a $(TiN)_{0.57}(TiB_2)_{0.25}Ti_{0.18}O_{0.1}C_{0.14}$ mixture. The nitrogen and boron contents, relative to titanium, are lower for the 1450°C material than for the 800°C material, suggesting that the reduction of TiO_2 involves both nitrogen and boron.

A TGA study of the ceramic conversion reaction showed weight losses in the ranges of 50-300° and 450-800°C, similar to those observed in the conversion of pure polyborazylene to boron nitride. At 1350°C an additional weight loss was observed which, consistent with an observed decrease in the oxygen content of materials treated above this temperature, further supports the evaporation of B_2O_3 and NO produced by the reduction of titanium oxide impurities by boron and nitrogen.

X-ray diffraction studies of the ceramic conversion reaction have shown that the product exhibits variations in composition and crystallinity with processing temperature and/or time. As shown in the diffraction patterns of the samples described in Table I (in Figure 3), there appears to be little reaction between the polymer and the titanium metal when the sample was heated at 800°C for 9.5 h. Consistent with this conclusion, elemental analyses of a sample at this point showed that the material still had a significant hydrogen content with the observed $B_{1.03}$:$N_{1.0}$:$H_{0.79}$ ratios, suggesting that polymer crosslinking was still occurring. When the sample was heated at 1000°C for 2 h, the titanium metal was completely consumed by reaction with the polymer and crystalline titanium nitride was initially observed. The pattern obtained from the the sample annealed at 1200°C for 2 h clearly indicates the presence of both crystalline TiB_2 and TiN. The decreased line widths in the pattern from the sample heated at 1450°C compared to that from the sample heated at 2000°C indicates that grain coarsening occurred at high temperature. Although not detected in the X-ray diffraction pattern, TEM imaging shown in figure 10 provides evidence that some BN crystallizes during the reaction.

The phase development with time at various temperatures was investigated with the samples described in Table II. As shown in figure 4, when the sample was heated for 1 h, TiN was observed to form. At this point, the existence of unreacted Ti metal was still clearly evident. It should be noted that a large amount of amorphous phase resulting in diffuse scattering intensity centered at 18° was also observed. When the sample was heated for 3.8 h an increase in crystalline TiN phase, along with a further decrease in Ti, was observed. After 49.0 h the Ti was completely consumed leaving the major crystalline phase, TiN, together with small amounts of TiB_2. The relative amount of amorphous phase in all samples decreased with annealing time suggesting that crystalline TiN -TiB_2 is achieved in two steps: the initial chemical reaction of titanium metal to produce amorphous titanium - nitride - boride, followed by the crystallization of TiN and TiB_2.

The phase assemblages from different processing conditions are shown in figure 5, which compares intensities of the primary peaks of each crystalline phase at times and temperatures listed in the table. Note that for all temperatures investigated TiN and TiB_2 appear to crystallize simultaneously in about a 2:1 ratio. Some deviation occurs on very long anneals (50 hrs or 120 hrs for 1000 °C and 1200 °C respectively), after which the TiN content is somewhat increased as the system equilibrates with a ratio of 2.27:1.

Assuming that the heating rates used in this study result in complete hydrogen loss from the polymer by 1000 °C, then the fact that all processing conditions result in two crystalline phases, TiN and TiB_2, suggests that a TiN-TiB_2 tie line exists in the Ti-B-N subsolidus equilibrium phase diagram. Further evidence for the existence of this tie line is that small deviations in composition around the proposed tie line result in BN, which further implies the TiB_2-BN and TiN-BN compatibilities. The proposed relationships are shown schematically in figure 6. This can be compared to the work of Matsudaira et al[16] who find that the solid state reaction of amorphous B and TiN does not proceed in a N overpressure but yields TiB_2 in an Ar overpressure. Their result implies the existence of a tie line between TiN and B. The latter tie line would be in contradiction to the TiB_2-BN and TiN-BN compatibilities but not TiN-TiB_2. Further work is obviously necessary to determine the complete diagram. The phase equilibria will obviously be dependent on nitrogen activity, as emphasized by this earlier work, and diagrams such as figure 6 represent sections of constant N activity. Thus, although unlikely, it is possible that all of the proposed compatibilities do exist but those in contradiction exist on different planes of nitrogen activity. Regardless of the consequent uncertainty to the BN-TiN-N section of the diagram, the TiN-BN-B-Ti sections should not be affected unless mass is lost to the system as a result of changing N atmosphere.

Microstructural Evolution

Samples 2-5, 2-6 and 2-9 are discussed to illustrate the effect of processing on morphology. The most notable characteristic of the microstructure is the difference between the TiN and TiB_2 grain size and shape. Since all of the grains are relatively small, the phases could not be distinguished by conventional dark field imaging. Since the chemical difference resides in the light element content, EDAX could not be used to distinguish the phases. However, ESI allowed identification of the morphology of the various phases.

Annealing at 1000°C for 49 hrs leads to partial crystallization of the material. The grain size of TiB_2 ranges from 100 to 200 nm, while that of TiN ranges from 0.5 to 1.0 µm. Furthermore, large amounts of amorphous BN are present. We have noted that cracks between TiB_2 crystals and amorphous BN are quite frequent, presumably due to the difference in coefficient of thermal expansion of the phases. Oxygen, dissolved in the matrix or in the form TiO_2 or B_2O_3 was not detected.

Images acquired with energy losses of B, N, and Ti, with the corresponding TEM bright field image from the sample annealed 1200 °C for 1 hr are shown in figures 7. As can be seen, the TiB_2 grains are elongated whereas the TiN grains appear more equiaxed. In the bright field image the TiN and TiB_2 phases cannot be distinguished; only by comparing the elemental maps can the phases be identified. The grain size of TiB_2 varies between 100 and 200 nm, while that of TiN varies between 0.5 and 1.0 µm. Amorphous BN was detected by EELS and electron diffraction with the texture illustrated in figure 8. After 3 hrs slight grain growth of TiN is observed, i.e. grains of 1.5 µm can be found, but the grain size of TiB_2 appears to be constant. The amorphous BN is still present.

Annealing at 1450 °C results in a significantly different microstructure in that this material is the most completely reacted and fully crystallized of the series of samples. The TiB_2 grain size is larger, after only 1 hr grains of 0.2 to 0.5 μm are observed, while that of TiN is between 0.5 and 1.5 μm (figure 9). The most striking variation in microstructure is the ordering of the residual amorphous BN into a turbostratic-like structure as shown in figure 10.

As noted above, amorphous phase was detected in several samples. In the first stage of the reaction (800 °C for 1 hr. for example) the sample is predominantly amorphous, as might be expected. In subsequent stages of the reaction some regions of the amorphous phase exhibited texture as illustrated in figure 8. These regions have a high B and N content, as indicated by EELS. In extreme cases turbostratic BN developed with a morphology typical of that in figure 10. Note by comparing these TEM observations with the x-ray data in Table II that BN was not detected by x-ray diffraction because any even the highest intensity crystalline peak could be hidden under the diffuse diffraction from the residual amorphous phase.

Measurements of grain sizes are summarized in Table II. The fact that the TiB_2 grains are an order of magnitude to a factor of 3 smaller than the TiN grains suggests that under the processing conditions studied here, the TiB_2 has a substantially higher nucleation frequency and/or much smaller growth rate than does the TiN. The observed grain coarsening is also evident in the x-ray diffraction patterns (figure 3). Although the rates and activation energies are not quantified here, this information will be exploited to control the final morphology of future materials.

Properties

Preliminary measurements of hardness, listed in Table III, indicate that the TiN-TiB_2 composites made from the polymer precursor described here exhibit hardnesses much lower than that previously reported for bulk TiB_2 but on the same order as that reported for films. Porosity in the samples resulted in a large scatter in the measurements; therefore, possible trends with phase content could not be confirmed. However, within sets of samples processed at a single temperature the hardness did increase with density. Thus, further work on this system is indicated.

SUMMARY

In summary, a high yield synthetic route to TiN/TiB_2 composites based upon a polymeric precursor approach has been developed. Phase evolution and microstructural development have shown that the nitride and boride phases have very different morphologies and, at present, samples contain a residual amorphous phase. These results also provide evidence for the existence of a $TiN-TiB_2$ compatibility in the $TiN-TiB_2-BN$ system.

Acknowledgements

This work was supported by Air Force Office of Scientific Research under grant # AFOSR-91-0103 (DB and MN), the Department of Energy, Division of Chemical Sciences, Office of Basic Energy Sciences, the National Science Foundation Materials Research Laboratory at the University of Pennsylvania (LS and KS), and the Bundesministerium fur Forschung and Technologie (BMFT) under contract # NYS 0215/8 (MR and VS). We are grateful to J. Mayer for many helpful discussions concerning energy filtered TEM.

Table 1. Summary of Reaction Conditions.

Sample #	T (°C)	Time (h)	Cer. yield (%)	d (g/cm^3)
1-1	800	9.5	99.1	2.98
1-2	1000	2	96.0	3.47
1-3	1200	2	95.5	3.81
1-4	1450	2	91.9	3.90
1-5*	2000	2	88.6	3.63
2-1	870	1.0	98.0	2.59
2-2	1000	1.0	98.2	2.82
2-3	1000	3.8	98.8	3.16
2-4	1000	49.0	99.5	3.29
2-5	1200	1.0	97.5	3.49
2-6	1200	3.0	98.4	3.73
2-7	1200	67.5	98.6	3.70
2-8	1200	126.0	96.1	4.18
2-9	1450	1.0	94.9	4.13
2-10	1450	17	91.6	3.49

* 1-5 was anealeded in vacuo, while 1-2 to 1-4 were under Ar.

TABLE II. Phase Evolution and Hardness of TiN/TiB_2 with Processing Conditions

Processing Conditions	TiN:Si peak ratio	grain size (μm)	TiB2:Si peak ratio	grain size (μm)
800 C, 16hrs	0	0	0	0
1000 C, 3.5 hrs	0.849		0.194	
1000 C, 49 hrs	2.77	0.5-1.0	0.800	0.1-0.2
1200 C, 1 hr	3.24	0.5	1.09	nm
1200 C, 3 hrs	2.01	0.5-1.5	0.73	nm
1200 C, 72 hrs	3.81		1.74	
1200 C, 126 hrs	6.26		2.57	
1450 C, 1 hr	8.15	0.5-1.5	3.90	0.2-0.5
1450 C, 17 hrs	7.58	0.5-1.5	4.34	0.5
2000 C, 16 hrs		0.5-1.5		0.5

* Ratios are based on the TiB2 (101), TiN (200), BN (111), and Si (111) peaks.

Table III. Properties of TiN/TiB$_2$ Composites

Sample	Rel. Density	Hardness
2-2	56%	0.7 GPa
2-3	63%	2.3 GPa
2-4	66%	1.3 GPa
2-5	70%	1.6 GPa
2-7	75%	1.6 GPa
2-8	84%	1.9 GPa
2-9	83%	1.0 GPa
2-10	70%ø	0.5 GPa

REFERENCES

1 K. Wynne, R. Rice *Annual Rev. Mat. Sci.* **14** (1984) 297-334.

2 S. Yajima, *Am. Ceram. Soc. Bull.* 62 (1983) 893.

3 (a) Paine, R. T.; Narula, C. K. *Chem. Rev.* **90** (1990) 73-91.
(b) L. G. Sneddon, M. G. L. Mirabelli, A. T. Lynch, P. J. Fazen, K. Su, J. S. Beck. *Pure and Applied Chemistry* 63, (1991) 407-410.

4 D. Seyferth, N. Bryson, D. P. Workman, C. A. Sobon. *J. Am. Ceram. Soc.* 74 (1991) 2687-2689.

5 (a) Greil, P.; Seibold, M. *Ceram. Trans.* **1991**, *19*, 43-49.
(b) Greil, P.; Seibold, M. *Adv. Mater. Processes, Proc. Eur. Conf.* Exner, H. E.; Schumacher, V. Eds., DGM Informationsges: Oberursel, 1990; vol. 1, p 641-646.
(c) Greil, P.; Seibold, M. *J. Mater. Sci.* **1992**, *27*, 1053-1060.

6 J. Mayer, Proceedings of 49th Annual Meeting of EMSA ed. G. W. Bailey, J. Bentley and J. A. Small San Francisco Press, Inc. (1992) 1198-1199.

7 For general review of the syntheses, structure and properties of metal borides see: (a) Greenwood, N. N; Parish, R. V.; Thornton, P. Q. *Rew.* **1966**, 20 441-461.(b) Matkovich, V. I. *Boron and Refractory Borides*; Springer-Verlag: New York, 1977. (c). Post, B. In *Boron, Metallo-Boron Compounds and Boranes*; Adams, R. M., Ed. Interscience: New York, 1964; pp 301-372. (d) Greenwood, N. N. *The Chemistry of Boron*; Pergamon: New York, 1975; pp 697-731. (e) Thompson, R. In *Progress in Boron Chemistry*; Pergamon: New York, 1970; Vol. 2, pp 173-230. (f) Hoard, J. L.; Hughes, R. E. In *The Chemistry of Boron and Its Compounds*; Muetterties, E. L., Ed.; Wiley: New York, 1967; pp 25-154.

8 For general review of the syntheses, structure and properties of metal nitrides see: (a) Toth, L. E. *Transition Metal Carbides and Nitrides* Academic Press, New York, 1971; pp1-28. (b) Johansen, H. A. Recent Development in the Chemistry of Transition Metal Carbides and Nitrides, In *Survey of Progress in Chemistry*, Vol 8 Scott, A. F. Academic Press, New York, 1977; pp57-81 (c) Toth, L. E. *Transition Metal Carbides and Nitrides* Academic Press, New York, 1971; pp 215-46

9 K. Su, M. Nowakowski, D. Bonnell, L. G.Sneddon *Chem. Mater.* 4 (1992) 1139-1141

10 Shriver, D.F.; Drezdzon, M. A. *Manipulation of Air Sensitive Compounds*; 2nd Ed., Wiley: New York, **1986**.

11 P. J. Fazen, J. S. Beck, A. T. Lynch, E. E. Remsen and L. G. Sneddon. *Chem. of Mater.* 2 (1990) 96-97.

12 L.. Reimer, *Advances in Electronics and Electron Physics* **81** (1991) 43.

13 M. Ruhle, J. Mayer, J. C. H. Spence, J. Bihr, W. Probst, E. Weimer, Proceedings of 49th Annual Meeting of EMSA ed. G. W. Bailey, J. Bentley and J. A. Small San Francisco Press, Inc. (1992) 706-707.

14 J. Mayer, Proceedings of 49th Annual Meeting of EMSA ed. G. W. Bailey, J. Bentley and J. A. Small San Francisco Press, Inc. (1992) 1198-1199.

15 L. Reimer, I. Fromm, C. Hulk, R. Rennekamp *Microsc. Microanal. Microstruct.* 3 (1992) 141-157.

16 T. Matsudaira, H. Itoh, S. Naka, H. Hamamoto, M. Obayashi, *J. Mat. Sci.* 23 (1988) 288-292.

FIGURE CAPTIONS

Figure 1. Schematic EELS spectrum illustrating the three window technique used for elemental mapping. Acquisitions at the energy losses ΔE_1 and ΔE_2 are used to extrapolate the background contribution to the intensity at the energy loss ΔE_3.

Figure 2. Schematic design of the imaging filter TEM (a) with integrated spectrometer (b).

Figure 3. X-ray diffraction patterns of samples heated for 16 hrs at 800 °C and for 2 hrs at other temperatures. At 800 °C, only Ti metal and amorphous phase are present. At higher temperatures both TiN and TiB_2 are present.

Figure 4. X-ray data diffraction patterns of samples heated to 1200°C for 1 hr. (a), 3.8 hrs. (b), and 49 hrs. (c).

Figure 5. Crystallization of TiN and TiB_2 at various temperatures.

Figure 6. Schematic diagram of the phase compatibilities indicated by the phase analyses. The TiB2-BN and TiN-BN tie lines are implied but not yet confirmed.

Figure 7. Electron spectroscopic imaging of a sample heated at 1200 °C for 1 hr. Elemental maps of B, N and Ti with the corresponding bright field micrograph can be used to deduce the phases.

Figure 8. Elemental maps of B and N indicating the presence of BN and a bright field image of the structure. Solution of Ti in the amorphous BN cannot be detected.

Figure 9. Phase distribution of TiN/TiB_2 at 1450°C after 1 h. The arrows in the bright field image indicate TiB_2 grains.

Figure 10. TEM bright field micrograph and elemental maps of BN/TIN. The diffraction pattern of BN and the parallel EELS spectra of both phases, including the extrapolated backgrounds, are shown at the right. The EELS spectra have been recorded with a slow scan CCD camera.

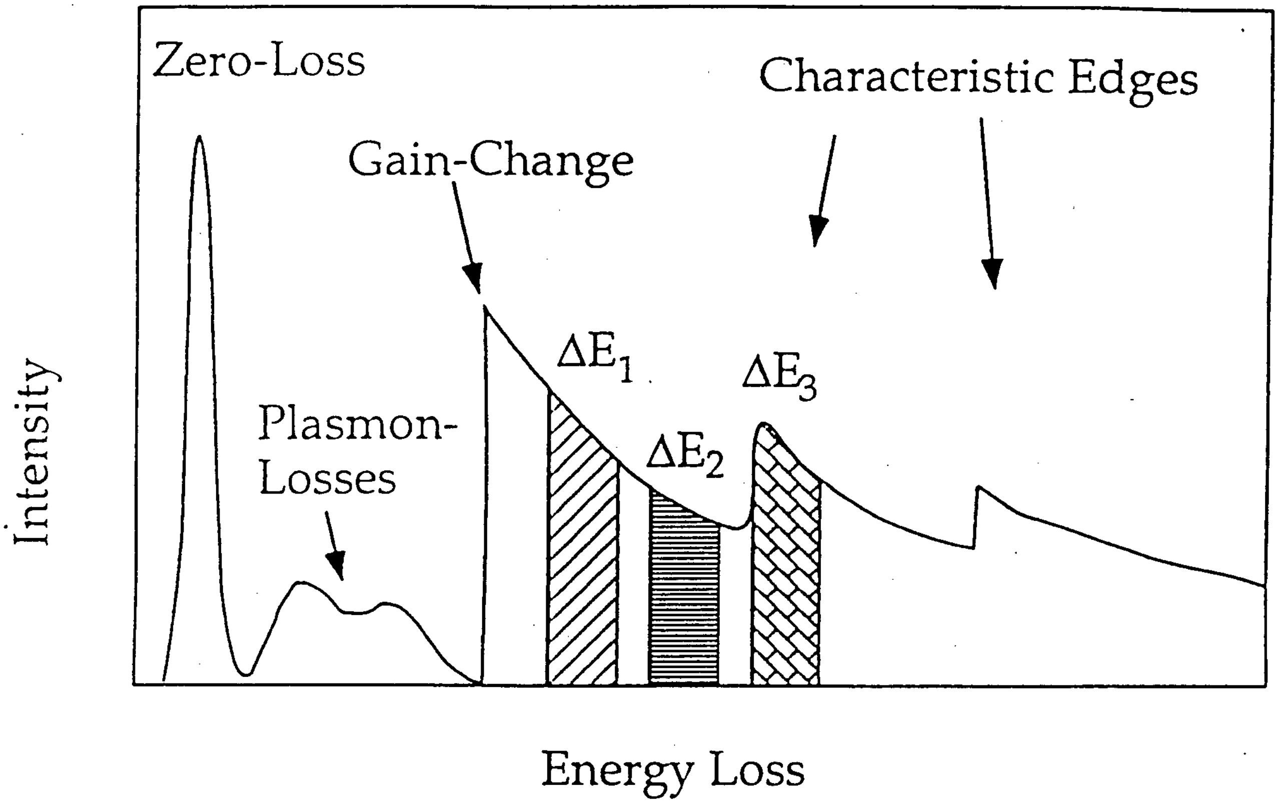
Zero-Loss
Characteristic Edges
Gain-Change
Plasmon-Losses
ΔE_1
ΔE_2
ΔE_3
Intensity
Energy Loss

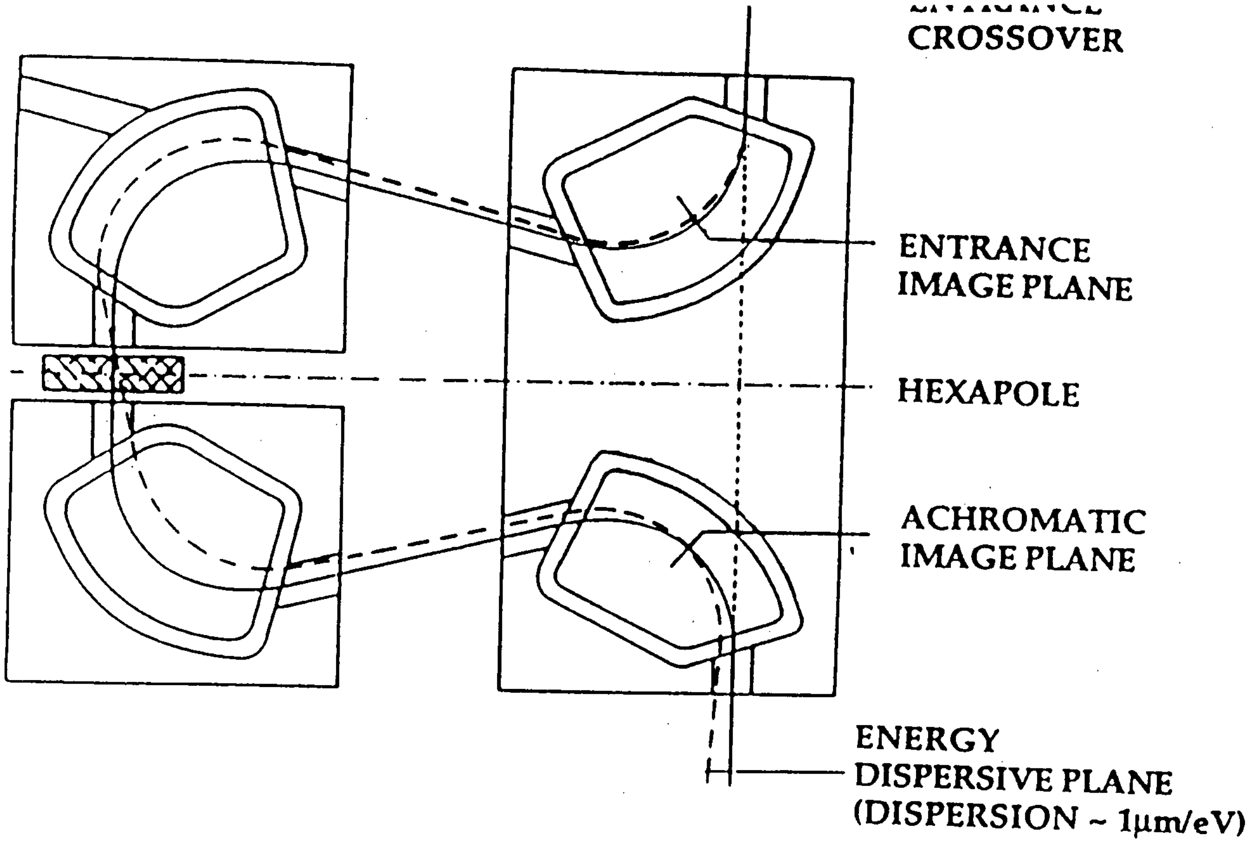
CROSSOVER
ENTRANCE
IMAGE PLANE
HEXAPOLE
ACHROMATIC
IMAGE PLANE
ENERGY
DISPERSIVE PLANE
(DISPERSION ~ 1μm/eV)

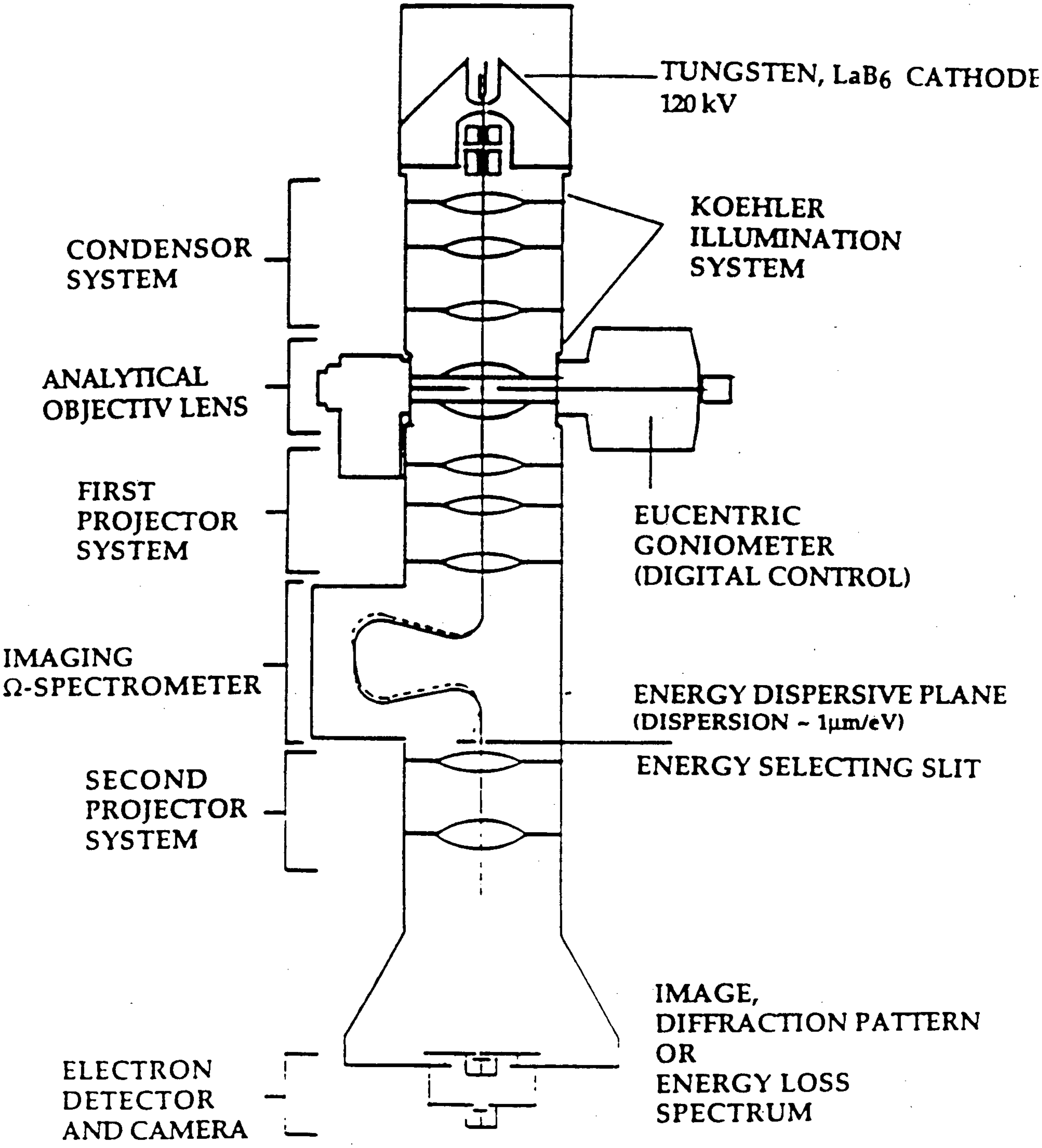

Column and spectrometer adjusted for E_0

High voltage varied for EELS, ESI: ($E_0+\Delta E$)

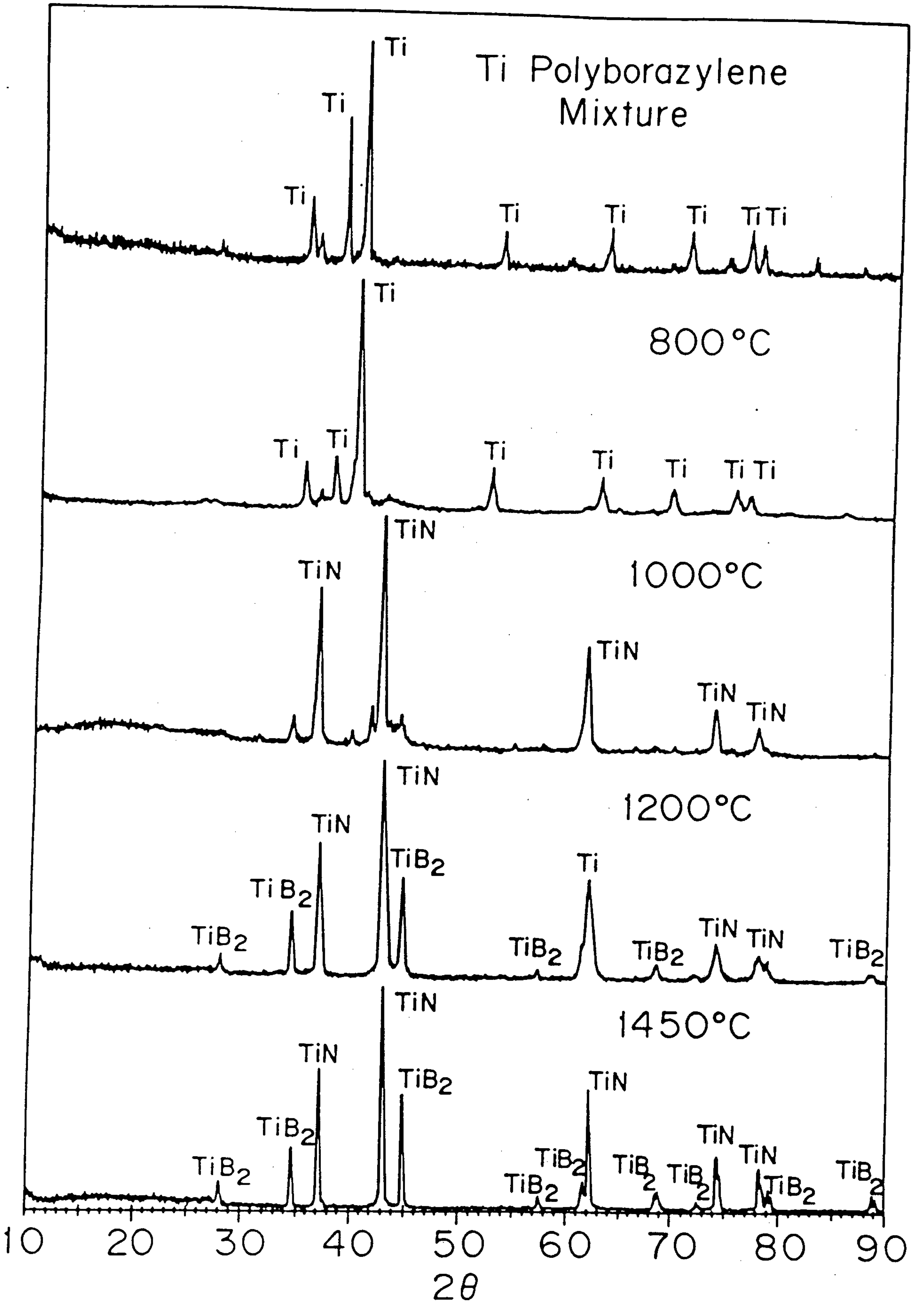

Ti Polyborazylene
Mixture
Ti
Ti
Ti
Ti
Ti
Ti
Ti Ti
800°C
Ti
Ti
Ti
Ti
Ti
Ti
Ti Ti
1000°C
TiN
TiN
TiN
TiN
TiN
1200°C
TiN
TiN
TiB2
TiB2
TiB2
Ti
TiB2
TiB2
TiN
TiN
TiB2
1450°C
TiN
TiN
TiB2
TiB2
TiB2
TiN
TiB2
TiB2
TiB2
TiB2
TiN
TiN
TiB2
TiB2
10
20
30
40
50
60
70
80
90
2θ

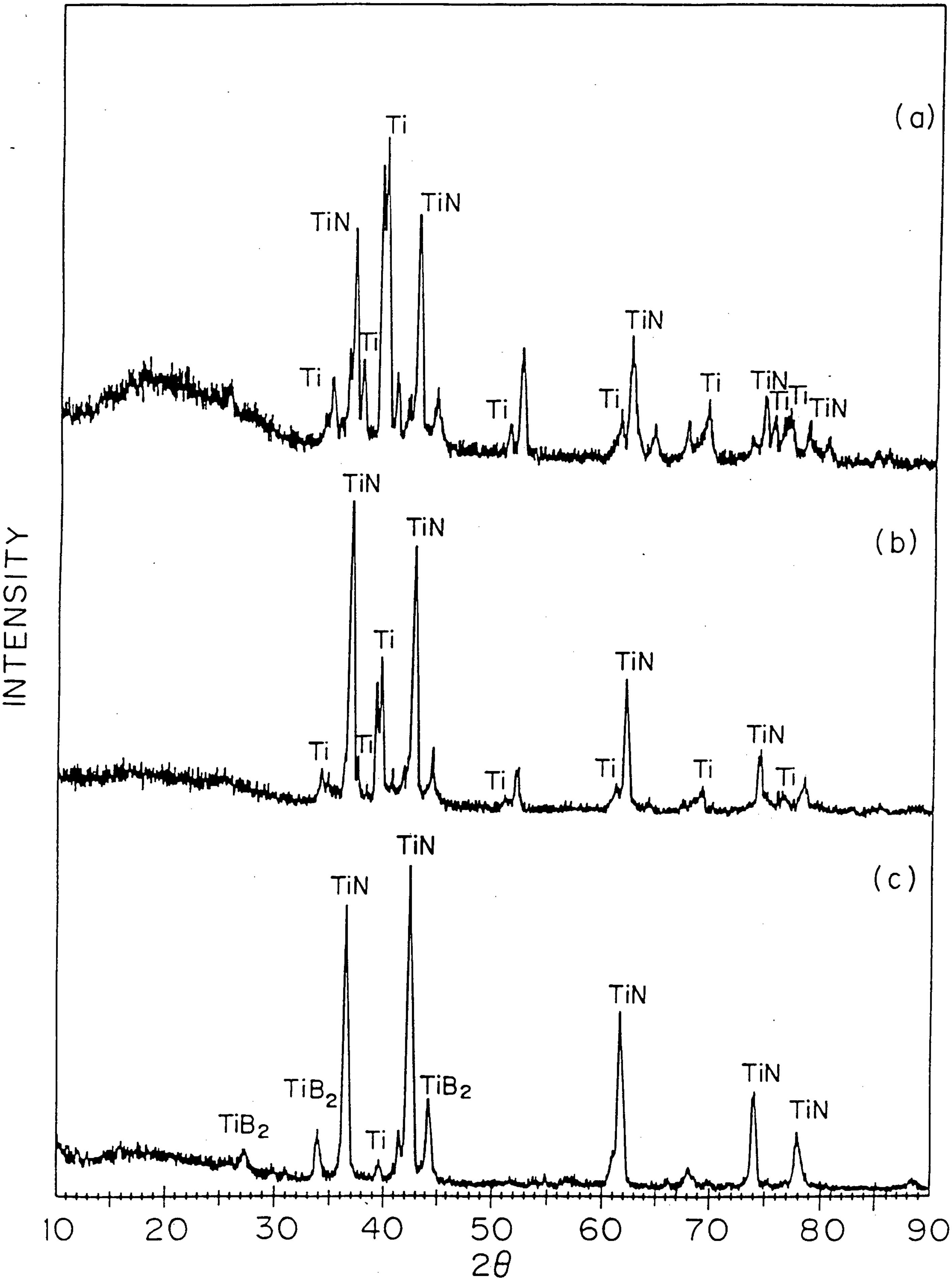
(a)
Ti
TiN
TiN
Ti
Ti
TiN
Ti
Ti
Ti
TiN
Ti
Ti
TiN
(b)
TiN
TiN
Ti
Ti
Ti
TiN
Ti
Ti
Ti
TiN
Ti
(c)
TiN
TiN
TiB2
TiB2
TiB2
Ti
TiN
TiN
TiN
INTENSITY
10
20
30
40
50
60
70
80
90
2θ

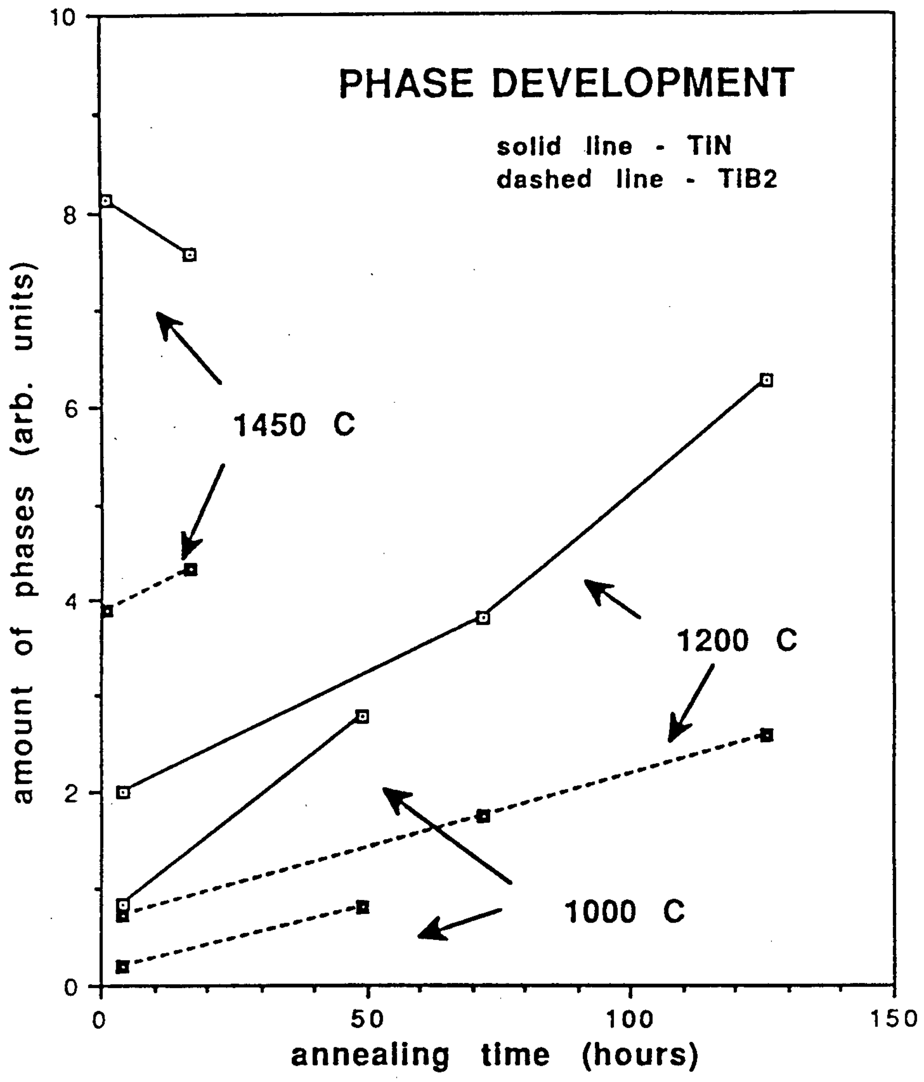
PHASE DEVELOPMENT
solid line - TiN
dashed line - TiB2
1450 C
1200 C
1000 C
amount of phases (arb. units)
annealing time (hours)
0
2
4
6
8
10
0
50
100
150

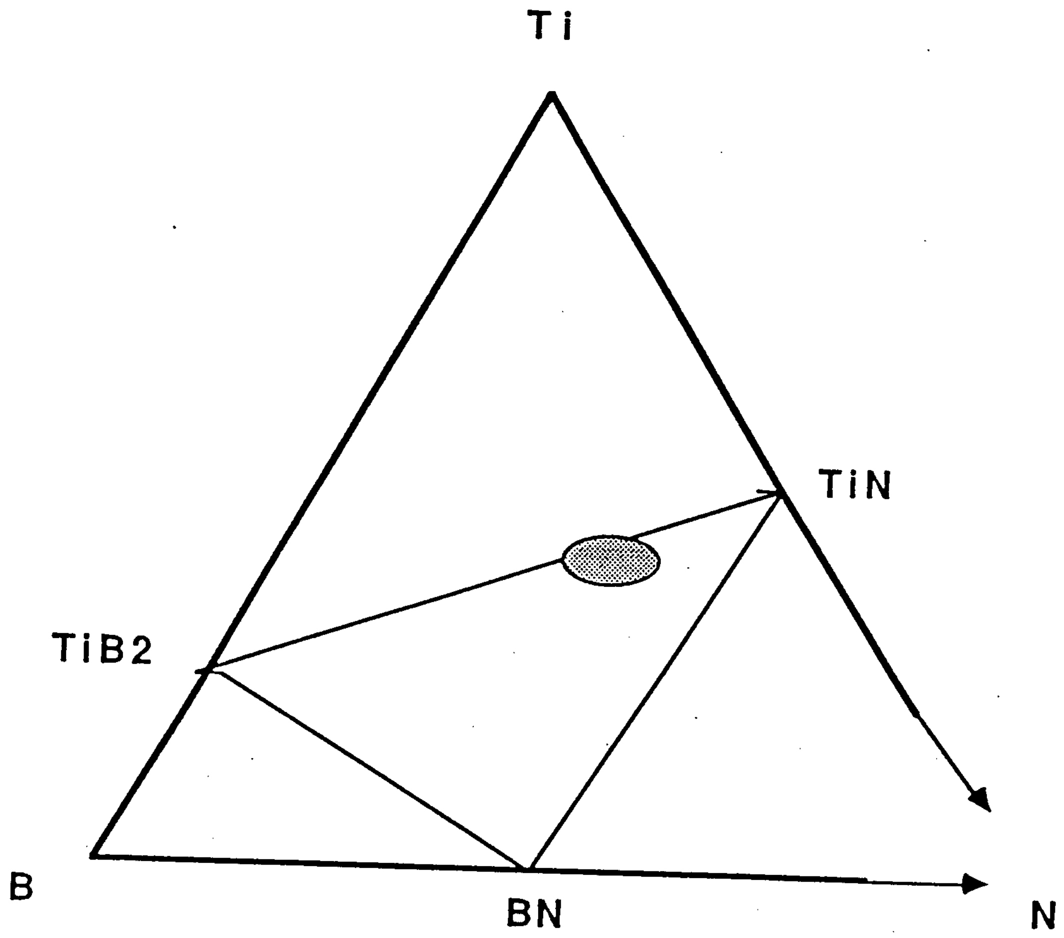

PROPOSED SUBSOLIDUS PHASE COMPATIBILITIES

1200 C 1 h

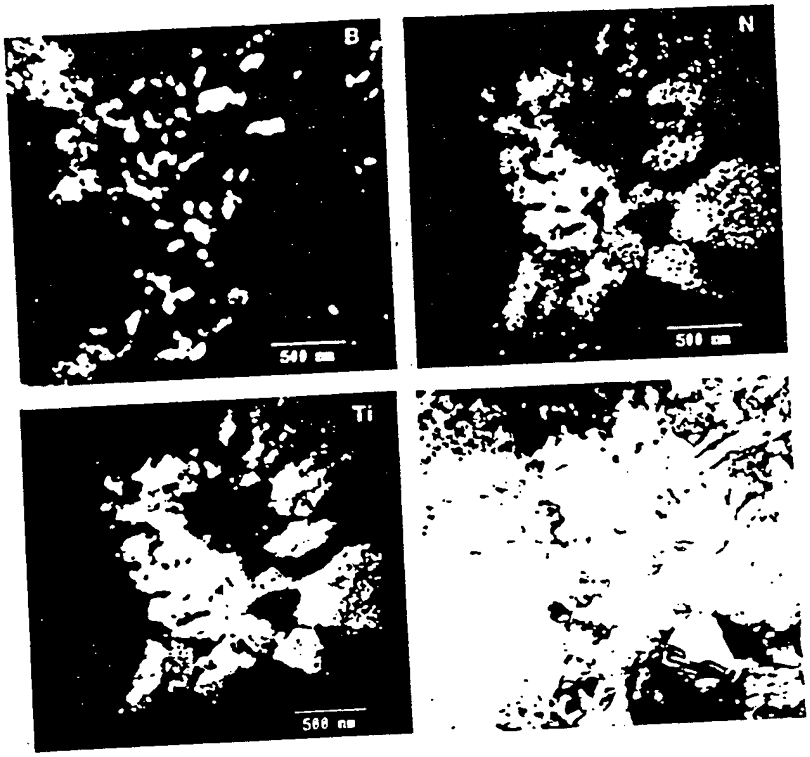

1200 C 1 h

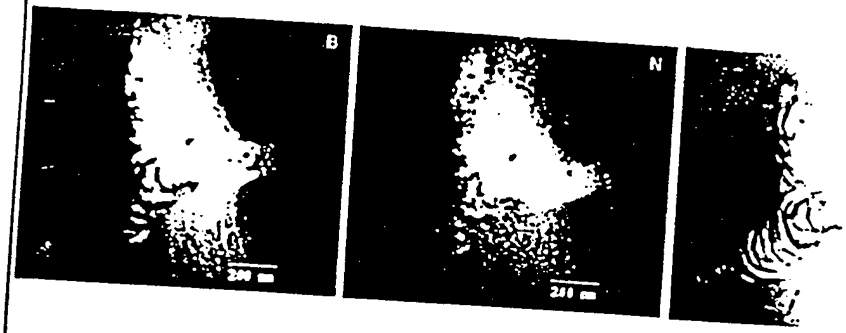

1450°C 1h

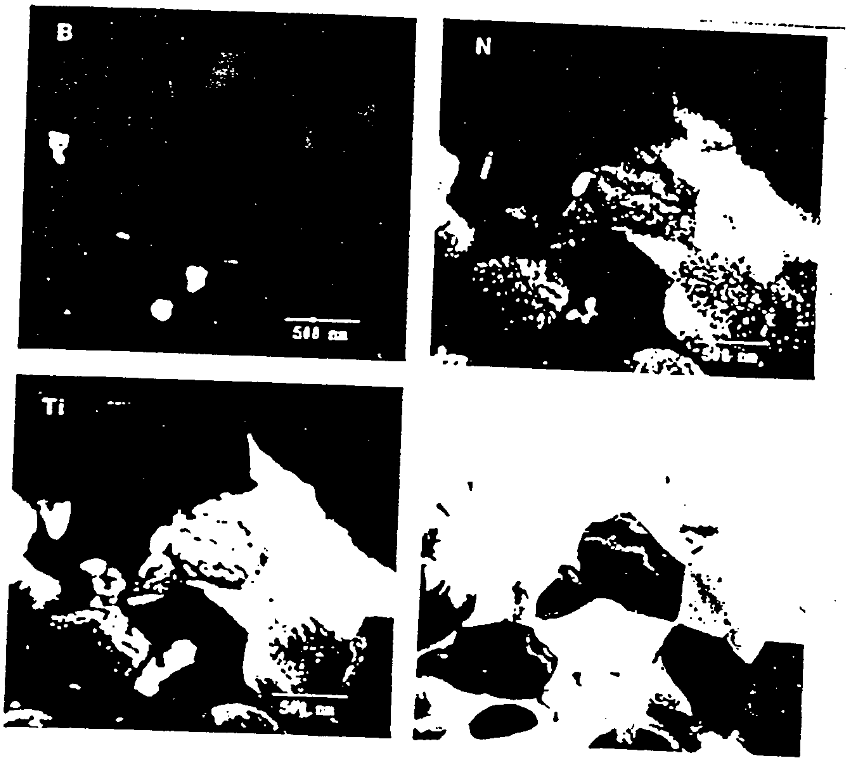

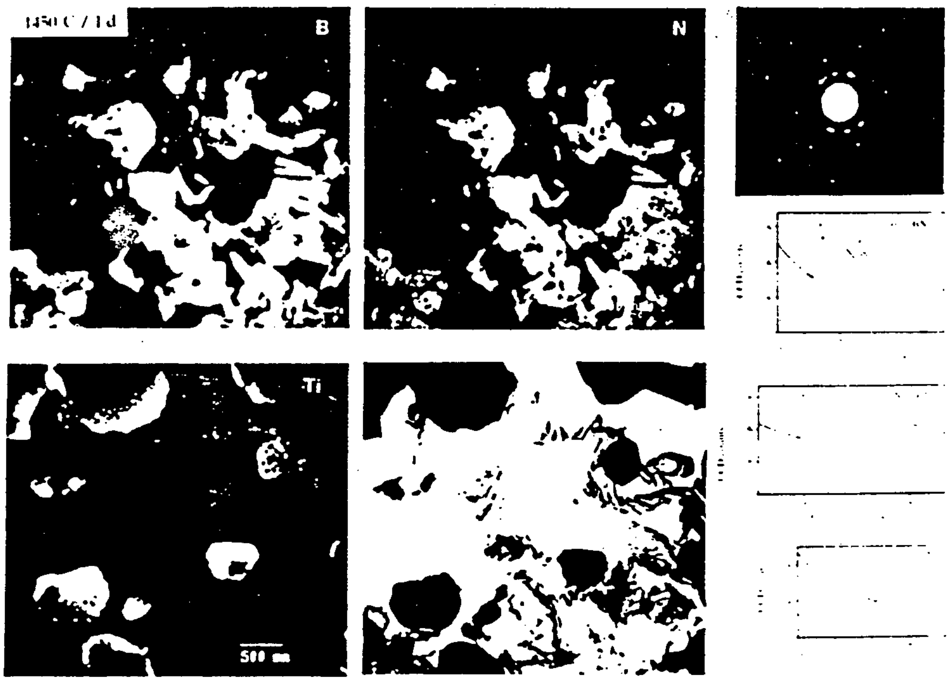
1450 C / 1 d
B
N
Ti
500 nm

Reprinted from Chemistry of MATERIALS, 1992, *4*.

Polymer Precursor Route to TiB_2/TiN Nanocomposites

Kai Su,[1] Marilyn Nowakowski,[2] Dawn Bonnell,*[,2] and Larry G. Sneddon*[,1]

Departments of Chemistry and
Materials Science and Engineering and the
Laboratory for Research on the Structure of Matter
University of Pennsylvania
Philadelphia, Pennsylvania 19104

Received June 24, 1992
Revised Manuscript Received August 18, 1992

Because of their high melting points, hardness, and chemical resistance at high temperatures, metal borides and metal nitrides are two of the most important families of engineering ceramics.[3,4] We report in this communi-

---

[1] Department of Chemistry.

[2] Department of Materials Science and Engineering.

[3] For general reviews of the syntheses, structures and properties of metal borides see: (a) Greenwood, N. N.; Parish, R. V.; Thornton, P. *Q. Rev.* 1966, *20*, 441–461. (b) Matkovich, V. I. *Boron and Refractory Borides*; Springer-Verlag: New York, 1977. (c) Post, B. In *Boron, Metallo-Boron Compounds and Boranes*; Adams, R. M., Ed.; Interscience: New York, 1964; pp 301–372. (d) Greenwood, N. N. *The Chemistry of Boron*; Pergamon: New York, 1975; pp 697–731. (e) Thompson, R. In *Progress in Boron Chemistry*; Pergamon: New York, 1970; Vol. 2, pp 173–230. (f) Hoard, J. L.; Hughes, R. E. In *The Chemistry of Boron and Its Compounds*; Muetterties, E. L., Ed.; Wiley: New York, 1967; pp 25–154.

0897-4756/92/2804-1139$03.00/0

cation a polymer-based synthetic route by which monolithic nanophase titanium boride/titanium nitride composite materials may be produced in [illegible] high ceramic and high chemical yields by polymer pyrolysis under inert atmosphere.

We have previously reported the preparation of the new boron–nitrogen polymer polyborazylene, $(B_3N_3H_4)_x$, and shown that this processable polymer can be converted to boron nitride in high ceramic and chemical yields (90–94%).[5] We have also demonstrated a new, potentially general route to metal borides, such as TiB_2 and ZrB_2, involving the reduction of the corresponding metal oxide with a boron–carbon-based polymer $(B_{10}H_{12}\text{–dinitrile})_x$.[6] Work by Seyferth[7] and Greil[8] has likewise shown that pyrolysis of preceramic–polymer/metal–powder mixtures can be used to generate composite ceramics containing metal silicides, carbides, nitrides, or borides. Taken together these results suggested that the reactions of a metal with polyborazylene might lead to incorporation of both polymer boron and nitrogen atoms to produce new composite metal–nitride/metal–boride materials which might have improved properties over an individual metal boride or nitride.[9] Furthermore, since high ceramic and chemical yields should be possible with the polyborazylene/metal system without employing a reactive pyrolysis atmosphere (e.g., ammonia), then the formation of monolithic ceramic materials should be enabled.

Such a titanium boride/titanium nitride precursor system was made by dispersing titanium powder into polyborazylene. Final ceramic materials were prepared by pyrolysis of either powders or shaped green bodies under inert atmosphere:

$$(B_3N_3H_4)_x + Ti \xrightarrow{\Delta} TiN/TiB_2 + H_2$$

In a typical process, 12.1 g of titanium metal (325 mesh, Strem Chemicals) was added to a dry tetrahydrofuran solution containing 5.0 g of polyborazylene. The solvent was then vacuum evaporated while maintaining ultrasonic agitation. The resulting black solid dispersion was ground into a fine powder. A 0.78-g sample was then heated under argon at 1450 °C for 10 h, resulting in the formation of 0.69 g of ceramic material, which corresponds to 91.8% ceramic and 88.5% chemical yields. Elemental analysis of the ceramic corresponds to a composition of $Ti_{1.0}B_{0.50}N_{0.57}H_{<0.06}O_{0.1}C_{0.14}$ consistent with a $(TiN)_{0.57}(TiB_2)_{0.25}Ti_{0.18}O_{0.1}C_{0.14}$ mixture.[10,11]

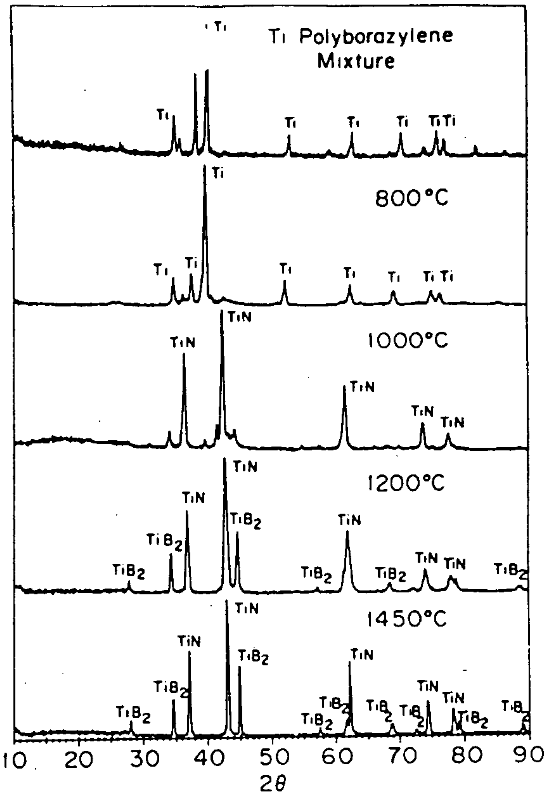

Figure 1. XRD spectra of the initial polymer/titanium powdered dispersion and bodies treated[12] at 800, 1000, 1200, and 1450 °C.

Green bodies were made by isostatic pressing of 1–5-g samples of polymer/titanium dispersions at room temperature at 75000 psi. The green bodies were then heated[12] under argon separately at 1000, 1200, and 1450 °C, resulting in the production of ceramic bodies with ceramic yields of 96.0%, 95.5%, and 94.9%, respectively. The final ceramic bars showed excellent shape retention. The ceramic monolith prepared at 1000 °C had a linear shrinkage of about 6%. The densities of the ceramic bodies increased from 3.0 (1000 °C) to 3.9 (1450 °C) with the increasing reaction temperatures.

A TGA study of the ceramic conversion reaction showed weight losses in the ranges 50–300 and 450–800 °C, similar to those observed in the conversion of pure polyborazylene to boron nitride.[5] At 1350 °C an additional weight loss was observed which, consistent with an observed decrease in the oxygen content of materials treated above this temperature,[10] is probably due to evaporation of B_2O_3 produced by the reduction of titanium oxide impurities by boron.

X-ray diffraction studies of the ceramic conversion reaction have shown that the product exhibits variations in composition and crystallinity as the processing temperature and/or time is increased. Thus, as can be seen in Figure 1, there appears to be little reaction between the polymer and the titanium metal when the sample was heated at 800 °C for 9.5 h. Consistent with this conclusion, elemental analyses of a sample at this point showed that the material still had a significant hydrogen content[10] with the observed $B_{1.03}$:$N_{1.0}$:$H_{0.79}$ ratio suggesting that polymer cross-linking was still occurring. When the sample was heated at 1000 °C for 2 h, the titanium metal was completely consumed by reaction with the polymer and crystalline titanium nitride was initially observed to form. The

---

(4) For general reviews of the syntheses, structures and properties of metal nitrides see: (a) Toth, L. E. In *Transition Metal Carbides and Nitrides*: *Academic Press*: New York, 1971; pp 1–28. (b) Johansen, H. A. In *Survey of Progress in Chemistry*; Scott, A. F., Ed.; Academic Press: New York, 1977; Vol. 8, pp 57–81. (c) Toth, L. E. In *Transition Metal Carbides and Nitrides*; Academic Press: New York, 1971; pp 215–46.

(5) (a) Fazen, P. J.; Beck, J. S.; Lynch, A. T.; Remsen, E. E.; Sneddon, L. G. *Chem. Mater.* 1990, 2, 96–97. (b) Fazen, P. J.; Sneddon, L. G. *Polym. Prepr.* (*Am. Chem. Soc., Div. Polym. Chem.*) 1991, *32*, 544–545.

(6) Su, K.; Sneddon, L. G. *Chem. Mater.* 1991, *3*, 10–12.

(7) Seyferth, D.; Bryson, N.; Workman, D. P.; Sobon, C. A. *J. Am. Ceram. Soc.* 1991, *74*, 2687–2689.

(8) (a) Greil, P.; Seibold, M. *Ceram. Trans.* 1991, *19*, 43–49. (b) Greil, P.; Seibold, M. *Adv. Mater. Processes*, *Proc. Eur. Conf.* Exner, H. E.; Schumacher, V. Eds., DGM Informationsges: Oberursel, 1990; Vol. 1, pp 641–646. (c) Greil, P.; Seibold, M. *J. Mater. Sci.* 1992, *27*, 1053–1060.

(9) Metal nitride/BN nanocomposites have previously been obtained upon pyrolysis of polymers derived from the reaction of trisazidoborazine and metal isothiocyanato complexes. See: Borek, T. T.; Paine, R. T.; Datye, A. K. *Mater. Res. Soc. Proc.* 1990, 33–35.

(10) Elemental analyses: 1450 °C ceramic: Ti, 73.4%; B, 8.31%; N, 12.2%; O, 2.91%; C, 2.66%; H, < 0.1%; 800 °C material: Ti, 65.8%; B, 9.80%; N, 12.3%; O, 8.58%; C, 0.66%; H, 0.70%. All analyses were performed at Pascher, Remagen, Germany.

(11) Carbon impurities may have come from the carbon crucibles used for pyrolysis.

(12) The green bodies were first annealed at 800 °C for 9.5 h, then heated (5 °C/min) separately to 1000, 1200, or 1450 °C and held at temperature for 2 h.

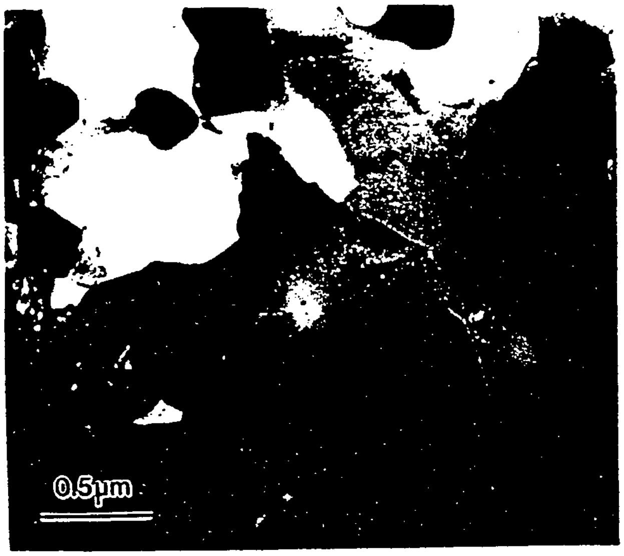

Figure 2. TEM of ceramic body treated at 1450 °C.

formation of crystalline TiB_2 was observed only upon heating of samples for either longer times (1000 °C, 3 days) or at higher temperatures (1200 °C, 1 h). The spectrum shown in the figure obtained from the sample annealed at 1200 °C for 2 h clearly indicates the presence of both crystalline TiB_2 and TiN. The decrease in the linewidths in the spectrum of the 1450 °C sample is consistent with an increase in the average crystal size.[13] SEM studies of bodies prepared at 800, 1000, 1200, and 1450 °C also indicate a change in morphology after 1000 °C suggesting the onset of reaction.

Consistent with the above results, TEM analysis of the compact annealed at 800 °C for 9.5 h shows the presence of 20–100-nm spherical crystals embedded in an amorphous matrix. These crystals could be either unreacted titanium metal or nucleated titanium nitride. For the ceramic compact annealed at 1200 °C,[12] TEM shows angular grains on the order of 50–100 nm which have two contrast levels. While it is tempting to assign these contrast levels to the two phases detected by X-ray diffraction, electron diffraction was impossible due to the size of the crystals. In agreement with the XRD study, the TEM of the 1450 °C sample presented in Figure 2, shows that two types of grains are still evident but that they have increased in size. There is some indication of a residual amorphous phase in both the images and electron diffraction patterns.

The preparations of TiB_2/TiN and TiB_2/Ti(CN) composite materials by sintering TiB_2 and TiN or TiCN powders at high temperatures have previously been reported.[14] Seyferth has also reported that a crystalline TiB_2/TiN powder composite can be made by the pyrolysis of $[B_{10}H_{12}\text{-diamine}]_x$ polymer/Ti under NH_3 atmosphere.[7] TiB_2/TiN composite coatings have also been achieved by CVD methods.[15] The polyborazylene-based route discussed herein is unique, however, in that it is the only reported direct chemical method which can be used to produce monolithic titanium boride/nitride composites, consisting of intimately mixed polycrystals with grain sizes on the order of nanometers, in high ceramic and chemical yields. The dependence of the crystal size and its distribution on the reaction/sinter temperature, the evolution of microstructure and the properties of the final composite material, such as conductivity and hardness are currently under investigation. We are also exploring the reactions of polyborazylene with other metals and soluble metal complexes with the goal of developing a range of new metal boride/nitride precursor systems that will allow the formation of both shaped bodies and coatings.

Acknowledgment. We thank the Department of Energy, Division of Chemical Sciences, Office of Basic Energy Sciences and the National Science Foundation Materials Research Laboratory at the University of Pennsylvania for support of this research. We also thank Professor Abhaya Datye for some initial TEM results on composite powder samples and Mr. William Romanow for assistance with the isostatic pressing.

Registry No. Ti, 7440-32-6; TiN, 25583-20-4; TiB_2, 12045-63-5; polyborazylene, 143186-38-3.

---

[13] Klug, H. P.; Alexander, L. E. *X-Ray Diffraction Procedures*; Wiley: New York, 1973; Chapter 9, pp 618–708.

[14] (a) Shobu, K.; Watanabe, T.; Enomoto, Y.; Umeda, K.; Tsuya, Y. *J. Am. Ceram. Soc.* 1987, *70*, C103–C104. (b) Watanabe, T.; Yamamoto, H.; Shobu, K.; Sakamoto, T. *J. Am. Ceram. Soc.* 1988, *71*, C202–C204.

[15] Becht, J. G. M.; Van der Put, P. J.; Schoonman, J. *Solid State Ionics* 1989, *32*, 789–794.